FRIEDRICH-SCHILLER-
UNIVERSITÄT
JENA

Triplet-Triplet Annihilation Upconversion in Polymeric Systems and Model Membranes

Dissertation
zur Erlangung des akademischen Grades doctor rerum naturalium
(Dr. rer. nat.)

vorgelegt dem Rat der Chemisch-Geowissenschaftlichen Fakultät
der Friedrich-Schiller-Universität Jena

von M. Tech. Keshav Kumar Jha
geboren am 25.02.1988 in Darbhanga, India

Gutachter/in:

1. Prof. Dr. Benjamin Dietzek-Ivanšić (Friedrich Schiller University Jena)

2. Prof. Dr. Tia Keyes (Dublin City University)

Tag der öffentlichen Verteidigung: 20.07.2023

॥ तमसो मा ज्योतिर्गमय॥

May the light of knowledge remove the darkness of ignorance.

Bṛhadāraṇyaka Upaniṣad (1.3.28.)

Table of Contents

Publications and Conference Contributions

Some of the results presented in this thesis have already been published in peer-reviewed journals or have been presented as presentations at designated conferences. The peer-reviewed journals and conference contributions are listed below.

* Represents equal contribution.

Articles in Peer-reviewed Journals

1. **Jha, K. K.***; Prabhakaran, A.*; Sia, R.C.; Arellano-Reyes, R.A.; Sarangi, N.K.; Kupfer, S; Guthmuller**, J;** Keyes, T.E.; Dietzek-Ivanšić, B.; Triplet Formation and Triplet-Triplet Annihilation Upconversion in Iodine Substituted Non-Orthogonal BODIPY-Perylene Dyads; *ChemPhotoChem* **2023**, e202300073.
2. [Submitted ChemPhotoChem] **Jha, K. K.**; Prabhakaran, A.; Spantzel, L; Sia, R.C.; Pérez, I; Arellano-Reyes, R.A.; Elmanova, A; Dasgupta, A; Eggeling, C; Börsch, M; Guthmuller, J; Presselt, M; Keyes, T. E.; Dietzek-Ivanšić, B.; A BODIPY-Molecular Rotor in Giant Unilamellar Vesicles: A Case Study by Polarization-Resolved Time-resolved Emission and Transient Absorption Spectroscopy.
3. [In preparation] Prabhakaran, A.*; **Jha, K. K.***; Keyes, Sia, R.C.; Arellano-Reyes, R.A.; Sarangi, N.K.; Kupfer, S; Guthmuller**, J;** Ivanšić, B. D.; BODIPY-Perylene Dyad Sensitized Triplet-Triplet Annihilation Upconversion in Solution and Model Membranes.
4. **Jha, K. K.**; Prabhakaran, A.; Burke, C. S.; Schulze, M.; Schubert, U. S.; Keyes, T. E.; Jäger, M.; Ivanšić, B. D.; Triplet–Triplet Annihilation Upconversion by Polymeric Sensitizers. *J. Phys. Chem. C* **2022**, *126* (8), 4057–4066.
5. Chettri, A.; Kruse, J. H.; **Jha, K. K.**; Dröge, L.; Romanenko, I.; Neumann, C.; Kupfer, S.; Turchanin, A.; Rau, S.; Schacher, F. H.; Dietzek, B. A Molecular Photosensitizer in a Porous Block Copolymer Matrix-Implications for the Design of Photocatalytically Active Membranes. *Chem. - A Eur. J.* **2021**, *27*, 1–11.
6. Arellano-Reyes, R. A.; Prabhakaran, A.; Sia, R. C. E.; Guthmuller, J.; **Jha, K. K.**; Yang, T.; Dietzek-Ivanšić, B.; McKee, V.; Keyes, T. E.; BODIPY-Perylene Charge Transfer Compounds; Sensitizers for Triplet-Triplet Annihilation Up-Conversion. *Chemistry – A European Journal,* **2023**, e202300239.
7. Yang, T.; Arellano-Reyes, R. A.; Curley, R. C.; **Jha, K. K.**; Chettri, A.; Keyes, T. E.; Dietzek-Ivanšić, B. In Cellulo Light-Induced Dynamics in a BODIPY-Perylene Dyad. *Chemistry – A European Journal,* **2023**, e202300224.

Conference Contributions

1. [Talk] **Jha, K. K.**; Prabhakaran, A.; Keyes, T. E.; Ivanšić, B. D.; Triplet–Triplet Annihilation Upconversion by Polymeric Sensitizers. *Bunsentagung*, Gießen, Germany, September **2022**.
2. [Talk] **Jha, K. K.**; Prabhakaran, A.; Keyes, T. E.; Ivanšić, B. D.; The BODIPY Molecular Rotor in The Giant Unilamellar Vesicle: A Case Study by Transient Absorption Anisotropy. *28th Lecture Conference on Photochemistry (GDCh)*, Düsseldorf, Germany, September **2022**.
3. [Poster] **Jha, K. K.***; Sarkar, P.*; Biswas, R.; Bhat, R.; Raghunathan, V. A Spatiotemporal Analysis Using Second Harmonic Generation Reveals Enhancement of Type I Collagen Polymerization by Dermatan Sulfate Glycosaminoglycans. *European Conferences on Biomedical Optics*; 2019; Vol. 11076, pp 45–47. Munich, Germany, June **2019**.

List of Abbreviations

Spectroscopic Terms

Abs	Absorbance
ACN	Acetonitrile
CR_S	Charge recombination to ground state
CR_T	Charge recombination to triplet state
CT	Charge transfer
DFT	Density functional theory
DAS	Decay associated spectra
DCM	Dichloromethane
DPA	9,10-diphenylanthracene
ESA	Excited state absorption
ET	Energy transfer
FLIM	Fluorescence lifetime imaging microscopy
FMR	Fluorescent molecular rotor
FRET	Fluorescence resonance energy transfer
fs-TA	Femtosecond transient absorption
FWHM	Full-width-at-half-maximum
GSB	Ground state bleach
GUV	Giant unilamellar vesicle
IC	Internal conversion
IRF	Instrumental response function
ISC	Intersystem crossing
LiDAR	Light detection and ranging
LE	Locally excited state
LED	Light emitting diode
LUV	Large unilamellar vesicle
MLCT	Metal-to-ligand charge transfer
MS	Monomeric triplet sensitizer
MVE	Minimum volume ellipsoid
ns-TA	Nanosecond transient absorption
Para	Parallel
Perp	Perpendicular
PCM	Polarizable continuum model

P(EO-EP)	Poly ethylene oxide-epichlorohydrin
PEG	Poly(ethylene glycol)
PES	Potential energy surface
PMMA	Poly(methyl methacrylate)
PS	Polymeric triplet sensitizer
RP-ISC	Radical pair-intersystem crossing
SE	Stimulated emission
SO	Spin-orbit
SOCT-ISC	Spin-orbit charge transfer-intersystem crossing
SV	Stern-Volmer
TA	Transient absorption
TAA	Transient absorption anisotropy
TDM	Transition dipole moment
TDDFT	time-dependent density functional theory
TE	Time-resolved emission
TEA	Time-resolved emission anisotropy/ time-resolved fluorescence anisotropy
TREPR	Time-resolved electron paramagnetic resonance
TTAUC	Triplet-triplet annihilation upconversion
TTA	Triplet-triplet annihilation
TTET	Triplet-triplet energy transfer
UC	Upconversion
UN	United Nations
UNESCO	United Nations Educational Scientific and Cultural Organization
UV	Ultraviolet (100 nm to 380 nm)
UV/Vis	Ultraviolet/Visible (380 nm to 760 nm)
VR	Vibrational relaxation
ΔOD	Differential optical density

Units

cP	centipoise
cm	centimeter
eV	electron-volt
fs	femtosecond
kHz	kilo Hertz
L	Liter

mJ	milli Joule
$mol^{-1} \cdot cm^{-1}$	$mol^{-1} \cdot$ centimeter^{-1}
ms	millisecond
$M^{-1}s^{-1}$	$L \cdot mol^{-1} \cdot$ second^{-1}
µs	microseconds
mW cm^{-2}	Milliwatt per centimeter square
nm	nanometer
ns	nanosecond
ps	picosecond
s	second
$s^{-1} \cdot cm^{-1}$	second$^{-1} \cdot$ centimeter^{-1}
W	Watt

Molecules and Ligands

bpy	2,2′-bipyridine
dqp	di(quinolin-8-yl)pyridine
BODIPY	4,4-difluoro-4-bora-3a,4a-diaza-s-indacene
B2P	Ph-2-BODIPY-2_Perylene
B2PI	Ph-2-BODIPY-2_Perylene-Iodine
chol	cholesterol
DOPC	1,2-dioleoyl-sn-glycero-3-phosphocholine
Ph	phenyl

1. Introduction

1.1 Motivation

The scientific advancement in the field of optics and photonics has greatly improved human life. The applications of light-based technologies are very broad and have found a place in day-to-day life *e.g.* spectacles for vision, light bulbs, or the sensors used in smartwatches, *etc*. It has played a pivotal role in the advancement of various scientific fields *e.g.* LiDAR for environmental research or microscopy for biological research. The impact of this field has such tremendous influence on society that, the United Nations (UN) recognized the year 2015 as the International Year of Light and Light-based Technologies. The United Nations Educational Scientific and Cultural Organization (UNESCO) announced May 16th as the International Day of Light in the memory of first successful operation of the laser by Physicist Theodore Maiman in the year 1960 and conducted outreach programs to raise awareness on the advancement of the light-based technologies and reached over a hundred million people in the year 2015 [*lightday.org*].

Optical spectroscopy is the field of study describing the interaction (*e.g.* absorption, emission, reflection, refraction, *etc*.) of UV, visible or infrared electromagnetic radiation by matter.[1] It has found wide applications at the interface of optics, chemistry and biology. In optical spectroscopy, matter interacts with the excitation photons and may emit photons of energy lower or higher than the excitation photons. The emission of higher energy photons has attracted much attention and found application in the development of lasers,[2,3] photovoltaics,[4,5] light-activated drug release[6] *etc*. There are two major pathways of forming a higher energy photon from two lower energy photons (i) harmonic generation[2,7] (ii) triplet-triplet-triplet annihilation upconversion (described in detail in section 1.2).[8–10] The harmonic generation needs coherent radiation with excitation power density near 100 mW cm^{-2} whereas triplet-triplet annihilation upconversion (TTAUC) requires incoherent photons with excitation power density as low as a few mW cm^{-2} to generate a higher energy photon,[10] due to low excitation power density TTAUC can harness solar energy.[4]

TTAUC has been used to generate green to blue,[11] red to green,[12] red to yellow,[13] NIR to blue,[14] photons. Although, the TTAUC has tremendous advantages and numerous applications; it is a bimolecular diffusion-controlled process, hence most efficient in liquids where its constituents are free to diffuse and to participate in intermediate

processes (*vide infra*).[8–10] Despite its potential, practical applications of TTAUC which need the upconversion process to occur in solid-state media remain difficult to execute.

I found strong motivation to contribute to the incoherent, low excitation density upconversion process (TTAUC) and make developments beyond state of the art. There are several scientific questions on this topic, which originate from the application of TTAUC in solid-state media and in lipid bilayer membranes, which need to be answered for the further development and application of the TTAUC process. Some of the important questions which lead to the objectives of this thesis are discussed in section 1.3.

1.2 Triplet-Triplet Annihilation Upconversion (TTAUC)

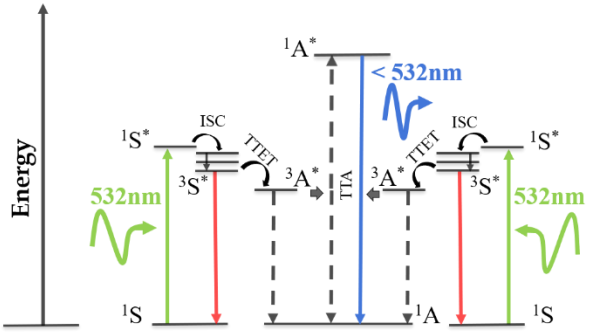

Figure 1.1: Jablonski diagram of TTAUC. Green upward arrows depict absorption by the sensitizer, and red downward arrow represents the phosphorescence of the sensitizer. Dashed downward arrows from $^3A^*$ depict the nonradiative decay of the triplet annihilator, the bidirectional dashed arrow represents TTA and the blue downward arrow depicts the emission of an upconverted photon.

Discovered by Parker and Hatchard,[15] TTAUC is a bimolecular diffusion-controlled process, where a long wavelength photon is absorbed by a sensitizer or donor molecule. Upon excitation of the sensitizers to its first singlet excited state ($^1S^*$) intersystem crossing (ISC) populates the sensitizer's lowest energy triplet state ($^3S^*$). Triplet-triplet energy transfer (TTET) transfers the triplet excited state energy from the sensitizer to an annihilator or acceptor molecule ($^3A^*$). If two $^3A^*$ annihilate by triplet-triplet annihilation (TTA), a single high-lying first singlet excited state in one of the acceptors ($^1A^*$) is formed, which decays radiatively. If the molecular system is designed correctly, the $^1A^*$ is higher in energy than the $^1S^*$ and consequently, the observed emission is of higher energy (blue-shifted) compared to the absorbed photons.[8,9,15]

The TTAUC mechanism is schematically depicted in the Figure 1.1. Two of the intermediate processes TTET and TTA are diffusion controlled. Thus, TTAUC is most suited in solutions where the sensitizer and annihilator can freely diffuse to participate in energy transfer. In addition, the solution media need to be deoxygenated, since oxygen molecules quench the triplet states (^{3}S* and ^{3}A*) and interfere with the energy transfer processes.

The intermediate processes involved in TTAUC can be understood with the following equations:[9,16,17]

Absorption/excitation	$^1S + h\nu_{exe} \rightarrow {}^1S^*$	Equation 1.1
ISC of sensitizer (rate: k_{ISC})	$^1S^* \rightarrow {}^3S^*$	Equation 1.2
TTET (rate: k_{TTET})	$^3S^* + {}^1A \rightarrow {}^3A^*$	Equation 1.3
Intrinsic decay of the sensitizer (rate: k_T)	$^3S^* \rightarrow {}^1S$	Equation 1.4
Oxygen quenching of sensitizer	$^3S^* + {}^3O_2 \rightarrow {}^1S + {}^1O_2{}^*$	Equation 1.5
Oxygen quenching of annihilator	$^3A^* + {}^3O_2 \rightarrow {}^1A + {}^1O_2{}^*$	Equation 1.6
TTA (rate: k_{TTA})	$^3A^* + {}^3A^* \rightarrow {}^1A^* + {}^1A$	Equation 1.7
Intrinsic decay of the annihilator (rate: k'_T)	$^3A^* \rightarrow {}^1A$	Equation 1.8
Emission (rate: k_f)	$^1A^* \rightarrow {}^1A + h\nu_{em}$	Equation 1.9
ISC of annihilator (rate: k'_{ISC})	$^1A^* \rightarrow {}^3A^*$	Equation 1.10

Here $^3O_2$ and $^1O_2$* are ground state and excited state oxygen molecules respectively, $h\nu_{em}$ is the energy of the emission photon.

1.3 The Applications and the Obstacles

There are two most promising applications of TTAUC: first, the application in solar cells to harness the solar radiation out of the absorption window of photovoltaics.[4,5,18–22] Using the TTAUC process, long wavelength photons (> 1 μm) from solar radiation can be upconverted into the absorption window of photovoltaics and efficiency to harness solar energy can be enhanced.[4,18–24] Second, light-activated drug release, in which liposomes are reconstituted with sensitizer, annihilator and drug molecules. The excitation light, which is also in phototherapeutic window initiates the TTAUC

mechanism to generate blue photons (400 nm), the upconverted blue photons trigger the drug release.[6,25] Both of the aforementioned applications exhibit great potential and are currently in the developmental stage. The current state of art and scientific problems which leads to objectives of this thesis are discussed below.

1.3.1 TTAUC in Solid-State Media

Despite the great potential, implementation of TTAUC within the solar cells is challenging; since, TTAUC is most efficient in liquid due to free diffusion of sensitizer and annihilator molecules. Practical application in solar cells requires the process to occur in solid-state media, which is exposed to the open environment and molecules are not entirely free to diffuse. As described in section 1.2, TTET and TTA are two diffusion-controlled energy transfer mechanisms in TTAUC. Since oxygen molecules quench the triplet states of sensitizer and annihilator, the TTAUC systems require inert conditions to work, including the exclusion of oxygen. Since deoxygenation is essential for effective TTET and TTA, significant modifications are still needed for the TTAUC systems to transfer effective concepts that work well in fluidic solutions to functionalized solid-state mediums *e.g.* gel, polymer or rubbery hosts. In this context, the TTAUC has been implemented in solid-state or gel environments and fully integrated polymer systems.[26-27]

Several approaches have been developed and adopted for integrating sensitizers and annihilators to a polymer host, that is optically inert to excitation and emission photons. Islangulov *et al*. used an ethylene oxide-epichlorohydrin P(EO-EP) as a rubbery host to integrate the sensitizer and annihilator in a solid-state environment.[28–30] The molecules integrated into the rubbery host can diffuse and participate in TTET and TTA because of the low crystallinity and glass transition temperature.[28] To overcome the quenching of triplet states by oxygen, Durandin *et al*. incorporated sensitizer and annihilator into poly(ethylene glycol)[26] doped with oleic acid (PEG-OA).[31] Lee *et al*. investigated the upconversion using methacrylate and methylmethacrylate (MMA)-linked annihilators with monomeric sensitizers in glassy material, the upconversion was observed at 32 mW cm^{-2}, which considered as upconversion at low power density in solid-state environment.[32] To achieve upconversion in a novel metal-free all-polymer system, Sittig *et al*. covalently integrated both sensitizer and annihilator to poly(methacrylate)s.[33] Edhborg *et al*. polymerized the annihilator molecule while sensitizer molecules were monomers.[34]

However, the impact of covalently linking only the sensitizer molecule into a polymer

backbone while the annihilator molecule remains monomer has not been yet investigated. Notably, such a strategy has proven to be advantageous for the photochemical generation of singlet oxygen ($^1O_2$) *i.e.* the polymerization of the sensitizer molecule enhanced the $^1O_2$ yield.[35,36] Because the triplet-triplet energy transfer (TTET) is a vital intermediate process of upconversion, polymerization could benefit the upconversion emission in a TTAUC system. This leads to the first objective of this thesis work to investigate the upconversion system in which the sensitizer has been polymerized while the annihilator molecules are monomers.

1.3.2 The Estimation of Viscosity of Lipid Bilayer

As described in the previous sections, diffusion plays a vital role in TTET and TTA processes. If the viscosity of a medium is high, diffusion of sensitizer and annihilator molecules will be slow; hence, energy transfer rates will also be slow;[10] however, if the viscosity of the medium reduces, energy transfer processes will be faster.[37] Therefore, it is vital to know the viscosity of the medium. The Stokes-Einstein model[38,39] describing the relation between rotational diffusion coefficient (D_R) and rotational relaxation times (τ_{rot}) is given in Equation 1.11 below:

$$D_R = \frac{1}{6\tau_{\mathrm{rot}}} = \frac{k_B T}{6\eta V} \qquad \text{Equation 1.11}$$

Where k_B represents the Boltzmann constant, T is the temperature, η the viscosity and V refer to the hydrodynamic volume of the molecule. It is evident that, the viscosity of the medium and rotational diffusion are inversely proportional to each other.

The rotational diffusion coefficient, rotational relaxation times as well as microviscosity of the mediums (lipid bilayer or biological cells) have been extensively investigated using time-resolved emission anisotropy (TEA).[38,40–57] However, this method provides information on the rotational diffusion of the molecule, if the rotational diffusion occurs within the timescale of the fluorescence lifetime (τ). If the fluorescence lifetime is much shorter than the depolarization timescale, then emission will decay to zero prior to depolarization; hence, emission anisotropy decay will not be able to reveal the full timescale of the depolarization *i.e.* rotational relaxation times. Similarly, when the emission timescale is much longer than the depolarization timescale then any change in depolarization will occur prior to fluorescence (decay of molecules from excited state), hence fluorescence decay will not be able to provide information on the anisotropy decay *i.e.* rotational relaxation times. For acquiring true

information on rotational relaxation times from fluorescence decay, the fluorescence lifetime and rotational relaxation time (depolarization time) have to be in the similar order of magnitude.[58,59]

In addition to the above-mentioned reasonings, many fluorophores might have reduced or quenched emission in specific environments,[60–62] *e.g.*, some of the BODIPY-derivatives are hydrophobic and non-emissive in aqueous environments.[63] The TTET and TTA processes, which occur in the triplet state of the molecule might also be non-emissive; therefore, TEA is not suitable to investigate the diffusion rates of the sensitizer and annihilator molecules in its triplet state.

In the above-mentioned situations, time-resolved absorption anisotropy (TAA) can be useful, since TAA is based on the absorption of the molecule, it can probe emissive as well as non-emissive molecules, hence complementing time-resolved fluorescence anisotropy (TEA) measurements to study rotational relaxation times. This leads to the second objective of this thesis to develop a transient absorption anisotropy setup and to investigate the rotational relaxation times of a fluorophore and microviscosity of the respective medium (discusses in the next section 1.3.3).

1.3.3 TTAUC in Light Activated Drug Release

In the context of light-activated drug release, Askes *et al*. synthesized sensitizer and annihilator reconstituted liposomes to generate blue light (*in situ*) by excitation of green or red light. Using a clinical-grade photodynamic laser source generating red light (630 nm), the liposomes produced blue light to activate ruthenium polypyridyl drug molecules from PEGylated liposomes. However, the drug release mechanism contained two-types of liposomes, one consisting of upconversion constituents and another light-activatable drug molecules, which caused the low efficiency of the drug activation.[6] In a following study to improve the efficiency of the drug release process, Askes *et al*. reconstituted liposomes with three components, porphyrin fluorophore as sensitizer, perylene dye as annihilator and light-triggered Ruthenium prodrug, which releases drug by sensing blue light. The sensitizer and annihilator molecules performed the upconversion process and produced a singlet excited state perylene species which transferred the energy to a nearby ruthenium-drug complex by fluorescence resonance energy transfer (FRET). The activation of the drug by FRET in a liposome consisting all three constituents made the process highly efficient.[25] Apart from the context of light-activated drug release, several other studies on TTAUC in lipid bilayer membranes are performed by the group of Prof. Sylvestre Bonnet,

University of Leiden; such as temperature-dependent upconversion studies on lipid bilayer membrane and three-dimensional imaging of a giant unilamellar vesicle (GUV).[37,64,65]

In all of the above-mentioned studies, TTAUC was performed in liposomes; however, the triplet state properties of the sensitizer and annihilator molecules in liposomes remained unknown. The triplet states are of vital importance since the energy transfer processes (TTET and TTA) take place in triplet states of sensitizer and annihilator.[9,10] The time-resolved study provides the characteristics of triplet states and energy transfer rates;[10] therefore, it is essential to perform time-resolved studies on liposomes reconstituted with sensitizer and annihilator molecules. The time-resolved study will also open the path to design the most efficient upconversion system in liposomes. This leads to the third objective of this thesis work to perform time-resolved studies on the liposomes reconstituted with sensitizer and annihilator molecules.

This objective leads to perform TTAUC in 1,2-dioleoyl-sn-glycero-3-phosphocholine (DOPC) lipid bilayer medium; therefore, rotational relaxation times of a relevant fluorophore (discussed in Chapter 4) and microviscosity of the DOPC lipid bilayer are chosen to be investigated using TTA for the aforementioned second objective.

1.4 Research Aims and Objectives

The scientific problems discussed in the context of TTAUC in section 1.3 leads to three main objectives summarized below:

(i) To understand the effect of confining sensitizer molecules into a macromolecule (polymer) where annihilator molecules are monomers in a triplet-triplet annihilation upconversion system.

(ii) To develop a transient absorption anisotropy setup and to measure the rotational relaxation times of a fluorophore using transient absorption anisotropy and to describe the application of the technique in solution and lipid bilayer membranes.

(iii) To investigate the excited state properties (emissive as well as non-emissive) of TTAUC constituents from solution to lipid bilayer membrane. To investigate the triplet formation in sensitizer molecules.

Based on the three objectives mentioned above, three chapters of the thesis are dedicated to each objective. (i) Chapter 3: Triplet-Triplet Annihilation Upconversion by Polymeric Sensitizer. (ii) Chapter 4: Investigation of Rotational Dynamics of

Fluorophores in Lipid Bilayer Membrane. (iii) Chapter 5: Triplet-Triplet Annihilation Upconversion in Lipid Bilayer Membrane.

The transient absorption anisotropy spectroscopy setup was developed to measure the ultrafast rotational dynamics of fluorophores in solution and lipid bilayer membrane. The development of the setup and instrumentation are described in Chapter 2. Three objectives are illustrated in Figure 1.2.

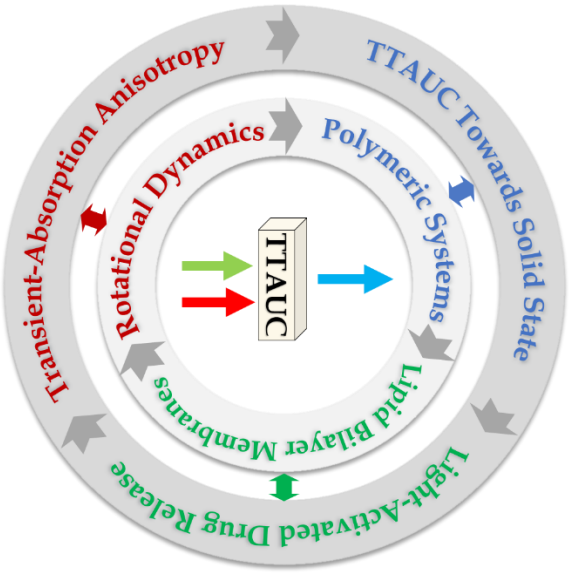

Figure 1.2: Schematic of the research aims and objectives.

1.5 The Characteristics of a TTAUC System

To investigate objectives 1 & 3, an in-depth understanding of a TTAUC system is required. For instance, what are the criteria for the selection of suitable sensitizer and annihilator molecules in a TTAUC system? How to determine the upconversion efficiency of a TTAUC system? What are the parameters to make an efficient TTAUC system? How to determine the triplet-triplet annihilation rate (k_{TTA}) in a TTAUC system? In this section, these questions about a TTAUC system are described. The characteristics of molecules for the selection as sensitizer and annihilator are described in this section. The upconversion efficiency to determine the efficiency, threshold power density (I_{th}) to examine the effectiveness of a TTAUC system and mixed kinetic analysis to determine the k_{TTA} are described in this section and its values for respective upconversion systems are discussed in Chapter 3.

1.5.1 Optimal Characteristics of the Sensitizer and Annihilator Molecules

The sensitizer needs to have qualities to perform efficient absorption, ISC and TTET

processes. Ideally, sensitizer should absorb in red to NIR region to fulfill the practical need of the TTAUC process. To maximize the absorption, the extinction coefficient (ε, $mol^{-1} \cdot cm^{-1}$) should be high over a broad range of wavelengths. For application in solar cells, the absorption of the sensitizer should ideally be beyond 900 nm where absorption of the commonly used Silicon (Si) solar cells reduces drastically.[18,20,21] For application in light-driven drug release, the absorption of the sensitizer is expected to be in the near-infrared (NIR) wavelength range which can penetrate deeper into the tissue.[6,25] To produce a large number of triplets, the sensitizer should have a high ISC. Organic sensitizers which have low ISC are substituted with heavy atoms (*e.g.* iodine and bromine) to achieve high triplet efficiency.[33,66,67] Metal complexes have high ISC (close to unity), hence used widely as sensitizers for many upconversion studies.[10,25,68–71] To efficiently transfer the triplet energy of the sensitizer to a nearby annihilator, the triplet lifetime of the sensitizer should be long *ca.* several microseconds. The singlet to triplet state energy gap should be small to minimize the energy loss by ISC.[8,9] The absorption band of the sensitizer should not overlap with the emission band of the annihilator to minimize the reabsorption losses.[8]

The annihilator should possess the virtue to participate efficiently in the TTET, TTA and fluorescence processes. For efficient TTET, the triplet energy level of the annihilator should be marginally lower than the triplet energy of the sensitizer. The triplet lifetime should be long (> 10 μs) to achieve high TTA, which is a pre-step to produce a singlet excited state annihilator needed to produce an anti-Stokes photon.[8,9] The first singlet state energy (E_{S1}) should be smaller than twice the first triplet state energy (E_{T1}) level. The difference between the first singlet state energy of the annihilator and sensitizer determines the blue shift of the upconversion process. To avoid forming quintet states, twice the first triplet state energy (E_{T1}) should be lower than the first quintet state energy (E_{Q1}). The fluorescence quantum yield (Φ_F) should be high (ideally near unity) to produce an anti-Stokes photon from its singlet state.[8,9]

1.5.2 Upconversion Efficiency

The absolute upconversion quantum yield (ϕ_{UC}) of the TTAUC depends on a series of processes (ISC, TTET, TTA, fluorescence) that occurs to produce an anti-Stokes shifted photon. Hence the upconversion efficiency depends on the efficiency of all the intermediate processes. The emission of an anti-Stokes shifted photon is achieved by the absorption of two low energy photons, hence the upconversion efficiency can be a maximum of 50%.[16] Equation 1.12 describes the upconversion yield:

$$\phi_{UC} = \frac{\phi_{ISC}\phi_{TTET}\phi_{TTA}\phi_F}{2}$$ Equation 1.12

Where ϕ_{ISC} is the intersystem crossing yield, ϕ_{TTET} is the triplet-triplet energy transfer yield, ϕ_{TTA} is the triplet-triplet annihilation yield and ϕ_F is the fluorescence quantum yield of the annihilator.

The intersystem crossing yield ϕ_{ISC}, which is close to unity for many of the sensitizers depends upon the ratio of sensitizers in the first triplet excited state ($^3S^*$) to sensitizers in its first singlet excited state ($^1S^*$), the maximum number of sensitizer molecules in singlet and triplet excited state is to be considered for the calculation of yield (ϕ_{ISC}). It is described using Equation 1.13, given below:

$$\phi_{ISC} = \frac{numbers\ of\ \ ^3S^*}{numbers\ of\ \ ^1S^*}$$ Equation 1.13

The triplet-triplet energy transfer yield ϕ_{TTET} depends upon the quenching rate of the sensitizer in the presence of annihilator (k_{TTET}) and the intrinsic decay rate of the sensitizer (k_T),[16] it is described using Equation 1.14, given below:

$$\phi_{TTET} = \frac{k_{TTET}[\ ^1A]}{k_{TTET}[\ ^1A] + k_T}$$ Equation 1.14

When the decay kinetics of the triplet sensitizer is first order, then the triplet-triplet energy transfer yield depends on the concentration of annihilator. With the increase of annihilator concentration, the lifetime and emission intensity of the sensitizer decreases, this change in intensity or lifetime with respect to annihilator concentration is plotted as Stern-Volmer plot.[16,59] The lifetime and emission intensity of the sensitizer decrease due to energy transfer from sensitizer to annihilator molecule; [16,59] hence, the ϕ_{TTET} can be obtained using information from the Stern-Volmer plot described using Equations 1.15 and 1.16:

$$\phi_{TTET} = 1 - \frac{I}{I_0}$$ Equation 1.15

$$\phi_{TTET} = 1 - \frac{\tau}{\tau_0}$$ Equation 1.16

Where I and I_0 are the phosphorescence intensity of the sensitizer with and without

the presence of an annihilator or quencher respectively, τ and τ_0 are the lifetimes of the sensitizer with and without the presence of annihilator. Equation 1.15 can also be used to calculate the fluorescence quenching of fluorophores by a quencher, as explained in Chapter 2 (see Equation 2.4).

The triplet-triplet annihilation yield (ϕ_{TTA}) is the efficiency of $^1A^*$ generation from available $^3A^*$, this step determines the maximum upconversion yield (ϕ_{UC}) to be 0.5. It depends on two factors, the proportion of $^3A^*$ that participate in the second-order annihilation process and the efficiency of the annihilator pair yielding an excited singlet $^1A^*$, this factor is also known as f (statistical probability).[16,72] To calculate the ϕ_{TTA}, maximum number of the $^1A^*$ and $^3A^*$ generated are considered; it described using Equation 1.17:

$$\phi_{TTA} = \frac{numbers\ of\ \ ^1A^*}{numbers\ of\ \ ^3A^*} \qquad \text{Equation 1.17}$$

The fluorescence quantum yield of annihilator (ϕ_F) molecules is the ratio of photons generated to number of singlet excited $^1A^*$ present in the medium,[16,72] described as Equation 1.18 below:

$$\phi_F = \frac{numbers\ of\ photon\ generated}{numbers\ of\ \ ^1A^*} \qquad \text{Equation 1.18}$$

There are a few more factor that affects the overall upconversion yield of the TTAUC process, such as reverse intersystem crossing which can reduce the number of triplet sensitizer participating in the energy transfer process. The presence of oxygen is a crucial factor in the efficiency of upconversion, since the triplet species (both sensitizer and annihilator) are quenched by the presence of oxygen, hence the medium should be oxygen-free to obtain a high yield.[67,73–75] The generated anti-Stokes shifted photons may be reabsorbed by the ground state sensitizer molecule,[72] these photons are generated but not observed by the detector. The excited singlet annihilator ($^1A^*$) may transfer its energy to ground state sensitizer, hence appear as a loss; it may be utilized in applications, such as light-activated drug release.[25] Minimizing the mutual overlap of absorption spectra of sensitizer and emission spectra of annihilator can significantly reduce the loss by reabsorption and energy transfer.[10,33] Two annihilators in the first excited triplet state ($^3A^*$) may form one higher excited triplet state ($^3A_n^*$) by TTA; but dissociation of the higher triplet state leads to only one triplet excited state (*i.e.*, $^3A^*$ +

$^3A^* = {}^3A_n^* + {}^1A$ and $^3A_n^* \longrightarrow {}^3A^*$); the process of forming one higher triplet state ($^3A_n^*$) by two $^3A^*$ but dissociation to only one $^3A^*$ also appears as a loss in the TTAUC mechanism, see the next section for details. Any other impurity present in the medium may participate in absorption or scattering of the excitation photons, which brings down the light-harvesting by sensitizer hence, the medium under study should be free of impurities to obtain high upconversion quantum yield, details are depicted in the Figure 1.3.[72]

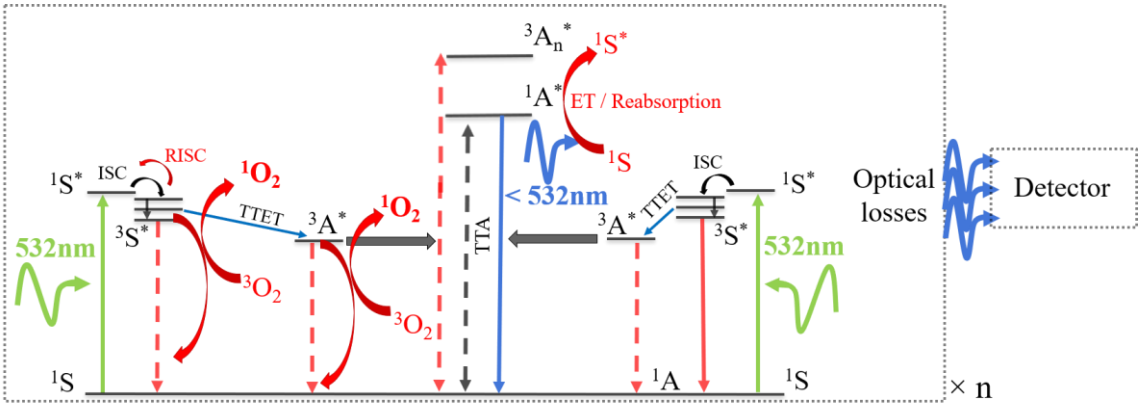

Figure 1.3: Loss mechanism of TTAUC. The red arrows (dashed lines and curved arrows) depict nonproductive and loss mechanisms.

1.5.3 Spin Statistics of TTA

The TTA of two $^3A^*$ provides a singlet $^1A^*$ that fluoresces an anti-Stoke-shifted photon. However, the encounter of two $^3A^*$ may form singlet (spin multiplicity = 1), triplet (spin multiplicity = 3), or quintet (spin multiplicity = 5) species due to tensor product (3×3) of the initial spin multiplicity (3). The probability of forming each spin state is according to the ratio of their spin *i.e.* 1:3:5 for singlet, triplet and quintet respectively.[76–79] This indicates that only one of nine $^3A^*$ will form $^1A^*$, hence, the efficiency can be a maximum 1/9. However, the experimental results show that the maximum efficiency can be much higher than 11.1%.[80,81]

$$^3A^* + {}^3A^* \rightleftharpoons \begin{cases} {}^1[{}^3A{}^3A]^* \longrightarrow {}^1A^* + {}^1A & \text{Equation 1.19} \\ {}^3[{}^3A{}^3A]^* \longrightarrow {}^3A^{**} + {}^1A & \text{Equation 1.20} \\ {}^5[{}^3A{}^3A]^* & \text{Equation 1.21} \end{cases}$$

The upconversion efficiency higher than the spin statistical limit becomes possible because the formed quintet complex breaks away into two triplet species ($^3A^*$), which

can again participate in forming ^{1}A*. The dissociation of the quintet complex takes place due to its very high energetic condition.[79,82] The annihilator molecule at its second excited triplet state (^{3}A**) also relaxes back to the first triplet excited state, where the triplet molecule can again participate in forming a singlet (^{1}A*). Therefore, the dissociation and internal fast relaxation populate the triplets, which enhances the overall upconversion efficiency of the process. Taking the energy level consideration of the annihilator molecule, the efficiency can be achieved beyond the spin statistical limit by making (i) twice its first triplet excited state energy level greater than the energy level of its first singlet excited state, *i.e.* $E_{T1} \geq E_{S1}/2$ (ii) twice of its first triplet excited state energy level should be always smaller than its second triplet excited state energy level or quintet state, *i.e.* $2 \times E_{T1} < E_{T2}$ and $2 \times E_{T1} < E_{quintet}$.[16,83–85]

1.5.4 Threshold Power Density

The upconversion emission intensity of the TTAUC depends on the excitation power density. The upconversion emission photon is a product of two excitation photons, hence, with an increase of the excitation intensity the emission intensity rises quadratically. However, beyond a certain threshold value of excitation power density, the relation between the excitation power density and emission intensity becomes linear. This threshold value is known as threshold power density (I_{th}).[86] The region below I_{th} is called weak annihilation regime and beyond I_{th} is called strong annihilation regime. This is because the triplet annihilators (^{3}A*) in the weak annihilation regime decay predominantly via triplet intrinsic decay (k_T^A, first-order decay) but in strong annihilation regime, triplet annihilators decay predominantly via triplet-triplet annihilation (k_{TTA}, second-order decay).[85–89] The efficiency of triplet-triplet annihilation (ϕ_{TTA}) reaches 50% of its maximum at I_{th}, hence the TTAUC system is designed to have a low value of I_{th} to provide high efficiency of the system at low excitation power density.[17,86,88] The low value of I_{th} is vital when TTAUC is implemented in solar cells, the TTAUC system with low I_{th} implemented in the solar cell will harness photons efficiently at low excitation power density comparable to radiation received by solar cells since the AM 1.5 one-sun illumination (475-575 nm region) is *ca.* 10 mW·cm^{-2}.[90–93]

The linear relationship between the excitation power density and upconversion emission intensity (I_F) can be further understood using the triplet decay rate equation suggested by Bachilo and Weisman:[79,83]

$$\frac{\mathrm{d}\sqrt{I_F(t)}}{\mathrm{d}t} \propto \frac{\mathrm{d}\left[{}^3A^*\right]_t}{\mathrm{d}t} = -k_T^A \left[{}^3A^*\right]_t - k_{TTA}\left[{}^3A^*\right]_t^2 \qquad \text{Equation 1.22}$$

The triplet annihilator molecule decays by two distinct pathways (i) the second-order bimolecular decay by triplet-triplet annihilation, kinetically characterized by the second-order rate constant k_{TTA} and (ii) the unimolecular decay, kinetically characterized by the first-order rate constant k_T^A. It consists of all pseudo first-order processes such as triplet quenching by oxygen molecules and intrinsic decay of the excited triplet annihilator (k'_T).[17,83] The analytic solution to Equation 1.22 is given as:[9,79,94]

$$\left[{}^3A^*\right]_t = \left[{}^3A^*\right]_0 \frac{1-\beta}{e^{k_T^A \cdot t} - \beta} \qquad \text{Equation 1.23}$$

$$\beta = \frac{k_{TTA}\left[{}^3A^*\right]_0}{k_T^A + k_{TTA}\left[{}^3A^*\right]_0} \qquad \text{Equation 1.24}$$

$[^3A^*]_0$ is the initial excited triplet concentration of the annihilator, $[^3A^*]_t$ is time dependent excited triplet concentration of the annihilator which decays due to pathways k_{TTA} and k_T^A. The dimensionless parameter β is the fraction of $[^3A^*]_0$ that decays through triplet-triplet annihilation.[79,83] When the upconversion system is in the weak annihilation regime, first-order processes are dominating in the decay of $^3A^*$, then $k_T^A > k_{TTA}\,[^3A^*]$, substituting in the Equation 1.23 reveals

$$\left[{}^3A^*\right]_t = \left[{}^3A^*\right]_0 e^{-k_T^A \cdot t} \qquad \text{Equation 1.25}$$

The upconversion emission intensity (I_F) is proportional to the square of the excited triplet annihilator concentration [^{3}A*] and can be written[17] as

$$I_F = \int_0^\infty I_F(t)\,\mathrm{d}t = \int_0^\infty \phi_F k_{TTA}\left[{}^3A^*\right]_t^2 \qquad \text{Equation 1.26}$$

Where ϕ_F is the fluorescence quantum yield of the annihilator.

Substituting Equation 1.25 in Equation 1.26, resulting integration yields

$$I_F = \frac{\phi_F k_{TTA}\left[{}^3A^*\right]_0^2}{2k_T^A} \qquad \text{Equation 1.27}$$

It is clear from Equation 1.27 that upconversion emission intensity is proportional to the square of the excited triplet concentration of annihilator ($[^3A^*]^2$), hence the relationship between excitation power density and upconversion fluorescence intensity is quadratic dependent in weak annihilation regime. However, if the upconversion system is in strong annihilation regime, second-order decays are dominating in the decay of $^3A^*$, hence, $k_T^A < k_{TTA}$ $[^3A^*]$,[17,79] substituting in Equation 1.23 reveals

$$\left[{}^3A^*\right]_t = \frac{\left[{}^3A^*\right]_0}{1 + t \times k_{TTA}\left[{}^3A^*\right]_0} \qquad \text{Equation 1.28}$$

Substitution of Equation 1.28 in Equation 1.26 and integration over time simplifies the upconversion fluorescence intensity (I_F) to

$$I_F = \phi_F \left[{}^3A^*\right]_0 \qquad \text{Equation 1.29}$$

It is clear from Equation 1.29 that, the upconversion emission intensity is proportional to the concentration of the excited triplet annihilator $[^3A^*]$, which successively makes upconversion fluorescence intensity linearly dependent on the excitation power density.[17,84,86,95]

The threshold power density I_{th} (photons $\cdot$ s^{-1} $\cdot$ cm^{-1}) can be described using Equation 1.30, given below:

$$I_{th} = \frac{(k_T^A)^2}{2\phi_{TTET}\,\alpha[{}^1S]\,k_{TTA}} \qquad \text{Equation 1.30}$$

Where ϕ_{TTET} is the efficiency of energy transfer from triplet sensitizer to ground state annihilator, $\alpha[^1S]$ is the absorption cross-section of the sensitizer in cm^{-1} at the excitation wavelength.[8,17,86,96]

1.5.5 Mixed Kinetic Analysis

There are several processes in a TTAUC system and the rate governing each of the

processes is described using a rate constant, the ISC is denoted as k_{ISC}, the intrinsic decay of the sensitizer molecule is denoted as k_T, triplet-triplet energy transfer is denoted with k_{TTET}, unimolecular decay of the annihilator molecule is denoted with k_T^A and bimolecular decay of the annihilator via triplet-triplet annihilation (TTA) is denoted with k_{TTA}. The k_{ISC} is determined using femtosecond transient absorption measurement (fs-TA), since $S_1 \rightarrow T_1$ takes place in sub-nanosecond to a few nanosecond timescales. The k_T is determined using nanosecond transient absorption (ns-TA) or nanosecond transient emission (ns-TE) measurement; since the triplet lifetime of the sensitizer molecule is expected to be several microseconds. The k_{TTET} is determined using the Stern-Volmer plot made from the quenching experiments performed using ns-TA or ns-TA. The k_T^A and k_{TTA} are obtained using the ns-TA or ns-TE measurements but involve kinetic modeling called mixed kinetic analysis described below.

The triplet annihilator molecules decay by two distinct pathways as described using Equation 1.22 in the previous section. Substituting Equation 1.24 in Equation 1.25 reveals Equation 1.31 for the time-dependent triplet concentration of the annihilator.[83,97–99]

$$\left[{}^3A^*\right]_t = \frac{e^{-k_T^A \cdot t}}{1+\left[{}^3A^*\right]_0 \times \frac{k_{TTA}}{k_T^A} \times (1-e^{-k_T^A \cdot t})} \qquad \text{Equation 1.31}$$

Using the nanosecond transient absorption decay kinetics of the annihilator and fitting into Equation 1.31, the rate of unimolecular decay (k_T^A) and bimolecular decay (k_{TTA}) can be obtained. The transient emission decay kinetics can also be used to obtain both the rates using the rewritten Equation 1.23 and Equation 1.31 below:

$$\frac{\left[{}^3A^*\right]_t}{\left[{}^3A^*\right]_0} = \frac{e^{-k_T^A \cdot t}}{1+\left[{}^3A^*\right]_0 \times \frac{k_{TTA}}{k_T^A} \times (1-e^{-k_T^A \cdot t})} \qquad \text{Equation 1.32}$$

The normalized square of the transient emission decay kinetics can be fitted into Equation 1.32 to obtain both rate constants.[83,99]

1.6 Anisotropy of Fluorophores

To investigate the rotational dynamics of a fluorophore (aforementioned objective 2) time-resolved emission anisotropy (TEA) and transient absorption anisotropy (TAA)

measurements are employed. Therefore, an in-depth understanding of anisotropy and its interpretation is essential. In this section, the anisotropy in an isotropic medium and its analysis methods are described; which is used to analyze the anisotropy measurements of the investigated molecules given in Chapter 4.

1.6.1 Photoselection of Molecules

The probability that a molecule absorbs a photon to reach its first excited state, is proportional to $\cos^2\theta$, θ being the angle between the electric field vector of the incoming photon and the absorption transition dipole moment of the molecule. When a sample consisting of a large number of molecules is excited with a light of definite polarization, the molecules within the excitation focal volume of the incident light having their absorption transition dipoles aligned to the electric field vector of the excitation light are more prone to get excited and to reach its excited state. This selective excitation of the molecules is called photoselection, illustrated in Figure 1.4.[40,58,100,101] Due to excitation by the polarized light and selective excitation (photoselection) of the molecules, the emission from the molecules is also partially polarized.[41,59]

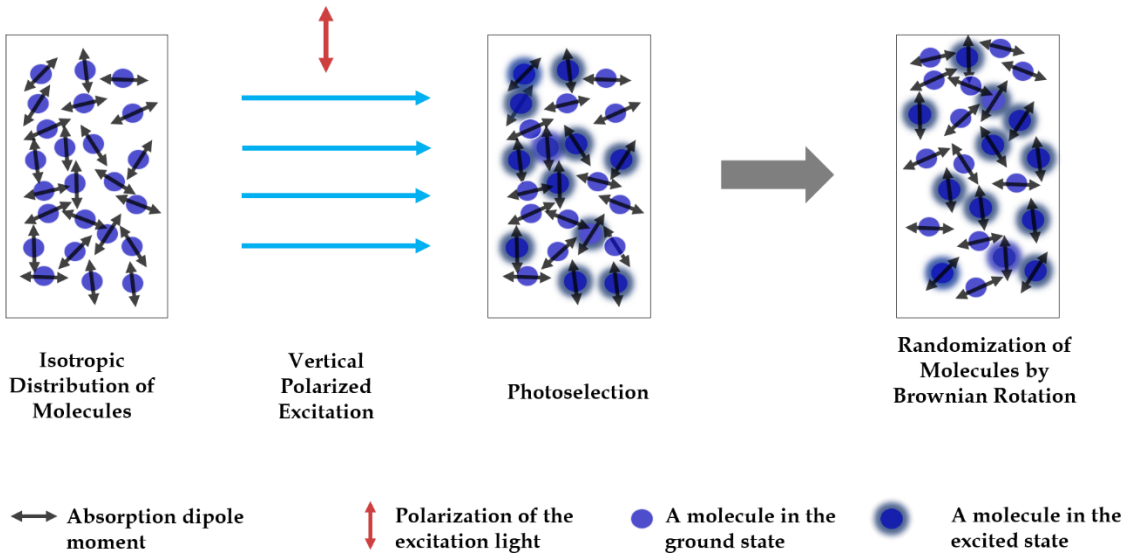

Figure 1.4: Photoselection of the random population of molecules by vertically polarized light, followed by rotational Brownian diffusion

1.6.2 Fluorescence Anisotropy

The emitted light from molecules is measured by passing it through an analyzer placed between the sample and the detector. The emission intensity measured by the

detector when the analyzer angle is identical to the excitation polarization light is called I_{ll}, and when the detector angle is perpendicular to the excitation polarization light is $I_{\perp}$., depicted in Figure 1.5. Using the emission intensity in parallel and perpendicular directions, fluorescence anisotropy is calculated using Equation 1.33, given below:[59]

$$r = \frac{I_{ll} - I_{\perp}}{I_{ll} + 2 \times I_{\perp}} \qquad \text{Equation 1.33}$$

When the molecules are immobile in the medium *i.e.* Brownian diffusion is restricted, then the anisotropy of the molecule remains constant to initial anisotropy (r_0) and is calculated using Equation 1.34, given below:

$$r_0 = \frac{3\cos^2\xi - 1}{5} \qquad \text{Equation 1.34}$$

Where ξ is the angle between absorption and emission dipole moments.

However, when the molecules are free to diffuse in the medium, the rotational diffusion of the molecule happens on a similar timescale as the fluorescence lifetime, which causes a gradual displacement of the emission dipole, consequently depolarizing the emission light. Due to gradual depolarization of the emitted light, the anisotropy starts decaying from its maximum value (r_0). This can be used to extract information about the rotational diffusion of the molecules under observation.[58,100,102–104]

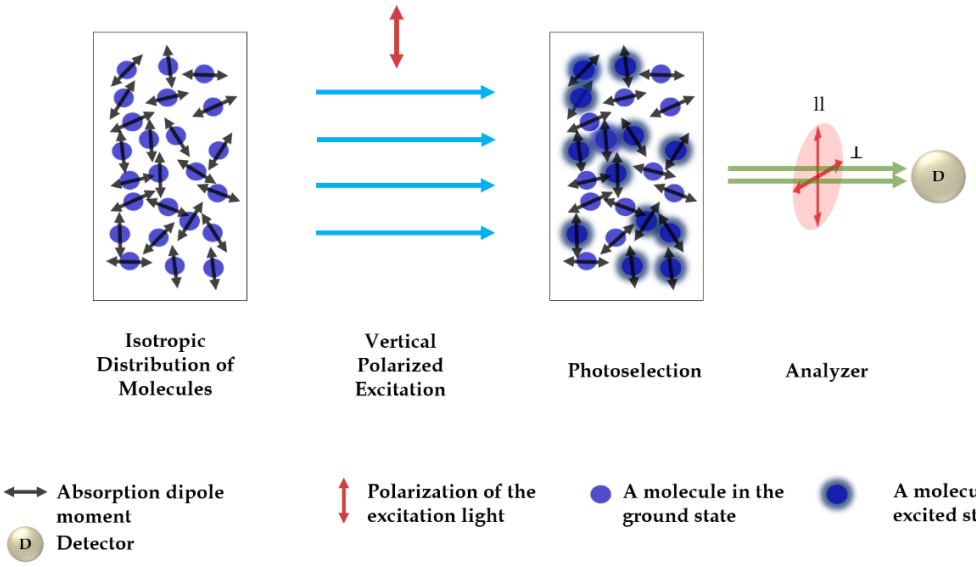

Figure 1.5: The measurement of anisotropy using an analyzer at parallel and perpendicular to the excitation polarization.

The fluorescence anisotropy is analyzed using steady-state and time-resolved anisotropy techniques. The steady-state anisotropy is obtained by exciting the sample continuously and emission is collected until a good signal-to-noise ratio is obtained. It provides a time-average of the anisotropy and is helpful in quantitative and qualitative analysis of the orientation, shape and size of the molecule.[59] This technique has found application in the investigation of binding and folding of the protein.[59] The time-resolved emission anisotropy (TEA) tracks the changes in the orientation of the molecules occurring to the rotational diffusion. When a molecule is attached to a large protein or polymer, the steady-state and time-resolved anisotropy provide the same details but time-resolved anisotropy analysis can distinguish the intramolecular motions. The time-dependent magic angle fluorescence intensity (*I(t)*), steady-state anisotropy (*r*), time-resolved anisotropy (*r(t)*) are described using equations given below:[59]

$$I(\mathrm{t}) = \frac{\mathrm{I_{ll}}\,(t) \;+\; 2 \times \mathrm{I_{\perp}}(t)}{3} \qquad \text{Equation 1.35}$$

$$r \;= \frac{\int_0^{\infty} r(t)\, I(t)\, \mathrm{d}t}{\int_0^{\infty} I(t)\, \mathrm{d}t} \qquad \text{Equation 1.36}$$

$$r\,(t) = \frac{\mathrm{I_{ll}}\,(t) \;-\; \mathrm{I_{\perp}}(t)}{\mathrm{I_{ll}}\,(t) \;+\; 2 \;\times\; \mathrm{I_{\perp}}\,(t)} \qquad \text{Equation 1.37}$$

The decay of time-resolved anisotropy for a rigid spherical molecule having one rotational relaxation time-constant (τ_c) is modeled using Equation 1.38, given below:

$$r\,(t) = \; r_0\, \mathrm{e}^{-t/\tau_c} \qquad \text{Equation 1.38}$$

However, when a molecule is non-spherical (*e.g.* ellipsoid or macromolecules) or has more than one rotational relaxation time, the decay of time-resolved anisotropy can be modeled using Equation 1.39, given below:

$$r\,(t) = \sum_{j=1}^{5} r_{0j}\; \mathrm{e}^{-t/\tau_{cj}} \qquad \text{Equation 1.39}$$

Here r_{0j} and τ_{cj} are the preexponential coefficients and rotational relaxation times of j^{th} anisotropy decay to the overall anisotropy of the molecule. These are complex

functions of the rates of rotation around the nonsymmetric body's molecular axes as well as the relative angle of the absorption and emission transition dipoles to these axes. As a result, anisotropy decay contributions are a useful method to study multi segmental mobility of a macromolecule or to obtain the multiple rotational characteristics of an ellipsoid. For an asymmetric body, a maximum of five rotational relaxation times can be present. But, due to the close similarity between two pairs of rotational relaxation times, only three can be resolved by an experimental measurement criterion. Molecules resembling the shape of an ellipsoid can be modeled as elongated (prolate) or flattened (oblate) ellipsoids, which have two identical axes and one distinct axis. Such models can have a maximum of three rotational relaxation times.[41,59,105]

1.7 Structure and Outline of this Work

In Chapter 1, triplet-triplet annihilation upconversion (TTAUC) and its potential applications are described. The scientific problems in the application of TTAUC lead to the objectives of this thesis work, which are described in section 1.3. The background theory of TTAUC is described in section 1.5. The anisotropy, which is the background of objective 2 is described in section 1.6. In the next chapters, spectroscopic methods and objectives of the thesis are investigated. The content of the chapters is described below.

Chapter 2: Spectroscopic Methods

To investigate the objectives mentioned in section 1.4 both steady-state and time-resolved spectroscopic techniques are required, hence both techniques were employed. In this chapter, a brief details of UV-Vis absorption spectroscopy, emission spectroscopy are given. Time-resolved spectroscopic methods such as transient absorption spectroscopy and transient emission spectroscopy to measure processes occurring from sub-picosecond to millisecond timescales were employed for the experiments; therefore, briefly described. To measure the rotational relaxation times of non-emissive states and non-emissive molecules transient absorption anisotropy set up was developed.

Chapter 3: Triplet-Triplet Annihilation Upconversion by Polymeric Sensitizer

In Chapter 3, the first objective "the effect of confining sensitizer molecules into a macromolecule (polymer) on the triplet-triplet annihilation upconversion" has been investigated. The steady-state and time-resolved properties of polymer-bound

sensitizers are compared with their monomeric counterpart with and without annihilator molecules. The effect of confinement on the energy transfer processes has been investigated and applications of the polymeric sensitizers have been suggested. The schematic representation of the objective is shown in Figure 1.6. The excitation wavelength in green and emission wavelength in blue depicts excitation by longer wavelength with respect to emission.

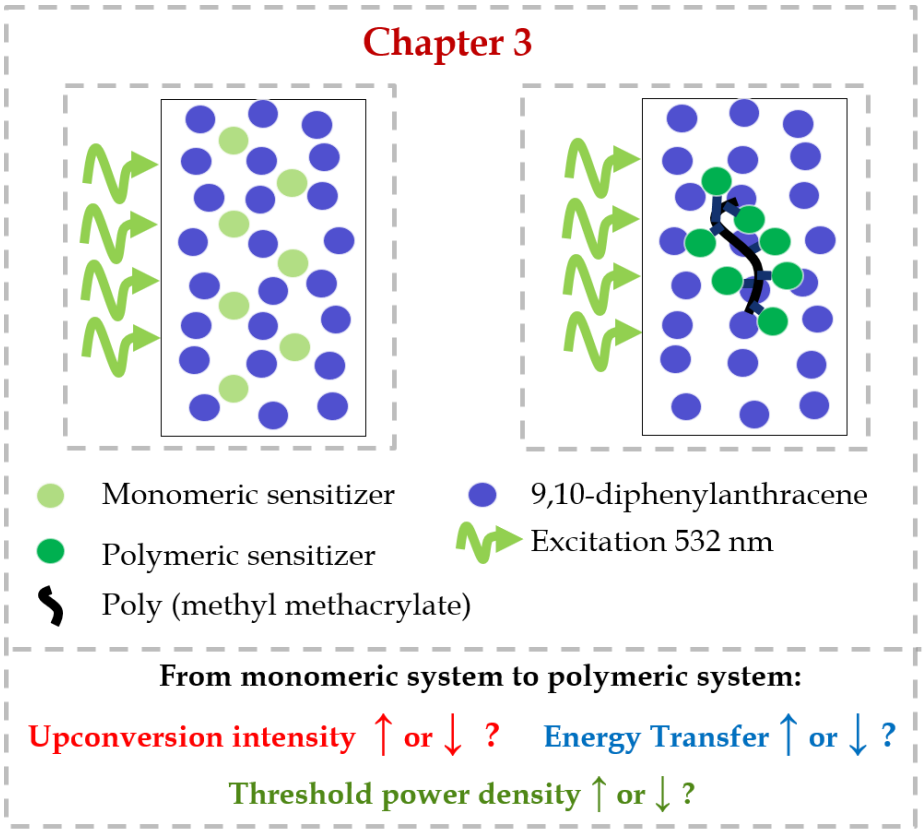

Figure 1.6: The schematics of the objective of Chapter 3: TTAUC using polymeric sensitizers.

Chapter 4: Investigation of Rotational Dynamics of Fluorophore in Lipid Bilayer Membranes

In Chapter 4, the second objective "to measure the rotational relaxation times of a fluorophore using transient absorption anisotropy" and "to describe the application of the technique in solution and lipid bilayer membranes" have been investigated. The development of the transient absorption anisotropy is described in Chapter 2. The advantage of transient absorption anisotropy over transient emission anisotropy is discussed. The rotational relaxation times of BODIPY-molecule in solution and lipid bilayer membrane have been obtained using transient emission and transient absorption anisotropy. The schematic representation of the objective is shown in Figure 1.7.

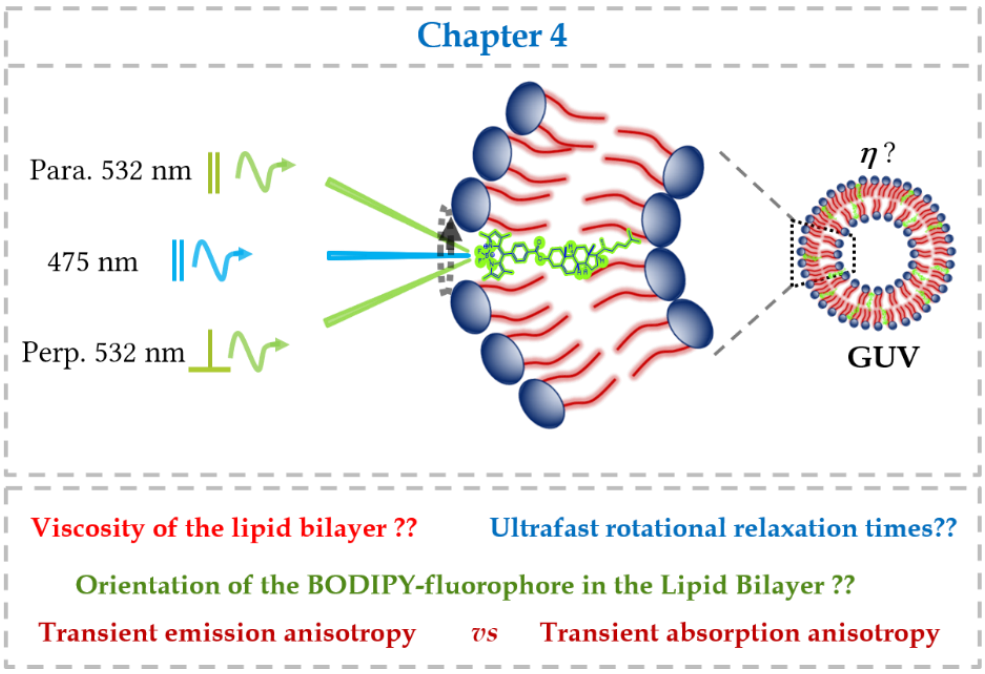

Figure 1.7: The schematics of the objective of Chapter 4: investigation of the rotational dynamics by transient absorption anisotropy. Para: parallel, Perp: perpendicular. The circular arrow depicts the rotation of the BODIPY-fluorophore in the lipid bilayer.

Chapter 5: TTAUC in Lipid Bilayer Membrane

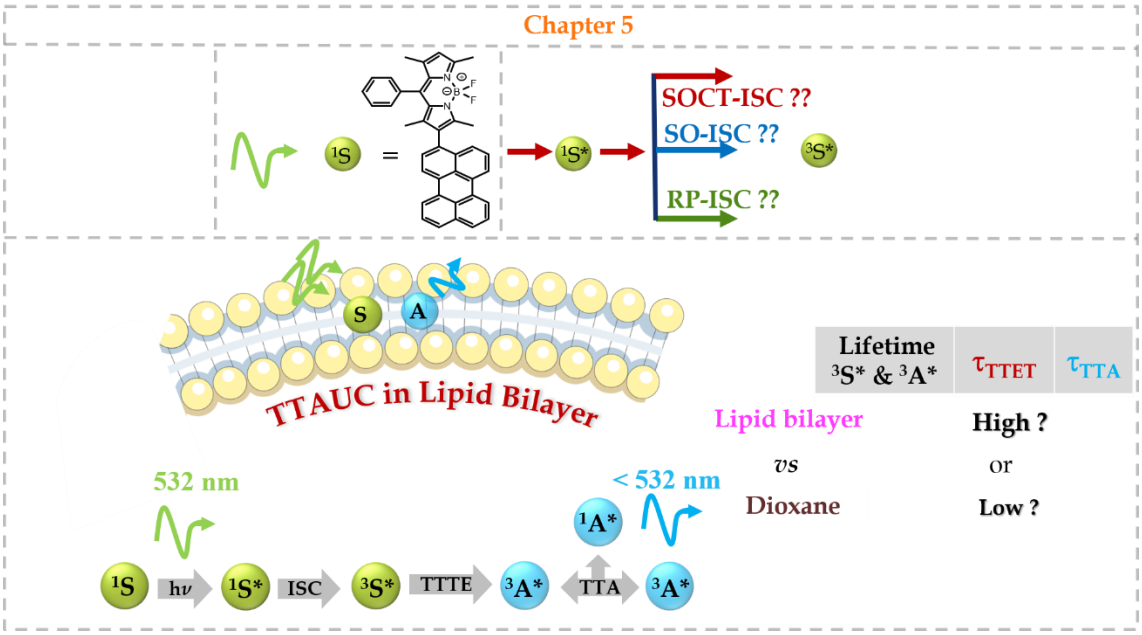

Figure 1.8: The schematics of the objective of Chapter 5: TTAUC in the lipid bilayer membrane. Singlet to triplet formation pathway: SOCT-ISC- spin-orbit charge transfer intersystem crossing or SO-ISC- spin-orbit coupling intersystem crossing or RP-ISC- radical-pair intersystem crossing. Investigation of triplet lifetime of sensitizer and annihilator molecules in solution and lipid bilayer. S: sensitizer and A: annihilator.

In Chapter 5, the third objective "to investigate the excited state properties (emissive as well as non-emissive) of the TTAUC constituents (sensitizer and annihilator) from solution to lipid bilayer membrane" and "to investigate the triplet formation in sensitizer molecules" have been investigated using femtosecond transient absorption spectroscopy and nanosecond transient absorption spectroscopy, as well as using computational simulations. The schematic representation of the objective is shown in Figure 1.8.

2. Spectroscopic Methodology

In a TTAUC system, initiating from absorption of red photons to generation of blue photons several photophysical processes take place, which vary on a time-scale from sub-picosecond to hundreds of microseconds. The photophysical processes (*e.g.* absorption, fluorescence, intersystem crossing) are described using Equations 1.1-1.10 in Chapter 1. These processes can be investigated using measurement techniques described in this chapter. First, a brief overview of these processes is given; thereafter the measurement techniques, steady state, time-resolved spectroscopic methods, polarization resolved confocal microscopy, synthesis of lipid bilayer and computational methods are described.

2.1 Photophysical Processes

The photoexcitation of a molecule leads to several energy transfer and dissipation processes, which can be easily understood using the Jablonski diagram shown in Figure 2.1.

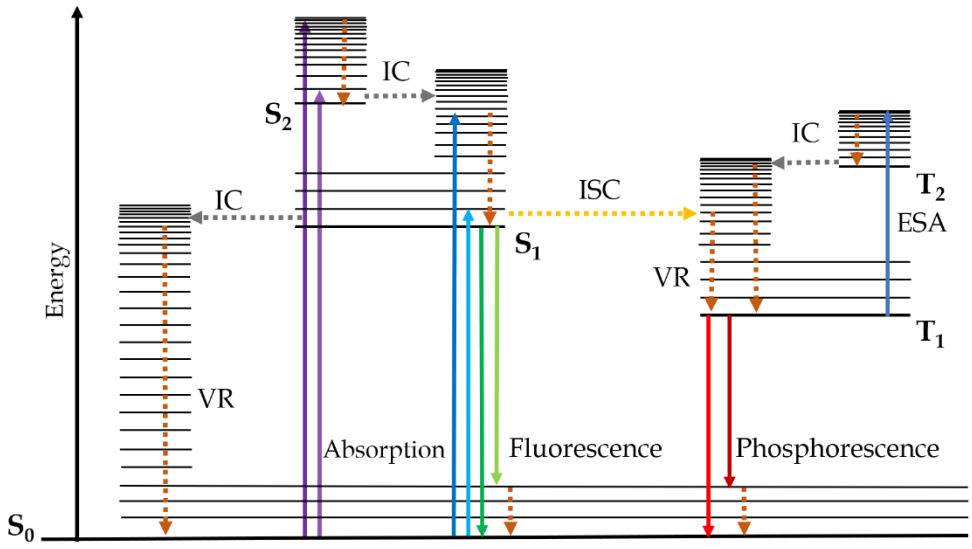

Figure 2.1: Jablonski diagram of energy transfer processes. The straight arrows represent radiative processes, while the dashed arrows represent nonradiative transitions. Upward arrows in violet and blue represent absorption. The acronyms are S_0: singlet ground state, S_1: first singlet excited state, S_2: second singlet excited state, T_1: first triplet excited state, T_2: second triplet excited state, ESA: excited state absorption, **VR**: vibrational relaxation (shown in brown), ISC: intersystem crossing (yellow), **IC**: internal conversion (grey).

Absorption is a very fast (~ 10^{-18} to 10^{-15} s) process, originating from the lowest vibrational state since most molecules remain in the lowest energy level (electronic

ground state) at room temperature. Upon absorption, molecules reach upper vibrational levels of the electronic excited state. The vibrational levels of the two electronic states are chosen by the most significant overlap of the two vibrational wave functions and this is also known as the Frank-Condon principle.[59,106]

According to Kasha's rule, radiative emission of a given spin-multiplicity will always occur from the lowest excited state of the same spin-multiplicity. Hence, nonradiative relaxation from upper vibrational levels to the lowest vibrational level occurs within the same electronic state and is known as *vibrational relaxation* (**VR**). The energy dissipated in the vibrational relaxation results in heat transfer to the environment (surrounding molecules) by collisional interactions. This process can range from ~ 10^{-14} to 10^{-12} s and depends on the phase of the medium.[106]

The relaxation from an electronic state's vibrational level to another electronic state's vibrational level of the same spin-multiplicity manifold is known as *internal conversion* (**IC**). This process depends on the energy gap between excited electronic states; if the gap is small between two electronic states, then an overlap of vibrational levels from two electronic states occurs, which facilitates the internal conversion. This process occurs in a similar time scale as vibrational relaxation.[59]

The radiative emission from a molecule, due to the transition from the lowest excited state to the ground state without a change in the spin-multiplicity ($S_1 \rightarrow S_0$) is known as *fluorescence*. This is relatively a slow process with respect to vibrational relaxation and internal conversion and ranges from 10^{-9} to 10^{-7} s, hence at higher electronic energy levels vibrational relaxation and internal conversion will take place first to bring the molecule to its lowest electronic excited state, where fluorescence takes place. The wavelength of an emitted photon depends on the difference in the energy gap between excited and ground-state energy levels. Due to vibrational relaxation and internal conversion, some energy is lost prior to fluorescence, hence the emitted photon is of lower energy or longer wavelength (red-shifted / Stokes-shifted) with respect to the absorbed photon. There are numerous vibrational levels within an electronic energy level, hence emitted photons are distributed over a wavelength range accordingly.[59]

The average time a molecule spends in an excited state before returning to the ground state is known as the lifetime of the excited state (τ).[59]

$$\tau = \frac{1}{k_r + k_{nr}} \qquad \text{Equation 2.1}$$

Here, k_f is the radiative decay rate constant, k_{nr} is the nonradiative decay rate constant,

which includes the rate of internal conversion (k_{IC}), rate of intersystem crossing (k_{ISC}) and nonradiative quenching.

The fluorescence *quantum yield* (Φ_F) is the ratio of the number of photons emitted to the number of photons absorbed.[59] The relative quantum yield (ϕ_f^S) obtained experimentally using quantum yield, absorbance and emission spectrum of a reference; the Φ_F and ϕ_f^S are described using Equations 2.2 and 2.3 respectively:[107]

$$\Phi_F = \frac{k_f}{k_f + k_{nr}} \qquad \text{Equation 2.2}$$

$$\phi_f^S = \phi_f^R \times \frac{n_S^2}{n_R^2} \times \frac{I_S \times \left(1 - 10^{-A^R}\right)}{I_R \times \left(1 - 10^{-A^S}\right)} \qquad \text{Equation 2.3}$$

When the radiative rate constant is much higher than the nonradiative rate constant, the quantum yield approaches unity.[59] ϕ_f^R is the quantum yield of reference, ϕ_f^S is the relative quantum yield of the sample, I_S and I_R are emission intensity of the sample and reference respectively; A^S and A^R are absorbances of the sample and reference respectively at the excitation wavelength, n_S and n_R are the refractive indexes of the sample and reference respectively.[107]

The radiative emission from a molecule due to the transition from the lowest triplet excited state to the ground state with a change in spin-multiplicity (*e.g.* $T_1 \rightarrow S_0$) is known as *phosphorescence*. This is a forbidden transition because it involves a change in spin multiplicity; therefore, it is a slow process occurring at a timescale of 10^{-6} to a few seconds.

The non-radiative transition with a change in spin-multiplicity from a singlet excited state to a triplet excited state (*e.g.* $S_1 \rightarrow T_1$) is known as *intersystem crossing* (ISC). This is also a forbidden and slow transition due to changes in spin multiplicity. However, it occurs through spin-orbit coupling, the mixing of states from spin angular momenta and orbital angular momenta make this transition possible since both have the same total angular momentum. The ISC is poor in most organic molecules, the substitution of a heavy atom enhances the spin-orbit coupling strength, which reflects in higher intersystem crossing.[108,109]

Energy transfer (*ET*) between two molecules takes place by molecular contact.[59,110] The photoexcited molecule at its singlet excited state goes to its triplet state by ISC, where the molecule may participate in ET by transferring its spin and energy to a nearby

ground state molecule (Figure 2.2). The triplet-triplet energy transfer (TTET) is an analogous process to Dexter exchange coupling;[111,112] it occurs with the exchange of spin and energy between two molecules. However, in Dexter exchange coupling only energy transfer takes place between electrons of the same spin (see Figure 2.2A).[110,113] The triplet-triplet annihilation (TTA) is also related to Dexter-type energy transfer, where two triplet molecules exchange energy and spin to form a singlet.

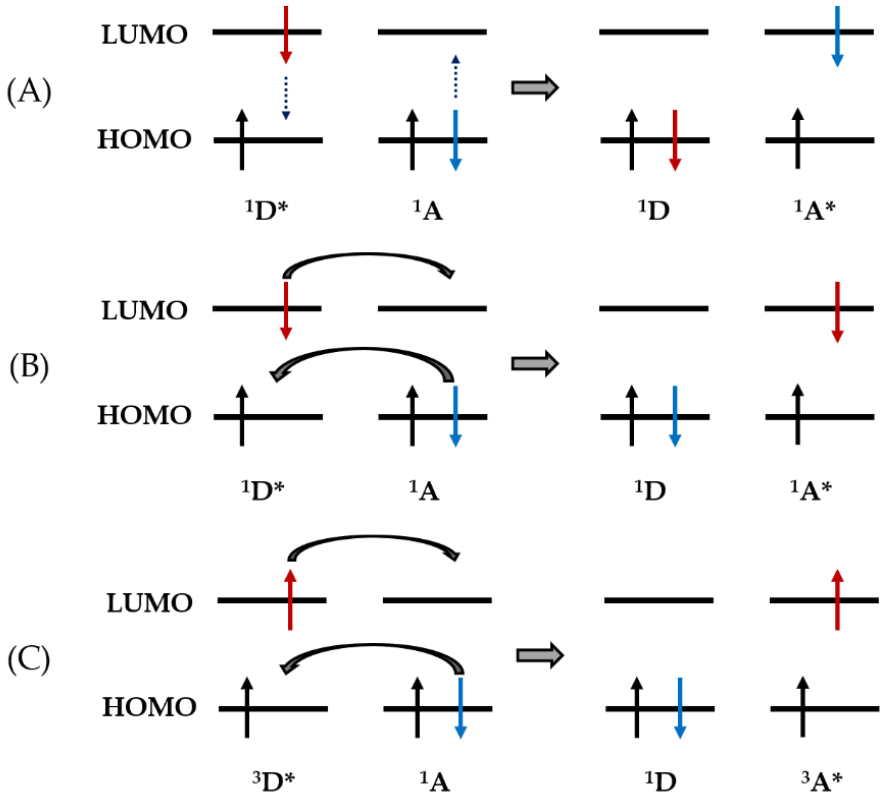

Figure 2.2: Schematics of energy transfer. (A) singlet-singlet Forster type energy transfer (B) singlet-singlet Dexter type energy transfer; HOMO- highest occupied molecular orbital, LUMO- lowest unoccupied molecular orbital, ^{1}D- singlet ground state donor molecule, ^{1}D*- singlet excited state donor molecule, ^{1}A- singlet ground state acceptor molecule, ^{1}A*- singlet excited state acceptor molecule, ^{3}D*- triplet excited state donor molecule, ^{3}A*- triplet excited state acceptor molecule.

In a system containing sensitizer and quencher, the rate of energy transfer from sensitizer to quencher is experimentally obtained using measurement of emission intensity of sensitizer with and without the presence of the quencher and fitting into the Stern-Volmer equation given in Equation 2.4:[10,59,114]

$$\frac{I_0}{I} = 1 + K\,[Q] = 1 + k_q \tau_0 [Q] \qquad \text{Equation 2.4}$$

Here, I and I_0 are the emission intensity of the sensitizer with and without the presence

of a quencher, K is the Stern-Volmer quenching constant, k_q is the rate of energy transfer from the sensitizer to quencher, τ_0 is the intrinsic lifetime of the sensitizer molecule under study and [Q] is the quencher concentration.

2.2 Steady State Spectroscopy

2.2.1 Steady-State Absorption Spectroscopy

The spectroscopic investigation of any molecule or sample begins with steady-state absorption measurement. This measurement gives the absorption spectra of the sample *i.e.* the band of wavelengths where the molecules absorb.

A sample is illuminated with a light beam, which gets absorbed by the sample and its molecules reach its excited state. A schematic diagram is illustrated in Figure 2.3 below:

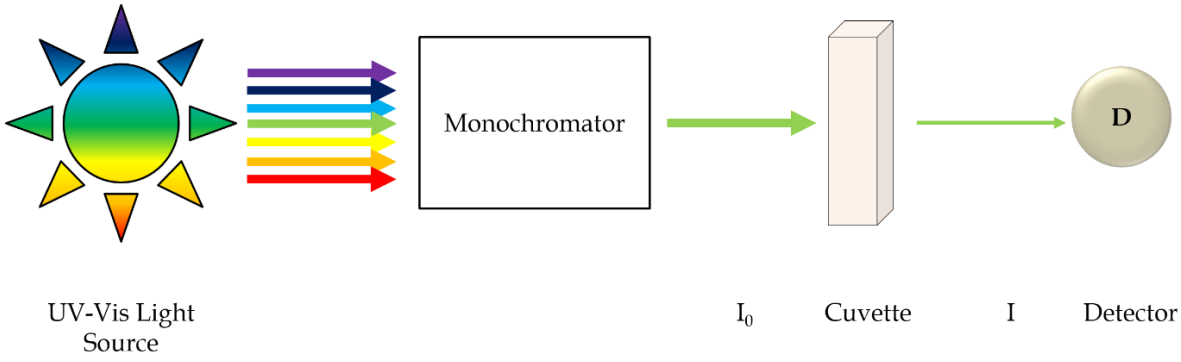

Figure 2.3: Schematic of UV-Vis absorption spectroscopy.

The light source is a UV-Visible light source, which can produce light of wavelengths from 200 nm to 900 nm. The monochromator is an optical device that separates a narrow wavelength of light from a wide range of wavelengths coming from a light source like the sun or white light source. The cuvette is a sample container made of glass, plastic or quartz, since the glass and plastic absorb the UV light, quartz made cuvettes have been used for all standard experiments in this thesis. The I_0 is the intensity of the light falling on the sample (inside the cuvette) and I is the intensity of the transmitted light which is detected by the detector. The relationship between the absorbance $A(\lambda)$, molar extinction coefficient of the sample $\varepsilon(\lambda)$, concentration (c) and path length (d) is given by Beer Lambert's Law described in Equation 2.5:[115,116]

$$A(\lambda) = log\left(\frac{I_0(\lambda)}{I(\lambda)}\right) = \varepsilon(\lambda) \cdot c \cdot d \qquad \text{Equation 2.5}$$

Where ε(λ) is a property of the molecule that indicates how intensely a molecule absorbs light of a particular wavelength, its unit is $L \cdot mol^{-1} \cdot cm^{-1}$. The concentration is denoted with c and the unit is $mol \cdot L^{-1}$. The path length of the cuvette or the length of the light path is denoted with l and its unit is cm.

The measurement of the UV-vis spectrum presented in this work was done with a JASCO V780 UV/VIS/NIR spectrophotometer, which has a double beam setup. In a double beam setup, cuvette with sample is placed in one path and cuvette with pure solvent is placed in another path and the measurements are performed simultaneously.

2.2.2 Steady-State Emission Spectroscopy

The steady-state emission is a measurement of long-term average fluorescence when excited with UV, visible or near-infrared (NIR) light. Using this technique, steady-state fluorescence spectra, excitation spectra, steady-state anisotropy and quenching experiments can be performed.[59]

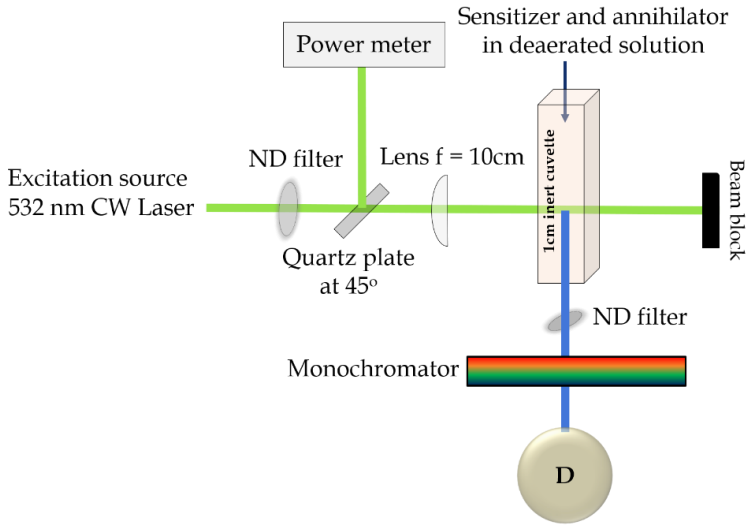

Figure 2.4: Schematic of the steady state upconversion emission measurement using a laser diode. ND: neutral density filter. D: detector. A planoconvex lens is used to increase the excitation power density at the focal point. The emission is measured in the perpendicular orientation to the excitation.

The steady-state emission measurement technique consists of a UV-visible-NIR excitation source, a monochromator to individually select an excitation wavelength, a sample holder to accommodate the cuvette, a monochromator again to individually select the fluorescence wavelength and a detector. In this work, a FLS980 emission spectrophotometer (Edinburgh Instruments) has been used to measure the emission

spectra, it has a xenon lamp as an excitation source (ozone free 450 W). The integrated emission intensity *vs.* excitation power density curves shown in Chapter 3 has been measured with this spectrophotometer by replacing the excitation source with a laser diode (CW532-100) of 100 mW from Roithner LaserTechnik GmbH, the schematic of the measurement system is shown in Figure 2.4.

2.3 Time-Resolved Spectroscopy

2.3.1 Transient Absorption Spectroscopy

Transient absorption spectroscopy is a pump-probe spectroscopy technique, where a sample is photo-excited by a light pulse (called pump pulse) to create thermodynamic nonequilibrium *i.e.* excites the sample to the excited state and a second light beam which can be continuous or pulsed called probe beam, follows the pump pulse to probe the excited state of the sample created by the pump pulse, the transmitted probe light from the sample is measured to observe the changes in the absorption as a function of wavelength and time.[117,118] This technique is used to measure the photogenerated excited states such as singlet and triplet excited states,[119] lifetimes of the states, intersystem crossing,[108,120,121] electron transfer,[122–124] energy transfer,[125] photoproduct kinetics.[126,127] It has found application in the investigation of photosynthesis,[128] photovoltaic conversion processes,[129,130] ultrafast processes in thin films,[131,132] photocatalysis and several other processes occurring at faster time scales.[119,133,134]

Transient absorption spectroscopy involves two kinds of instrumental setup based on the investigation of timescale, although both the instrumentations are based on the same principle and are called pump-probe spectroscopy. The ultrafast processes like formation of singlet excited state, geometrical relaxation, vibrational relaxation, solvent relaxation, singlet to triplet formation, electron transfer are investigated using excitation by femtosecond pulses hence called fs-TA.[128] Similarly, relatively slow processes like lifetime of the triplet states, bimolecular processes like triplet-triplet energy transfer and triplet-triplet annihilation, *etc*. are investigated using excitation by nanosecond pulses hence called ns-TA.[135,136]

The work presented in this thesis involves both fs-TA and ns-TA. First, instrumentation of fs-TA is described thereafter instrumentation of ns-TA is explained. The fs-TA consists a mode-locked titanium doped sapphire (Ti:Sa) as the fundamental laser, it produces pulses of wavelength of 800 nm, pulse duration 80 fs, repetition rate 1 kHz and energy 1 mJ. The output beam is split into two beams using

a beam splitter to generate suitable pump and probe beams. The pump wavelength is generated from the split beam either using a second harmonic generation crystal or an optical parametric oscillator (OPA, TOPASwhite, LightConversion Ltd.). Since the output wavelength of the fundamental laser is 800 nm, the second harmonic generation through barium borate (BBO) crystal provides 400 nm as pump wavelength;[137] whereas the OPA can generate a very broad wavelength, the OPA used for the experiments given in the thesis could generate wavelength ranging from 370 nm to 760 nm.

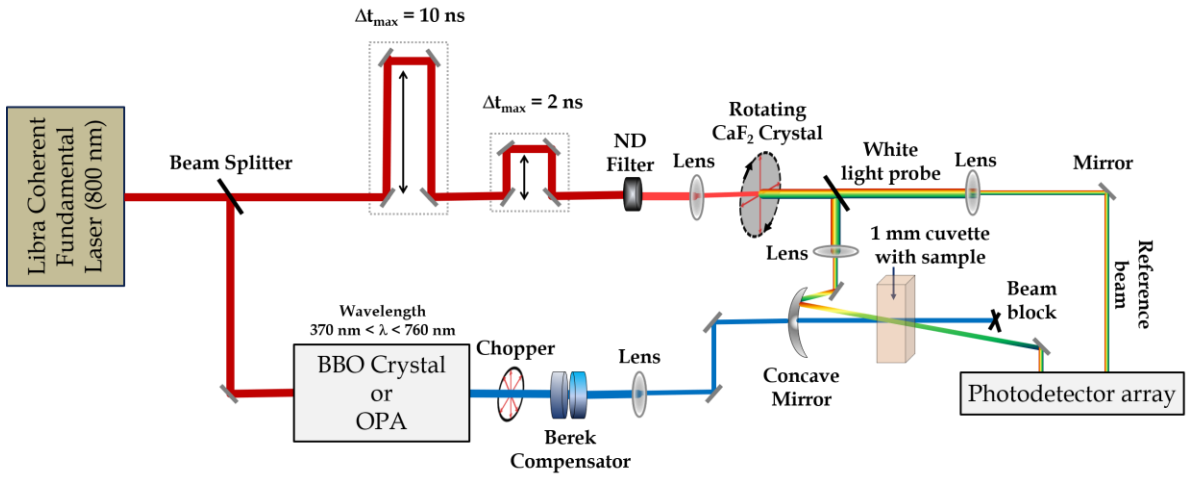

Figure 2.5: Schematic of the femtosecond transient absorption spectroscopy setup. Δt: is the delay time of the optical delay line. ND Filter: neutral density filter.

The pump pulse energy is at least an order of magnitude higher than the probe pulse. The pump pulse excites the sample to its electronic excited states. The second split beam from the fundamental laser is used as a probe beam. For single wavelength kinetics measurements, a single wavelength of choice needed to investigate the kinetic process is selected as the probe beam. The probe beam traverses through two delay lines of 2 ns time window and 10 ns time window, of which only one is used at a time. The delay line provides the time delay between the pump and probe light pulses. In case of a white light probe, the probe part of the fundamental beam is focused on a calcium fluoride (CaF_2) plate to generate a supercontinuum[138,139] (*white light*) after traversing through two delay lines. The probe light intensity is controlled using an attenuator and focused on to the CaF_2 plate using a lens to control the intensity and quality of the supercontinuum. The CaF_2 plate rotates in a non-circular path to avoid degradation by light intensity. A fraction of the probe beam before falling on the sample is recorded as a reference beam (I_{ref}). The relative polarization between the pump and probe polarization is kept at a magic angle (54.7°) to avoid signal contribution from rotational diffusion. A Berek compensator in the path of the pump

beam can realize the pump polarization at magic angle with respect to the probe polarization as well as controls the pump intensity. The pump and probe beams are spatially and temporally overlapped on the sample plane, which is placed in a 1 mm cuvette. The spatial overlap of the pump and probe beams is realized in a non-collinear fashion to separate and block the pump beam after the sample excitation; whereas, the reference and transmitted probe beam from the sample are sent to the detector.

A chopper is placed in the pump path before the sample position to chop the repetition rate to half of the fundamental laser source, while the probe beam has the repetition rate of the fundamental laser source. The chopper blocks every second pump pulse; hence, providing one pump pulse per two probe pulses. The detector measures two consecutive probe pulses transmitting from sample (i) after the pump excitation – I_p (ii) without the pump excitation – I_{np}. The measurement by the detector when both the pump and probe are blocked is denoted with I_{off}, it is subtracted from the measured spectra to remove the signal contribution stemming from the ambient light and electronic noise. A signal is recorded when only pump is on, probe and reference remain off, this signal is accounted for the emission from signal and noise and denoted as I_{pf}.

The differential absorption signal $\Delta A(\lambda,\Delta t)$ which is dependent on the wavelength and delay time can be written in terms of the equation as given below in Equation 2.6:[140]

$$\Delta A(\lambda,\Delta t) = log\left(\frac{I_{ref}(\lambda,\Delta t) - I_{off}(\lambda)}{I_p(\lambda,\Delta t) - I_{pf}(\lambda)}\right)\cdot\left(\frac{I_{ref}(\lambda,\Delta t) - I_{off}(\lambda)}{I_{np}(\lambda,\Delta t) - I_{off}(\lambda)}\right) \qquad \text{Equation 2.6}$$

The differential absorption signal $\Delta A(\lambda,\Delta t)$ can also be written in terms of the sum of molar extinction coefficient $\varepsilon_j(\lambda)$ and time-dependent molar concentration $c_j(\Delta t)$, where j is the number of transient species weighted by their time-dependent molar concentration. It is a straightforward representation of the Beer-Lambert law (given in Equation 2.5) in matrix notation, given in the Equation 2.7 below:[118]

$$\Delta A(\lambda,\Delta t) = \sum_j \varepsilon_j(\lambda)\cdot c_j(\Delta t)\cdot d \qquad \text{Equation 2.7}$$

The differential absorption signal $\Delta A(\lambda,\Delta t)$ dataset can be modeled as a function of delay time t and probe wavelength λ. The model can be described as a function, given in the Equation 2.8 below:[118]

$$\Delta A(\lambda, \Delta t) = \text{IRF} \otimes \sum_{j} A_j(\lambda) \cdot e^{\frac{-t}{\tau_j}} \qquad \text{Equation 2.8}$$

Where $A_j(\lambda)$ is the preexponential coefficient also known as decay associated spectra (DAS) associated with each probe wavelength; characteristic time constant (τ_j) associated with each exponential decay, j is the number of species varied to find the best fit. This model is also known as global analysis.[141] The quality of the fit is judged by the residual obtained from the fitting procedure. The data in the range of -250 fs to +250 fs are neglected in the analysis because of the contribution from coherent artifact signals due to the interaction of two short laser pulses in a polarized medium.[142] Due to the ignored region of artifact, the deconvolution with impulse response function (IRF) is neglected in data analysis, because the IRF is smaller than the ignored region.

The differential absorption signal (ΔA) for a specific λ and at a delay time Δt is calculated by the difference between the absorption signal of the sample in presence of pump and the absorption signal in absence of pump.[128] The ΔA signal can be positive or negative based on the contribution from the processes described below[128,140,143]:

Ground state bleach (GSB): The pump pulse excites the molecules to the excites state, hence the number of molecules present in the ground state decreases. Consequently, the absorption of the probe photons in the excited sample is less than the sample in the ground state (*i.e.* without excitation). This results in a (-) negative contribution to the ΔA signal. The GSB occurs in the steady state absorption region of the molecule, hence appear similar to inverted absorption spectra.

Stimulated emission (SE): The pump pulse excites the molecules to the excites state, these excited molecules interact with the incoming probe photons and induce emission in the same direction to the probe photons[144] and reach to the detector. It results in the detection of more photons at the detector with respect to no stimulated emission, consequently, resulting in a (-) negative contribution to the ΔA signal. The SE occurs in the emission region of the excited molecule, hence appears similar to the inverted emission spectrum. When the Stokes shift is small, the GSB and SE overlaps and appear as one band.

Excited state absorption (ESA): The pump pulse excites the molecules to the excited state, however, if any further higher excited states exist and the energy level matches with the wavelength of the incoming probe photons then the absorption of the probe photons by excited state molecules will occur. This results in fewer photons at the detector with respect to the sample in the ground state (*i.e.* without excitation);

consequently, appears (+) positive contribution in the ΔA signal.

Photoproduct absorption: The pump pulse excites the molecules to the excited state and if the molecules form a transient state such as a charge-transfer state or isomerized state, the absorption of probe photons by these transient states will lead fewer photons at the detector with respect to the sample without excitation; consequently, photoproduct absorption appears (+) positive contribution in the ΔA signal.

The ΔA signal of a sample can contain an overlap of two or more bands from GSB, ES, ESA and photoproduct absorption, it may depend on the absorption and emission bands of the constituent of a sample.

The nanosecond transient absorption spectroscopy (ns-TA) also works on the same principle as described above, however, its instrumentation varies significantly from the fs-TA, especially the pump pulse laser. It consists a fundamental Nd:YAG laser, which generates 5 ns pulses at a repetition rate of 10 Hz. The fundamental laser pumps an OPO to generate the excitation pump wavelength in the 410-800 nm range. The white light probe is generated using a 75 W xenon arc lamp. The probe beam is detected using a five-stage R928 Hamamatsu photomultiplier tube (PMT) placed at the exit slit of a monochromator.[10,145] The electronics of the detection system and software programs to control the hardware for fs-TA, ns-TA, and TAA (*vide infra*) have been developed by Pascher instruments (Lund, Sweden).

2.3.2 Transient Absorption Anisotropy

In a transient absorption spectroscopy measurement, the relative polarization between pump and probe polarization is kept at magic angle (54.7°) to avoid contribution from the depolarization of the transition dipoles of the molecules.[128] However, the anisotropy measurement is performed to measure the depolarization time of the dipoles; the relative polarization between pump and probe is either 45° or probe is split in two beams and polarization of the two split beams are set to 0° and 90° relative to the pump polarization. The transient absorption anisotropy (TAA) setup shown in Figure 2.6 was developed to investigate the objective 2 of this thesis.

In the setup shown here, probe beam is split into two beams and polarization is set accordingly. This setup is used to measure the rotational relaxation times of molecules described in Chapter 4.

While all other specifications of the instruments and devices used in the transient absorption anisotropy (TAA) setup remain the same as described in fs-TA setup, the

TAA involves a short delay line in the path of one the split probe to make both the probe paths exactly equal in length, as shown in Figure 2.6.

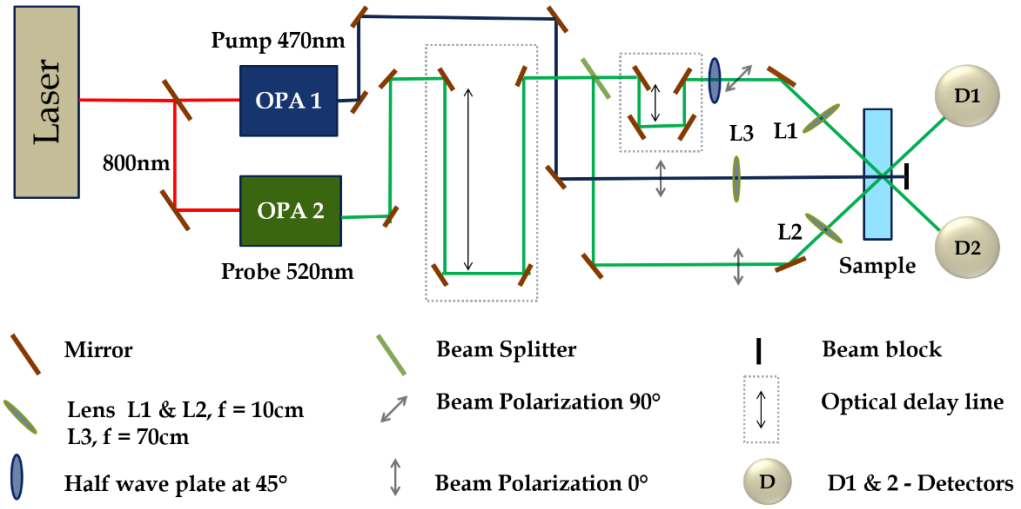

Figure 2.6: Schematic of the transient absorption anisotropy setup.

The TAA has a significant advantage over the time-resolved emission anisotropy (TEA) because the instrument response function of TEA[58] is in order of 100 ps whereas the instrument response function of TAA is in order of 100 fs.[146,147] As well as the electronics detection system of the TEA is not fast enough to detect the sub-picosecond timescales. Hence the transient absorption anisotropy is used which can resolve the sub-picosecond timescale since it involves an ultrafast laser pulse (80 fs) for the excitation and the step size of the delay time is determined by the step movement of the optical delay line. However, with the recent development of electronics and instrumentation of the time-resolved emission setup, timescales of several femtoseconds can be measured.[148,149]

2.3.3 Time-Resolved Emission Methods

Time-resolved emission spectroscopy provides the lifetime of the electronic excited state. This measurement is performed to determine the lifetime of the excited states and energy transfer process and to obtain the Stern-Volmer plot as described in Chapter 1. In this thesis work, two kinds of setups have been used to obtain the time-resolved emission measurement.

The time-resolved emission of the upconversion processes is measured using the ns-TA setup described (*vide supra*). The white light probe beam is blocked and the sample is excited with the 5 ns pulse laser and the emission is detected using the photomultiplier tube.

The time-resolved emission of the BODIPY molecules described in Chapter 4 is measured using a time-correlated single photon counting (TCSPC) setup with a fluorescence lifetime spectrometer (FluoTime 200, PicoQuant). An LED with an excitation wavelength 459 nm, 1 ns pulse width and a repetition rate of 10 MHz was used as the excitation source. A Glan-Taylor prism was used to select the polarization of the excitation and emission. The emission was recorded at 515 nm wavelength. The G-factor (= 1.34) which describes the polarization sensitivity of the detector was calculated using fluorescence decay of the Rhodamine 110 solution.

The time-resolved emission data is analyzed using the exponential decay of the emission intensity fitted with the equation below:

$$I\,(t) = I_0 \cdot e^{\frac{-t}{\tau_j}} \qquad \text{Equation 2.9}$$

The I_0 is the emission intensity at time zero and τ_j is the fluorescence lifetime of the molecule. In case of more than one decay component, the time constants can be the fluorescence lifetime along with the aggregation induced emission components

2.4 Microscopy Methods

The confocal fluorescence images of giant unilamellar vesicle (GUVs) presented in Chapters 4 & 5 were collected using a Leica TSP inverted (DMi8) confocal microscope, a 40x oil immersion objective was used. A white light LED with a monochromator to select 500-550 nm wavelength was used as an excitation source. The emission was collected in the spectral range of 510-570 nm without a polarizer. The GUVs were incubated in 0.1% agarose solution for 10 minutes before imaging to keep the vesicles immobile. The unpolarized emission images of GUVs in Chapter 4 and steady-state upconversion emission from LUV samples in Chapter 5 were acquired by Ms. Amrutha Prabhakaran in the laboratory of Prof. Tia Keyes, Dublin City University, Dublin, Ireland.

The polarization resolved confocal microscopy and fluorescence lifetime imaging of GUV shown in Chapter 4 were recorded using a confocal STED microscope (ExpertLine, Abberior Instruments, Göttingen, Germany). A linearly polarized pulsed picosecond laser of repetition rate 40 MHz at 488 nm was used as the excitation source. A 60x water immersion objective UPLSAPO60XW (NA = 1.2) from Olympus (Shinjuku, Japan) was employed as the objective lens. The fluorescence emission was measured in the range of 505-550 nm and split by a polarizing beam splitter cube to

record simultaneously by two single photon counting avalanche photodiodes (SPCM-AQRH-14-TR, Excelitas, Mississauga, Canada) using synchronized TCSPC electronics comprising four-synchronized SPC-150N cards with routers (Becker & Hickl, Berlin, Germany). The confocal anisotropy image analysis was performed by correcting the detector sensitivity and accounting for background intensity. The depolarization factor of the microscope objective was accounted for the calculation of the anisotropy of each pixel. The polarization resolved confocal microscopy and time-resolved emission anisotropy measurements were performed in the Single Molecule Microscopy laboratory of Prof Michael Börsch, Friedrich Schiller University, Jena.

2.5 Synthesis of Lipid Bilayer Vesicles

The giant unilamellar vesicles (GUVs) used for anisotropy measurements in Chapter 4 were prepared using 1,2-Dioleoyl-sn-glycero-3-phosphocholine (DOPC) lipid of 5 mM and 15 μM of the dye (BODIPY-Ar-Chol) in chloroform solution. The solution mixture of DOPC and dye was drop cast on a pair of indium tin oxide (ITO)-coated glass slides and kept in the desiccator and vacuum was applied to evaporate the chloroform. The dried ITO slides were inserted into the Vesicle Prep Pro (Nanion Technologies) and a greased O-ring was applied on the conductive side of one slide. Two slides were kept in the fashion to completely seal the 230 mM sucrose filled lipid drop casted area with conductive sides facing each other. The electroformation was started with a rising voltage ramp-waveform 0-3 V within 5 minutes, then 3 V was kept steady for 170 minutes at 10 Hz frequency, then a decaying ramp-waveform 3-0 V in 5 minutes was applied to finish the electroformation. The GUVs were collected and stored in an Eppendorf tube. The entire process of electroformation was carried out at 37°C which is maintained by the Nanion device.[63] The GUVs were placed in 1 mm pathlength cuvettes for femtosecond transient absorption anisotropy measurement.

The large unilamellar vesicles (LUVs) used for upconversion measurements in Chapter 5 were prepared by the hydration extrusion method. A sample mixture of lipid (DOPC), annihilator and sensitizer were prepared in the molar ratio 5088:10:1 respectively in chloroform solution. The mixture was placed in a 1.5 mL glass vial and the solvent was evaporated by nitrogen flow, followed by evaporation under vacuum conditions in a desiccator for 60 minutes. The dried film of the mixture on the glass vial was rehydrated with 1 mL phosphate buffer saline (PBS) at pH 7.4 and the film was suspended into the PBS by vortexing for 60 s. The solution mixture was extruded

through a polycarbonate membrane of 100 nm by eleven times to produce uniform LUVs of 100 nm sizes. To perform the TTAUC measurements on LUVs samples, sodium sulfite (Na_2SO_3) has been used as an oxygen scavenger.

The GUVs and LUVs used for experiments in Chapter 4 and Chapter 5 were synthesized by Amrutha Prabhakaran from the group of Prof. Tia Keyes, Dublin City University, Ireland.

2.6 Computational Methods

The computational simulations were performed to calculate the dihedral angles, orientation of the transition dipole moment (TDM), potential energy surface (PES) and Löwner-John ellipsoid in Chapter 4; energy levels and spin-orbit coupling in Chapter 5. The simulation work to calculate TDM, PES and spin-orbit coupling was carried out by Mr. Rengel Cane Sia and Dr. Julien Guthmuller from Gdańsk University of Technology, Gdańsk, Poland. The simulation work to calculate the Löwner-John ellipsoid was performed by Dr. Martin Presselt and Ms. Anna Elmanova from Friedrich Schiller University, Jena.

This thesis work is based on experimental spectroscopic investigation; however, due to the strong interdependence between simulation and experimental results presented in Chapters 4 and 5, a brief outline of the simulation methodology is described here.

The Gaussian 16 and Orca 5.0 program was used to conduct the quantum chemistry computations.[150,151] The shape of the ground state (S_0) was calculated using density functional theory (DFT), while the singlet excited state (S_1) characteristics, namely energy, S_0-S_1 transition dipole moment (TDM), geometry, triplet excited states properties (*i.e.* transition dipole moment, vibrational frequencies) and geometry was computed using time-dependent DFT (TDDFT). The DFT and TDDFT computations were carried out using the MN15[152] exchange-correlation (XC) functional and the def2-SVP basis set.[153,154] The GD3 model was used to include density functional dispersion adjustments for MN15,[155,156] using the value described by Goerigk *et a*l.[156] The polarizable continuum model (PCM)[157] was used in the SMD solvation model to account for the effects of the solvent (ε_{DCM} = 8.93, $\varepsilon_{Dioxane}$ = 2.2099).[158] By comparing non-equilibrium and equilibrium PCM computations, the impacts of solvent reorganization on the TDM were determined.

The TDM coordinates (X, Y, Z) were determined with respect to a Cartesian frame fixed within the molecule. The X-axis of the frame links the center carbon atom and

the boron atom of the BODIPY core. The Y axis goes through a carbon atom of the center BODIPY ring, defining the BODIPY's long axis. The Z axis is perpendicular to the XY plane. This Cartesian frame is used to compute all TDMs values. As a result, the computed rotation angles characterizing a TDM rotation within the molecule-fixed frame.

The Orca was used to calculate the scalar relativistic TDDFT computations using the Douglas-Kroll-Hess (DKH) technique to determine the spin-orbit coupling (SOC) between the singlet state S_1 and the triplet states T_1, T_2, and T_3. These computations were carried out using optimized S_0 and S_1 geometry. The XC functional MN15 was used in conjunction with the basis sets DKH-def2-TZVP (for atoms H, C, N, B, F) and SARC-DKH-TZVP (for atom I) as well as the supplementary basis set SARC/J. CPCM used the SMD solvation model to account for the effects of the solvent (1,4-dioxane).

The Löwner-John ellipsoid shown in Chapter 5 was calculated using the iterative procedure to find the smallest ellipsoid touching the Van-der Waals surface of the sensor molecule.[159–161] The task of determining the minimum Löwner ellipsoid for a given set of points, which may also be interpreted as a convex polytope, is equivalent to identifying the minimum volume of an ellipsoid that fully encloses the polytope. The Minimum Volume Ellipsoid (MVE) problem is a widely recognized issue in the fields of convex geometry and optimization.[162] Various algorithms exist for resolving the MVE problem, which commonly entails iterative methodologies that ultimately converge toward the solution. The Ellipsoid Method is a well-known algorithm, it was first presented by Shor in 1987.[163] The Ellipsoid Method commences by selecting an initial ellipsoid that encompasses the convex polytope. Subsequently, the method proceeds to enhance the ellipsoid iteratively by reducing its size along its longest axis until it attains the minimum size that encloses the polytope.[164] During each iteration, the algorithm calculates a linear approximation of the polytope by utilizing the present ellipsoid and subsequently identifies the facet of this approximation that is in closest proximity to the origin. The utilization of the supporting hyperplane pertaining to this facet serves to establish a novel ellipsoid that is comparatively smaller in size and encompasses the polytope. The iterative procedure is executed by the algorithm until the ellipsoid attains convergence to the minimum achievable volume. In the current scenario, an iterative approach was employed to compute the minimum ellipsoid that could potentially accommodate the given set of points.

2.7 Synthesis of Molecules

The molecules investigated in the thesis have been obtained from various collaborators, the details of the synthesis can be found in the respective publications mentioned in the references. The group of Prof. Tia Keyes, Dublin City University, Ireland synthesized and provided the following molecules (i) the ester-decorated $[Ru(2,6\text{-di(quinolin-8-yl)pyridine})_2]^{2+}$ used as monomeric sensitizer in Chapter 3;[10] (ii) the BODIPY-Ar-Chol molecule used for the investigation of anisotropy[63] in Chapter 4 and (iii) the BODIPY-perylene dyad molecules used for the upconversion experiments in Chapter 5.[165] The poly(methyl methacrylate) bound $[Ru(dqp)_2]^{2+}$ molecules used as polymeric sensitizer in Chapter 3 was synthesized[10] and provided by the group of Dr. Michael Jäger, Institute of Organic Chemistry and Macromolecular Chemistry, Friedrich Schiller University Jena, Germany.

3. Triplet-Triplet Annihilation Upconversion by Polymeric Sensitizer

3.1 The Objective and the Approach

In this chapter, objective 1 has been investigated using steady-state and time-resolved spectroscopy. First, the selection of sensitizer and annihilator molecules is discussed; followed by steady state, time-resolved measurements and results are presented and discussed.

To investigate the TTAUC system, where the sensitizer molecules are linked to a macromolecule, ester-decorated $[Ru(dqp)_2]^{2+}$ complex has been chosen as a monomeric triplet sensitizer (**MS**), where dqp is 2,6-di(quinolin-8-yl)pyridine; and 9,10-diphenylanthracene as annihilator. Both molecules have been investigated for their potential to participate in triplet-triplet energy transfer (TTET).[27,75] For instance, Boutin *et al*. demonstrated TTAUC in polymer-linked $[Ru(2,2\text{-bipyridine})_3]^{2+}$ sensitizer and 9,10-diphenylanthracene (DPA) as an annihilator.[27] Several other combinations of ruthenium-based sensitizers and DPA have been reported as sensitizer and annihilator pair respectively.[67,70,166,167]

The $[Ru(dqp)_2]^{2+}$ complex has a longer triplet lifetime with respect to bpy-based congeners.[168] The suitability of the **MS** with DPA for TTET has already been identified.[68,169,170] The $[Ru(dqp)_2]^{2+}$ complex units linked to poly(methyl methacrylate) (PMMA) backbone[171] is referred as Ru-PMMA. It has been used as a polymeric triplet sensitizer (**PS**) with DPA as an annihilator in the TTAUC system.

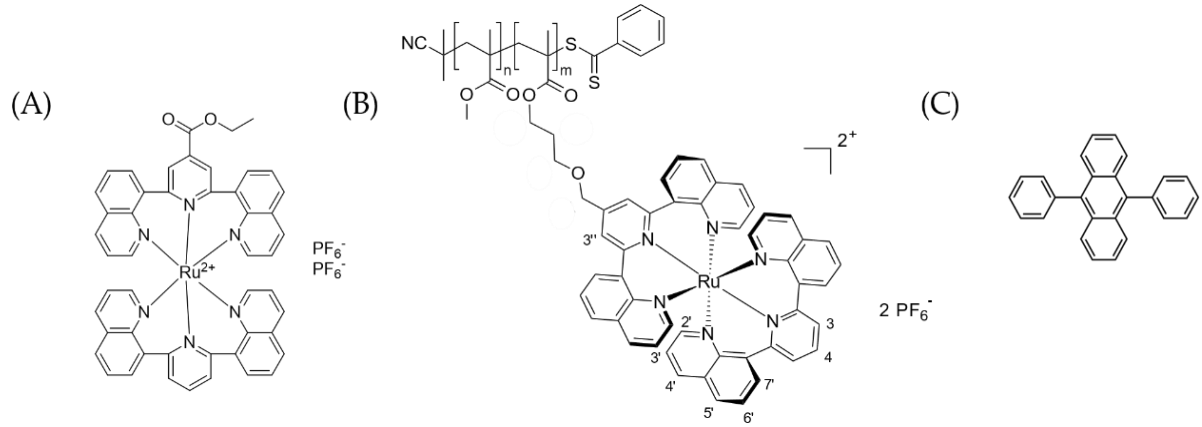

Figure 3.1: Molecular structure of (A) **MS** (B) **PS** (C) DPA

Based on the MMA conversion rate (79%) and the original MMA/monomer ratio

(95/5), a typical **PS** chain should comprise 75 MMA units and 4 Ru centers. The nuclear magnetic resonance integration of sample protons yields a relative content of Ru units vs MMA units of 6%, which is consistent with the observed seamless conversion and feed ratio of polymerization. The details of the synthesis of molecules have not been included in the thesis but can be found in the supporting information of the manuscript published.[10] In essence, multiple Ru centers can be reasonably presumed to be incorporated in a sample polymer (PMMA) chain. The molecular structure of **MS**, **PS** and DPA are given in Figure 3.1.

3.2 Samples and Terminology

All experiments were carried out in deaerated acetonitrile (ACN). The deaeration of the ACN is performed through freeze pump thaw. All steady-state and time-resolved measurements are performed using 1-centimeter Schlenk-cuvettes in order to maintain the inert conditions. The sensitizer concentration is held fixed at 5 μM and three annihilator concentrations of 10 μM, 50 μM, and 250 μM are used for upconversion and energy transfer measurements.

Table 3.1: Terminology and the concentration of the samples under investigation.

Samples	Sensitizer concentration (μM)	Annihilator concentration (μM)	Terminology
MS and DPA	5	10	**M-10**
	5	50	**M-50**
	5	250	**M-250**
PS and DPA	5	10	**P-10**
	5	50	**P-50**
	5	250	**P-250**

Throughout the text, the following terminology is used: when monomeric sensitizer (**MS**) of 10 μM concentration is mixed with 20 μM of DPA in deaerated acetonitrile, a sample containing 5 μM of **MS** and 10 μM of DPA is formed, which is referred as **M-10**; similarly, **PS** of 10 μM concentration is mixed with 20 μM of DPA results in 5 μM of **PS** and 10 μM of DPA, it is referred as **P-10**. All other samples were prepared with

different concentrations of DPA while keeping sensitizer concentration constant, see Table 3.1 for details. The concentration of **PS** refers to the concentration of Ruthenium-units linked to polymer chains in the sample.

The steady-state and time-resolved experiments are performed using the setup described in Chapter 2. The excitation wavelength was 532 nm for all the experiments reported here. A 532 nm notch filter (Edmund optics) is used to block the pump from entering to the detector. The energy of the pump pulse is maintained at 0.10±0.01 mJ. The lifetime of the sensitizer and annihilator molecules are obtained by the global analysis of the nanosecond transient absorption (ns-TA) spectra using Origin 2019. The decay associated spectra (DAS) obtained from the global fitting were used to assign the lifetimes. The best fit was selected by the investigation of the residuals from fit and minimum reduced chi-square (reduced-χ^2) value. An integrated sphere method was used to calculate the absolute quantum yield (Φ) of the emission of **MS**. Quantum yield of **PS** and upconversion yield has been obtained relative to the quantum yield of **MS**. The maximum theoretical efficiency of the upconversion emission quantum yield is 50%.[72]

3.3 Steady State Absorption and Emission Spectroscopy

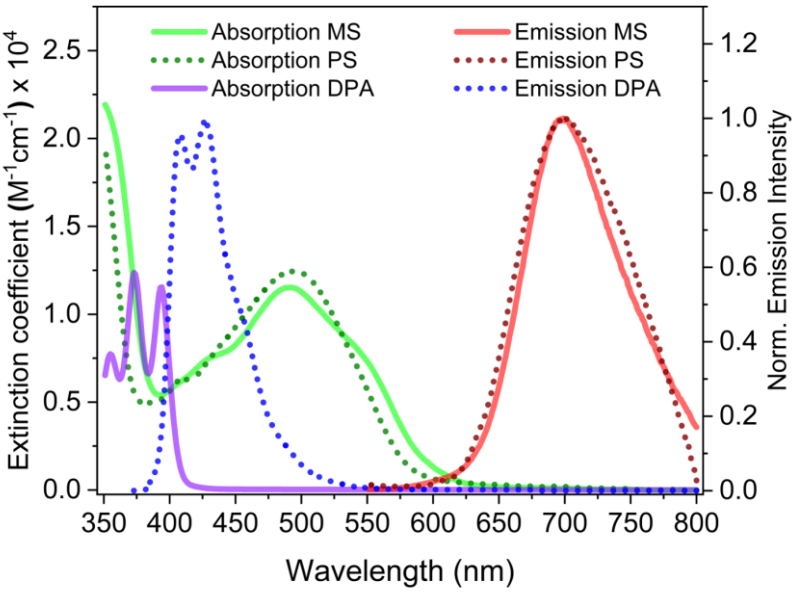

Figure 3.2: Absorption and emission spectra of **MS**, **PS** and DPA, excitation wavelength is 532 nm for MS and PS, 355 nm for DPA

The absorption and emission spectra of **MS**, **PS** and DPA are shown in Figure 3.2. The

absorption spectra of **MS** match with the absorption spectra of a [Ru(dqp)2]$^{2+}$-type complex as reported in the literature.[27,68,172,173] The **PS**'s chromophore concentration is selected so that the absorbance at 532 nm is the same for **MS** and **PS**. Although, the absorption spectra of **MS** and **PS** are very similar; there is a small change in the absorption spectra of **PS** near 450 and 550 nm in comparison to **MS**. The bathochromic shift has been previously reported and can be ascribed to the electron-withdrawing nature of ester group versus the slightly electron-donating nature of the alkyl group.[68]

The emission bands of **MS** and **PS** in the 600-800 nm region are nearly indistinguishable and resemble the form of the ^{3}MLCT phosphorescence of [Ru(dqp)2]$^{2+}$-type compounds.[174,175] The absorption of DPA lies between 350 and 415 nm. It emits light in wavelengths ranging from 375 to 525 nm (see Figure 3.2). Triplet-triplet annihilation upconversion (TTAUC) is evident in all six samples, previously mentioned (**M-10** to **P-250**): the samples are excited at 532 nm, the usual DPA fluorescence at wavelengths below 500 nm is visible (Figure 3.3).[9,176]

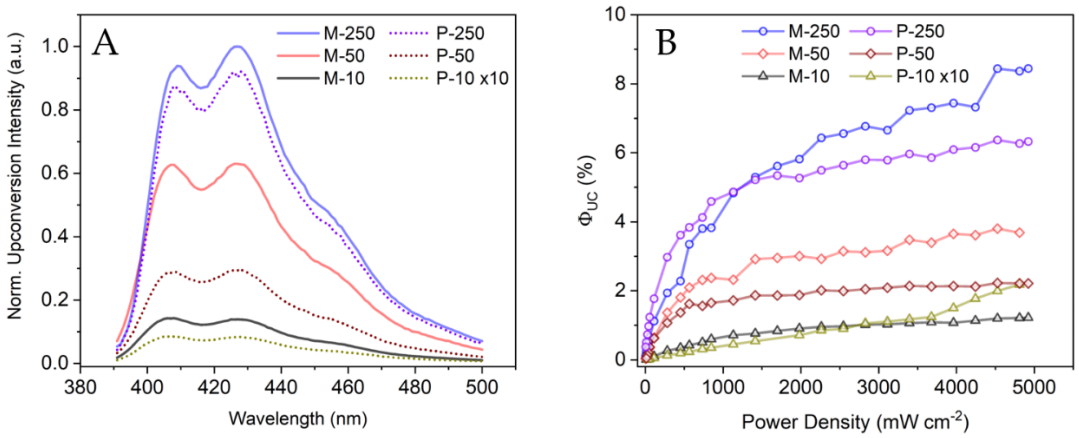

Figure 3.3: (A) Upconversion emission from **M-10**, **M-50**, **M-250**, **P-10**, **P-50** and **P-250**; all upconversion emissions are measured at an excitation density of 850 mW cm^{-2} and are normalized at the emission maximum of **M-250** at 427 nm. (B) Power density *vs.* upconversion quantum yield, Φ_{MS}= 3.6%, Φ_{PS}= 0.7%.

The effect of increasing the DPA concentration on upconversion is visible in Figure 3.3A; the peaks at 405 and 427 nm are rising with the increase of DPA concentration. The integrated area under the upconverted emission bands for **M-10**, **M-50**, and **M-250** are 8.2, 36.3, and 54.8 respectively; similarly, 0.5, 16.9 and 50.3 for **P-10**, **P-50**, and **P-250** respectively. The rise in integrated upconversion emission intensity upon increasing the DPA concentration is steeper in **PS** containing samples.

3.3.1 Upconversion Quantum Yield

The **MS** has an absolute fluorescence quantum yield of 3.6% and **PS** has relative quantum yield of 0.7%. The absolute quantum yield of **MS** (3.6%) is used as the reference for all relative quantum yield measurements. The upconversion emission quantum yield (Figure 3.3B) for **M-10**, **M-50**, and **M-250** at excitation power densities of 1130 mWcm^{-2} are 0.7, 2.3, and 4.8%, respectively; while for **P-10**, **P-50**, and **P-250** are 0.1, 1.7, and 4.8% respectively. Similar to integrated upconversion intensity, the rise in upconversion quantum yield with increasing DPA concentration is steeper for **PS** containing samples than for **MS**. The highest upconversion quantum yield measured at 4900 mW cm^{-2} are 0.2%, 2.2%, and 6.3% for **P-10**, **P-50**, and **P-250** respectively; for **MS** containing samples **M-10**, **M-50** and **M-250** upconversion quantum yield are 1.2%, 3.7%, and 8.4% respectively.

3.3.2 Threshold Power Density (I_{th}) of Monomeric and Polymeric Upconversion Systems

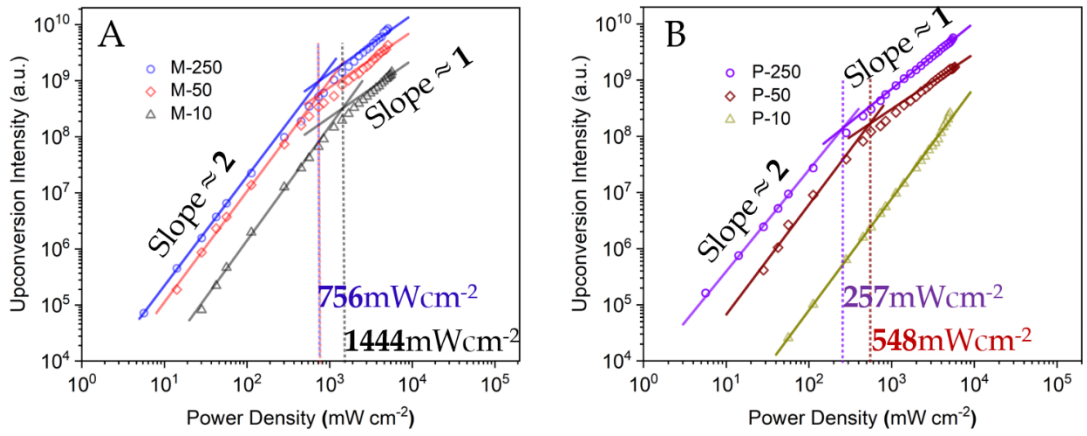

Figure 3.4: log (Power density) *vs*. log (Integrated upconversion emission intensity) for (A) **MS** and (B) **PS**; R^2(COD) ≈ 0.98 in all fitting case; for **P-250** weak annihilation regime slope is 1.8 and strong annihilation regime slope is 1.2 which is considered as 2 and 1 respectively in Figure B.

The upconversion intensity increases steeply as a function of excitation power density up to *ca*. 1000 mW cm^{-2}; either observed directly as integrated upconversion intensity (shown in Figure 3.4) or as reflected in the upconversion quantum yield (Figure 3.3 (B)). The sharp rise in integrated upconversion intensity is followed by a region with a significantly reduced slope at higher excitation power density (> 2000 mw cm^{-2}). This changeover in the slope indicates the change from the weak to strong annihilation

regime and is described as threshold power density (I_{th}) in the literature as well as in section 1.5.4.[89,177,178] The I_{th} value at which the upconversion system reaches its strong annihilation limit is 1444 mW cm^{-2} for **M-10** and 756 mW cm^{-2} for **M-50** and **M-250**. Thus, despite a rise in the absolute upconversion emission intensity, increasing the DPA concentration from **M-50** to **M-250** does not decrease the I_{th} any further. The I_{th} values for **P-50** and **P-250** are 548 mW cm^{-2} and 257 mW cm^{-2} respectively. There is no noticeable transition from a weak to a strong annihilation regime for **P-10**, indicating an inefficient upconversion system; whereas, the **P-250** is the most efficient system for upconversion based on the threshold power density. This finding is similar to what Sittig *et al*. found on a fully polymer-integrated upconversion system, where they also observed a linear relation between integrated upconversion intensity and low values of excitation power density.[33]

In general, increasing the annihilator concentration results in more collisional partners (annihilator molecules) in the proximity of an excited triplet sensitizer (^{3}S*). As a result, chances of the triplet-triplet energy transfer process (TTET) increase. However, exceeding a certain DPA concentration level can result in aggregate and excimer formation and consequently limiting the upconversion emission.[179–181] The ground state sensitizer molecules (^{1}S) have more photons available for absorption by increasing the excitation power density; in such cases more number of ^{3}S* is formed which participates in TTET to form ^{3}A*, ultimately a higher number ^{3}A* participates in efficient TTA and consequently increasing the upconversion emission intensity (see equation 1.12). However, beyond the I_{th} upconversion intensity varies linearly with increasing excitation power density and the quantum output appears to plateau and TTA (^{3}A*-^{3}A*) limits the upconversion rate, as described in section 1.5.4.[86,88,89,182,183]

The sensitizer units in the **PS** samples are covalently linked to the polymer chain, resulting in a non-homogeneous distribution of sensitizer molecules in the sample. The sensitizer (**PS**) content is high within the volume occupied by the polymer chain, whereas the sensitizer concentration is depleted in other regions of the sample. The impact of the non-uniform distribution of sensitizers on the upconverting mechanism can be observed through the following outcomes: (i) the TTAUC takes place solely in the proximity of the **PS**, specifically in the proximity of the polymer strands where **PS** is linked. As a result (ii) the ^{3}A* produced by TTET is spatially restricted to the region of the polymer strands. Consequently, the ^{3}A* molecule does not need to diffuse far to find a second ^{3}A* molecule for TTA; which leads to very effective TTAUC (strong annihilation) near the polymers, forming "upconversion hot spots".[8,184,185] In contrast, the distribution of sensitizers and annihilators in samples containing **MS** is

homogeneous. Consequently, upconversion occurs throughout the excitation focal volume. (iii) A significant proportion of the annihilator molecules (DPA), specifically those located in partial volumes devoid of the sensitizer molecule, does not participate in the upconversion process. The presence of a polymer backbone (PMMA), responsible for anchoring the sensitizer molecules, has the potential to impede the unrestricted diffusion of both sensitizer and DPA molecules. This hindrance may arise due to the obstruction or confinement of the diffusion pathway, leading to a potential impact on the TTET and collisional TTA processes, eventually limiting the upconversion emission.[186] (iv) Finally, the sensitizer compartmentalization in **PS** units reduces the upconversion photons by reabsorption from the first excited singlet state of DPA (^{1}A*) to **PS** (^{1}S).[170,187,188] In scenarios, where the excitation power density is low and a low number of sensitizer molecules are excited, the occurrence of back energy transfer from a localized excited singlet DPA (^{1}A*) to a non-excited **PS** (^{1}S) within the "upconversion hot spots" is higher, due to the presence of numerous sensitizer molecules in the ground state of the proximity to a given excited ^{1}A*. Reabsorption (back-energy transfer) may take place under conditions of high excitation power density; nevertheless, considering the low numbers of ground-state sensitizer molecules (^{1}S), it is improbable that the reabsorption process will prevail over the upconversion emission. The aforementioned factors indicate that changes to the excitation power density or DPA concentration have a more significant influence on samples containing **PS**.

The **P-10** upconversion system, as evident from the Figure 3.4B does not attain the strong annihilation regime. It exhibits two limitations: firstly, when the excitation power density is low, specifically in the weak annihilation regime, a considerable number of sensitizers that are not excited are present in proximity to an excited emissive singlet annihilator (^{1}A*). Consequently, a relatively significant proportion of the excited ^{1}A* engages in reabsorption, as mentioned in point (iv) above. At high excitation power densities, a considerable amount of triplet states (^{3}S*) is present, which can afford effective triplet-triplet annihilation upconversion (TTAUC); however, the likelihood of triplet-triplet energy transfer (TTET) is reduced due to the low number of DPA molecules that can serve as energy acceptors in the proximity of a specific excited **P-10** sensitizer. Therefore, the **P-10** sample fails to attain the strong annihilation regime.

3.4 Transient Absorption Spectroscopy of Upconversion Systems

The kinetics of the TTAUC process were investigated using nanosecond time-resolved spectroscopy (ns-TA). The data pertaining to ns-TA is depicted in Figure 3.5.

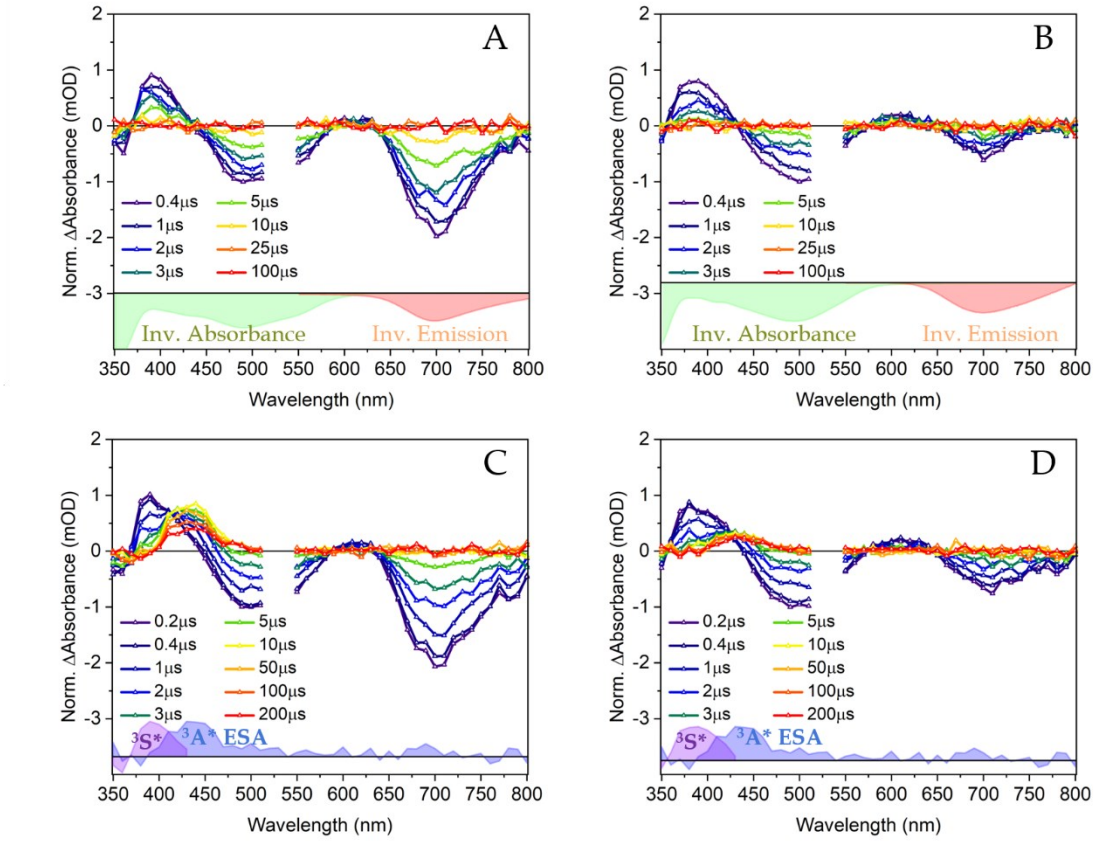

Figure 3.5: Normalized nanosecond transient absorption spectra of (A) **MS**, τ_{MS} = 4.5 µs (B) **PS**, τ_{PS} = 2.5 µs; spectra A and B normalized by peak of GSB at 500 nm (C) **M-50**, τ_{MS} = 2.4 µs, τ_{DPA} = 160 µs (D) **P-50**, τ_{PS} = 2.0 µs, τ_{DPA} = 210 µs. Bottom of A and B - inverted emission in red and inverted absorbance in green. Bottom of C and D - overlap of excited state absorption of ^{3}S* in violet and ^{3}A* in blue. τ represents the triplet lifetime of the individual species as indicated in the subscript.

The results depicted in Figure 3.5 shows the stimulated emission of **MS** centered at 700 nm, as well as ground-state bleach (GSB) centered at 500 nm and excited-state absorption (ESA) near 400 nm. The data were fitted using mono-exponential global fitting procedure, which yielded a decay time of 4.5 µs, it is attributed to the lifetime of the triplet state of **MS**. The spectra features (GSB, ESA and SE) and the triplet lifetime of the molecules are consistent with the earlier findings by Hammarström and coworkers.[68,189] The decay associated spectra of the **MS** are shown in the Figure 3.6A. The spectral features exhibited by **PS** (Figure 3.6B) are analogous to **MS**. Nevertheless, a mono-exponential global fitting procedure applied to the data yields a characteristic

lifetime value of 2.5 µs. Furthermore, it is observed that the incorporation of the sensitizer into the polymer matrix results in shorter triplet lifetime. Additionally, the relative intensities of the stimulated emission band at 700 nm are relatively less pronounced in **PS** sample compared to **MS**. In identical experimental conditions, the DPA of 50 µM revealed an excited state lifetime of 3.1 ms, which is consistent with literature reports.[96,190] The nanosecond transient absorption spectra and DAS are shown in Figure 3.7. The triplet state formation pathway in DPA sample is due to excitation at 410 nm followed by the intersystem crossing.

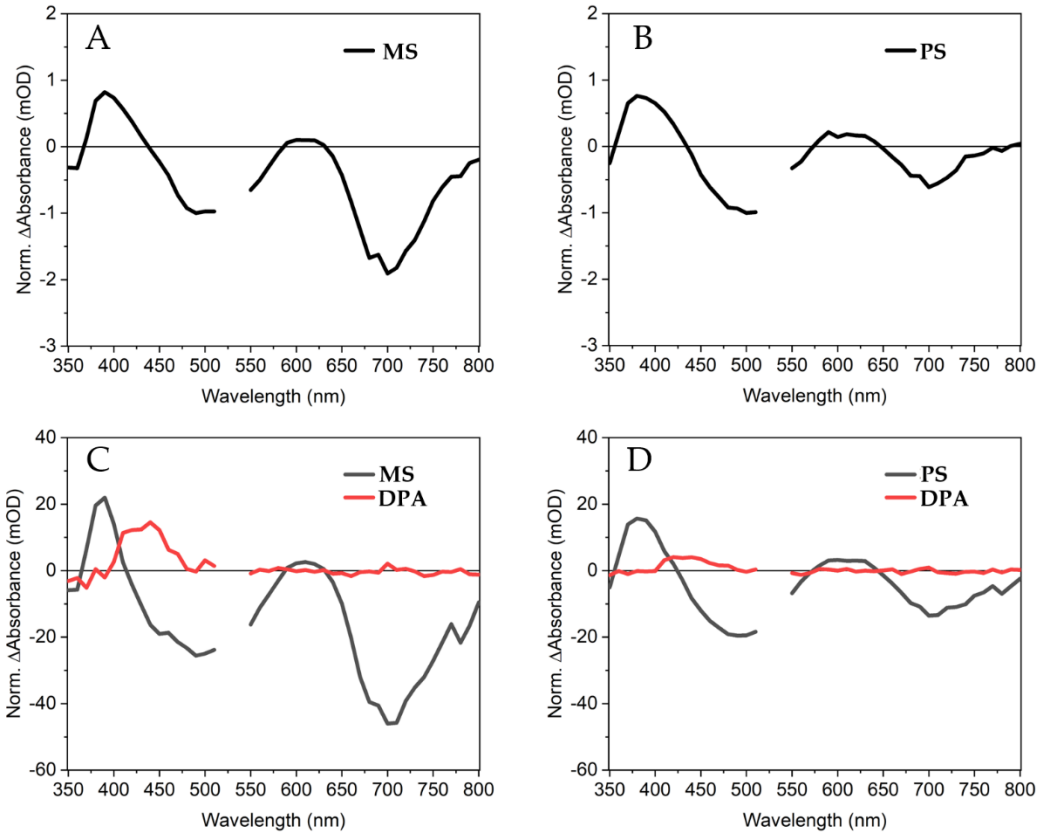

Figure 3.6: Normalized decay associated spectra (DAS) of (A) **MS**, (B) **PS**, (C) **M-50**, and (D) **P-50**.

Following the addition of annihilator into the sensitizer solutions, the differential absorption (ΔAbsorbance) characteristics of the sensitizer persist. However, an additional band associated with excited state absorption (ESA) of DPA at 425 nm becomes apparent, signifying the presence of the triplet state DPA (^{3}A*), see Figures 3.6C and 3.6D.[191] The presence of triplet DPA results in the shortening of the ^{3}S* lifetime of **MS** in M-50 to 2.4 µs as a consequence of TTET, the lifetime of ^{3}A* is 160 µs (Figure 3.5C). The spectra of **P-50** are shown in the Figure 3.5D and its DAS is shown in Figure 3.6D; the spectra features of **P-50** resemble to **M-50**. The appearance of the

additional band at 425 nm in **P-50** is also due to the formation of triplet DPA, triplet lifetimes of the sensitizer and annihilators are 2.0 μs and 210 μs, respectively.

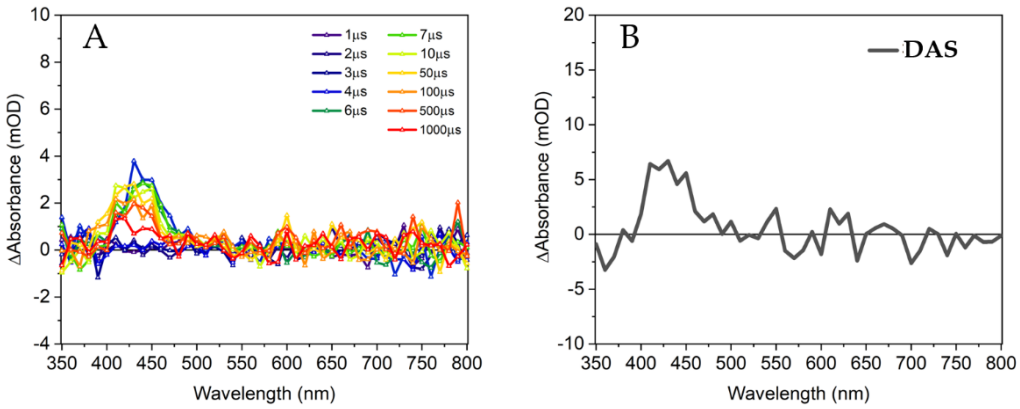

Figure 3.7: Nanosecond transient absorption spectra of 50 μM DPA in deaerated acetonitrile, excitation wavelength is 410 nm. (B) Corresponding decay associated spectrum (DAS).

The triplet state lifetime of the **PS** is shorter than the triplet state lifetime of the **MS**. The longer triplet lifetime of **MS** molecules will create more triplet annihilator ^{3}A* through TTET than **PS**, resulting in higher differential absorbance of ^{3}A* centered around 425 nm in **M-50** (Figure 3.5C) than **P-50** (Figure 3.5D); consequently, resulting in a higher number of TTA pairs and higher upconversion emission intensity. The lifetimes were determined using the global fitting (see, Equation 2.8 for details) and are tabulated in Table 3.2.

Table 3.2: Triplet lifetime of samples. The maximum error is within 10% of the given value. DPA sample is 50 μM, measured in deaerated acetonitrile.

	MS	**PS**	DPA	**M-10**	**M-50**	**M-250**	**P-10**	**P-50**	**P-250**
^{3}S* τ (μs)	4.5	2.5	-	3.8	2.4	0.9	2.4	2.0	1.0
^{3}A* τ (μs)	-	-	3100	340	160	120	>1000	210	190

Upon increasing the concentration of the annihilator in the monomeric sensitizer system, the lifetime of the ^{3}A* gets reduced from 340 μs to 120 μs. The upconversion systems that consist of polymeric sensitizers exhibit a greater influence by variation in annihilator concentration. The triplet lifetime of ^{3}A* in **P-10** is observed to exceed 1 ms. However, upon increasing the annihilator concentration to **P-250**, the triplet lifetime of ^{3}A* reduces to 190 μs. The observed phenomenon is attributed to the higher

localized concentration of $^3A^*$ in the localized "upconversion hot spots" in the vicinity of the polymer chains. This results in localized more efficient triplet-triplet annihilation (TTA) and consequently, shortening the lifetime of the $^3A^*$.

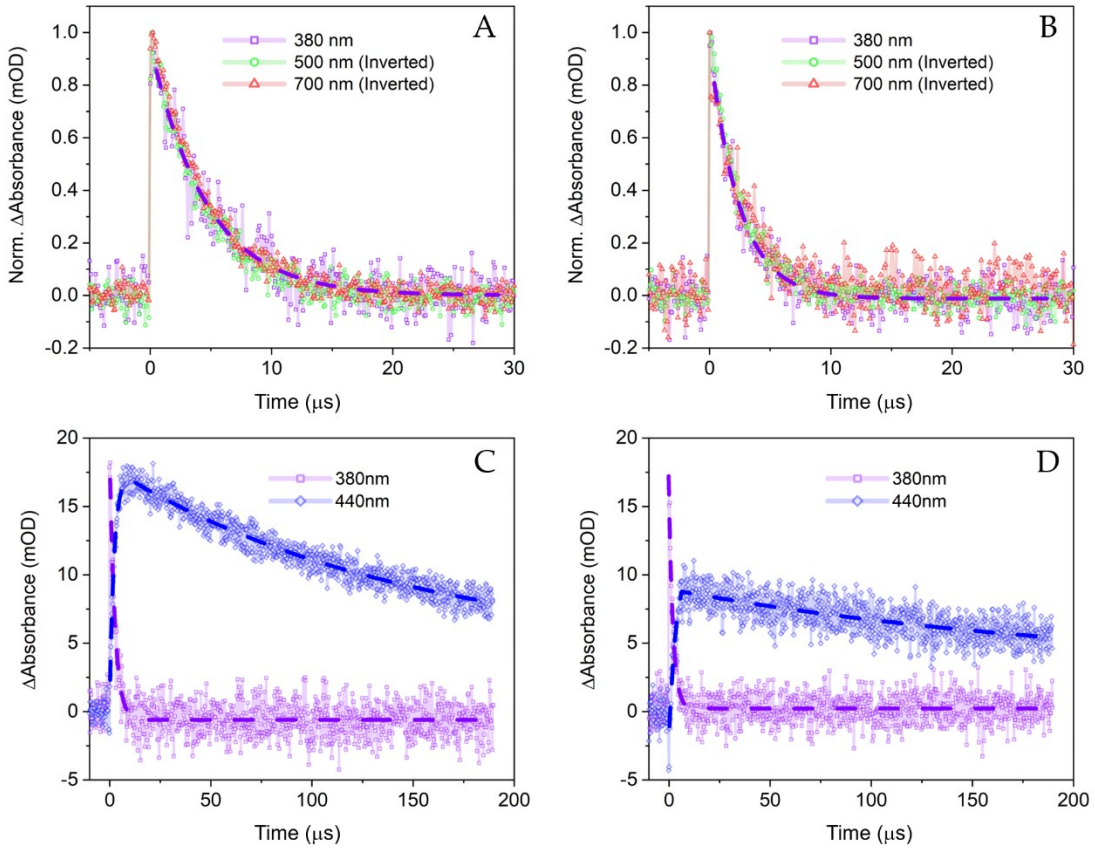

Figure 3.8: The decay transients obtained from nanosecond transient absorption spectra recorded at four different wavelengths (380 nm, 440 nm, 500 nm, and 700 nm), are presented in colors violet, blue, green, and red, respectively. The raw data is depicted using both line and symbol, while the exponential fit is represented by a dashed line. The shown kinetics display normalized decay transients at 380 nm, 500 nm (inverted), and 700 nm (inverted) in Figures (A) and (B). The violet dashed line represents a mono-exponential decay fit to spectra at 380 nm, while the fitting for 500 nm and 700 nm are not presented. The symbol "τ" denotes the duration of the triplet state for each respective species, as denoted by the subscript. (A) **MS**, fits at 380 nm, 500 nm and 700 nm are τ_{MS} are 4.6 μs, 4.3 μs and 4.5 μs respectively. (B) **PS**, fits at 380 nm, 500 nm and 700 nm are τ_{PS} = 2.5 μs, 2.5 μs, 2.6 μs respectively. (C) **M-50**, τ_{MS} = 2.5 μs (violet), build-up τ_{DPA} = 2.1 μs, decay τ_{DPA} = 150 μs (blue). (D) **P-50**, τ_{PS} = 2.0 μs, build up τ_{DPA} = 3.3 μs, decay τ_{DPA} = 230 μs. Reduces Chi-square ≤ 0.003 in all fitting cases. Spectra in A and B are normalized by their respective peak. The error is within 10% of the respective differential absorption signal.

The nanosecond transient decay kinetics of **MS** and **PS** were recorded at 380 nm (ESA), 500 nm (GSB) and 700 nm (SE), as depicted in Figures 3.8A and 3.8B. The curves in the figure demonstrate the decay of ESA, GSB and SE; it is evident that all kinetics

decays with the same lifetimes. Furthermore, the lifetimes obtained through global fitting also yield the same values. The transient decay kinetics observed at 380 nm (reflecting the ESA of the sensitizer) and 440 nm (reflecting the ESA of the annihilator) of **M-50** and **P-50** are presented in Figures 3.8C and 3.8D respectively. The pump-intensity dependent transient absorption data of **MS** and **PS** are shown in Figure 3.9. The kinetics of transient absorption is measured at 380 nm wavelength, which corresponds to the ESA of sensitizer molecules.

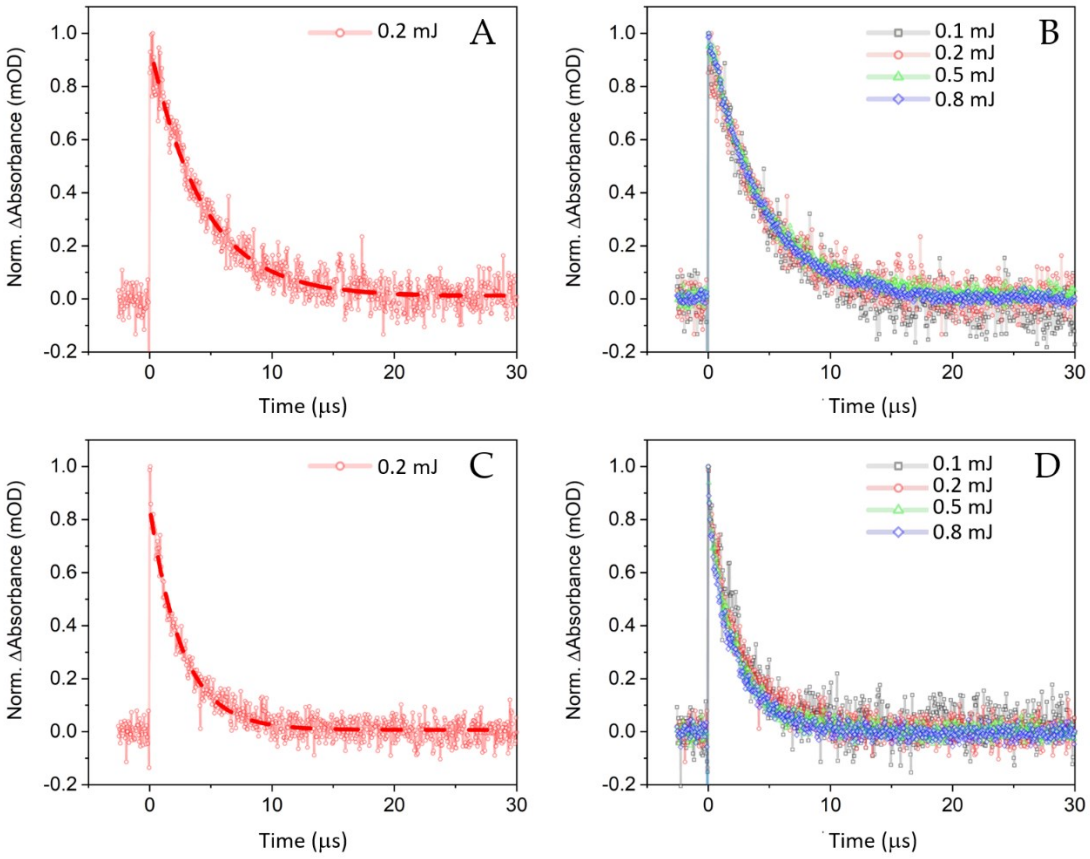

Figure 3.9: The decay of sensitizer triplet lifetime under varying excitation power densities. The measured data (normalized) is represented by a combination of line and symbol, while a mono-exponential decay fit is represented by a dashed line. The symbol "τ" denotes the lifetime of each distinct species, as denoted by the subscript. (A) **MS** - 5 μM, at 0.2 mJ, fit reveals lifetime τ_{MS} = 4.5 μs (B) **MS** - 5 μM, τ_{MS} = 4.5 μs, 4.5 μs, 4.2 μs and 4.2 μs for the energy levels 0.1 mJ, 0.2 mJ, 0.5 mJ and 0.8 mJ respectively. (C) **PS** - 5 μM at 0.2 mJ, τ_{PS} = 2.5 μs (D) **PS** - 5 μM, τ_{PS} = 2.4 μs, 2.5 μs, 2.3 μs and 2.4 μs for the energy levels 0.1 mJ, 0.2 mJ, 0.5 mJ and 0.8 mJ respectively. The error falls within 10% of the specified differential absorption intensity.

The investigation of the triplet lifetime of **MS** and **PS** at energy per excitation pulse 0.1 mJ, 0.2 mJ, 0.5 mJ, and 0.8 mJ is shown in Figure 3.9. The results indicate that the lifetimes of the **MS** and **PS** are centered around 4.4 μs and 2.4 μs, respectively. The

investigation reveals that, there is no significant change in the triplet lifetime of the sensitizer molecules at the employed concentration and pulse energy. The upper threshold for pulse energy is 0.8 mJ due to experimental limitations. No variations in the lifetime of the excited state were observed as a function of pump intensity. Therefore, it can be inferred that sensitizer-sensitizer (S-S) TTA does not play a role in the decay pathway of the triplet excited state in either **MS** or **PS**.

3.4.1 Determination of Triplet-Triplet Energy Transfer Rate

The determination of the triplet-triplet energy transfer rate constant (k_{TTET}) can be done through Stern-Volmer analysis, which is based on the sensitizer triplet lifetimes in the absence (τ_0) and the presence of (τ) DPA. Figure 3.10 illustrates the process of quenching the $^3S^*$ by three distinct concentrations of annihilator (10 µM, 50 µM, 250 µM). The lifetimes of the quenched sensitizers are given in Table 3.2 and are used to make the plot. The Stern-Volmer dynamic quenching equation was utilized to determine the Stern-Volmer constants (K_{SV}) and bimolecular triplet-triplet energy transfer rate constant (k_{TTET}). Equation 2.4 is rewritten here in the context of triplet-triplet energy transfer (TTET) to determine the K_{SV} and k_{TTET}:

$$\frac{\tau_0}{\tau} = 1 + K_{sv}[Q] = 1 + k_{TTET}\tau_0[Q] \qquad \text{Equation 3.1}$$

The Stern-Volmer quenching constant is denoted by K_{SV}, while the concentration of DPA is represented by [Q].

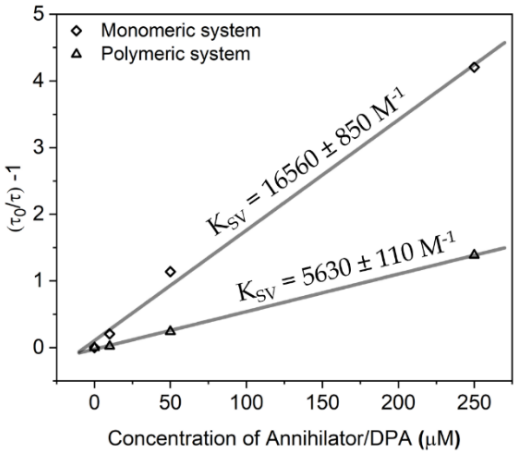

Figure 3.10: Stern-Volmer plot of quenched triplet lifetime of the sensitizer molecules in different concentrations of annihilator. K_{SV} is the quenching constant. R^2(COD) > 0.99 in both fitting cases.

The values of k_{TTET} for monomeric and polymeric systems obtained from the Stern-Volmer plots are $3.6 \cdot 10^9$ $M^{-1}s^{-1}$ and $2.2 \cdot 10^9$ $M^{-1}s^{-1}$, respectively. These results are consistent with previous studies on the energy transfer mechanism between Ruthenium-complex based sensitizers and DPA.[70,192] The higher k_{TTET} observed in the monomeric system can be attributed to the unhindered diffusion of the sensitizer molecules (**MS**). Whereas, in the polymeric system, each macromolecule **PS** is composed of an average of four Ru-complexes located in the sidechains of 75 MMA repeat units within the polymer backbone. The size of a photosensitizer (**PS**) is significantly greater than that of a molecular sensitizer (**MS**), which ultimately restricts the diffusion of the sensitizer molecule and leads to a lower k_{TTET}.[193]

3.4.2 Mixed Kinetic Analysis of Upconversion Systems

The mixed kinetic analysis is performed to obtain the triplet-triplet annihilation rate (k_{TTA}) as described in section 1.5.5. The fitting analysis is performed using Equation 1.31 on the decay of triplet ESA of annihilator.

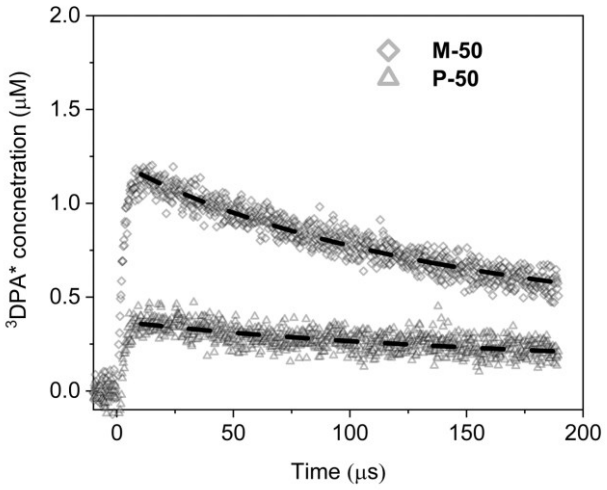

Figure 3.11: k_{TTA} rate calculation for **M-50** and **P-50** using mixed kinetic analysis. The dashed line represents the fit. For both the fits reduced $\chi^2 < 10^{-14}$.

The transient absorbance recorded at 450 nm reflects the concentration of triplet DPA (^{3}A*) as the triplet state in DPA has a characteristic absorption[10] at 450 nm with a molar extinction coefficient of $1.56 \cdot 104$ $M^{-1}cm^{-1}$.[194] The triplet absorption of sensitizer molecule in the Figure 3.5C is negligible at 450 nm, upon addition of annihilator a distinct ESA centered at 425 nm appears due to TTET as described in section 3.3. The mixed kinetic analysis is performed on the annihilator ESA kinetics at 450 nm using Equation 1.31, the fits are shown in Figure 3.11.

The k_T^A which represents the intrinsic triplet lifetime of the annihilator is fixed to 350 s^{-1} during mixed kinetic analysis fit; since its value is 3.1±0.5 ms known from ns-TA measurement shown in Figure 3.7. The parameters obtained from the analysis are summarized in Table 3.3; higher differential absorption intensity (ΔAbsorbance) in the monomeric system leads to a lower error value.

Table 3.3: Parameters obtained from mixed kinetic analysis.

	^{3}DPA* (μM)	β	k_T^A (s^{-1})	k_{TTA} (10^9 $M^{-1}s^{-1}$)
M-50	1.22±0.005	0.94±0.01	350±35	4.3±0.004
P-50	0.37±0.005	0.90±0.01	350±35	9.5±0.42

The ^{3}DPA*, which represents the initial triplet concentration of the DPA is higher for the monomeric system due to a higher number of triplet DPA formations, it is also visible as higher triplet ESA in the monomeric system, see Figures 3.5C & 3.5D.

The dimensionless parameter β represents the initial fraction of the triplet concentration of the annihilator which decays through bimolecular second-order triplet-triplet annihilation is slightly higher for the monomeric system. The bimolecular rate constant k_{TTA} reflects triplet-triplet annihilation, it primarily depends on diffusion coefficient of the annihilator units and the effective distance between two ^{3}A* units participating in annihilation.[86,195] The k_{TTA} rate of the polymeric system is more than twice of the monomeric system, which indicates the relative distance between the two annihilator molecules is shorter in the polymeric system due to upconversion occurring only at hot-spots, it is illustrated in Figure 3.12.

The threshold power density (I_{th}) as described in Equation 1.27 is proportional to the square of k_T^A; inversely proportional to ϕ_{TTET}, $\alpha[^1S]$ and and k_{TTA}. The I_{th} for the **M-50** and **P-50** are 756 mW cm^{-2} and 548 mW cm^{-2} respectively. The efficiency of energy transfer (ϕ_{TTET}) is calculated using lifetime data given in Table 3.2; the substitution of lifetime data in Equation 1.16 yields ϕ_{TTET} values 47% and 20% for **M-50** and **P-50** respectively *i.e.* higher for the monomeric system. The k_T^A (first-order decay rate of the annihilator) value is same for both the monomeric and polymeric systems; since, both systems have DPA as annihilator. Based on the parameters discussed here, the lower I_{th} value for the polymeric system can only result from higher $\alpha[^1S]$ and k_{TTA} of the polymeric system. The k_{TTA} is higher for the polymeric system as described above and $\alpha[^1S]$ which is the absorption cross-section of the sensitizer can be relatively higher for

the polymeric system due to polymer linkage. The polymeric system has a higher number of sensitizer molecules near the upconversion hot-spots; hence, a higher localized concentration of the sensitizer molecules which reflects in the higher $\alpha[^1S]$ value for the polymeric system.[85,88] In conclusion, the higher value of k_{TTA} and higher localized concentration of the polymeric sensitizer reflect in the lower I_{th} value for the polymeric system.

The schematic of homogeneous upconversion in a monomeric system and upconversion from localized hot-spots in a polymeric system is shown in Figure 3.12.

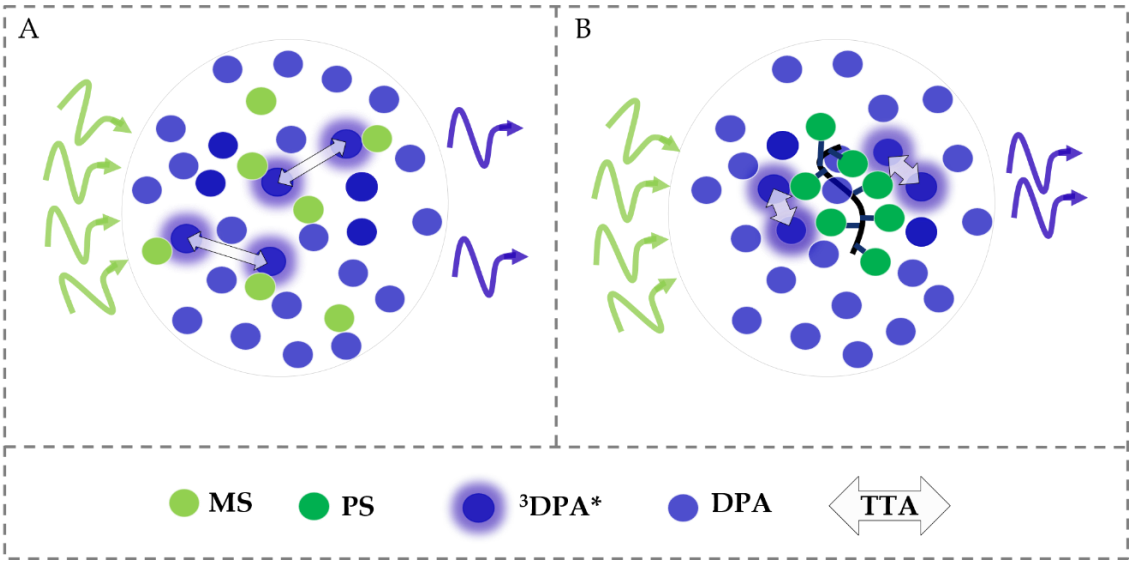

Figure 3.12: (A) Homogeneously distributed sensitizer, annihilator molecules and upconverted emission from monomeric upconversion system (B) Homogeneously distributed annihilator and polymer linked sensitizer molecules, localized upconversion from hot spots in polymeric upconversion system.

4. Investigation of Rotational Dynamics of Fluorophores in Lipid Bilayer Membrane

4.1 The Objective and the Approach

In this chapter, objective 2 has been investigated using steady-state, time-resolved anisotropy and TDDFT computations. To measure the rotational relaxation times using transient absorption anisotropy (TAA), a 4,4-difluoro-4-bora-3a,4a-diaza-s-indacene (BODIPY) derivative in dichloromethane (DCM) and giant unilamellar vesicle (GUV) has been chosen. The choice of the molecule is discussed below before presenting the experimental results. The development of the optical setup for TAA is described in section 2.3.2.

BODIPY fluorophores possess tunable optical properties,[63] high fluorescence quantum yields and large extinction coefficients,[196–198] which serve as the fundamental basis for their application in various fields such as photochemical singlet oxygen generation,[199] molecular rotors[44,49,200–204] and triplet-triplet annihilation upconversion (TTAUC).[10,33] BODIPY-derivatives through meso-substitution of a phenyl ring can be turned in to fluorescent molecular rotors (FMRs), see Figure 4.1B.[44,202] FMRs can be used to investigate the viscosity *e.g.* to determine the viscosity of a cell membrane,[44] which is a crucial factor in drug diffusion. The change from low to high viscosity results in an increase in the fluorescence intensity and lifetime of a BODIPY FMR, which can be attributed to the impeded intramolecular rotation.[44,205]

Giant unilamellar vesicles (GUVs) have been used as models for cellular membranes.[206] Previous studies have investigated the rotational relaxation time, as well as the organization and orientation of different fluorophores (including BODIPYs),[38,42,45,103,207,208] within giant unilamellar vesicles and cellular membranes using the TEA. In this thesis, a BODIPY-derivative BODIPY-Ar-Chol (Figure 4.1A) has been chosen for the investigation of rotational dynamics using TAA. This molecule can be reconstituted into homogeneous and ternary GUVs and are soluble in a range of solvents, *e.g.*, dichloromethane (DCM), acetonitrile (ACN) and chloroform.[63] Hence, their rotational mobility in a range of microenvironments can be inferred from transient absorption anisotropy. In particular, the BODIPY-Ar-chol has been found suitable to target biological cells, where it permeates the membrane and localizes into inner lipid droplets.[63] Having these properties, the BODIPY-Ar-chol molecule presents promising molecular properties to be investigated in GUVs by TAA.

The BODIPY-Ar-chol molecules were dissolved in DCM for measurements in solution and reconstituted with DOPC lipid to form GUVs, the synthesis method is described in section 2.5. The methods of microscopy used in this chapter have been introduced the section 2.4.

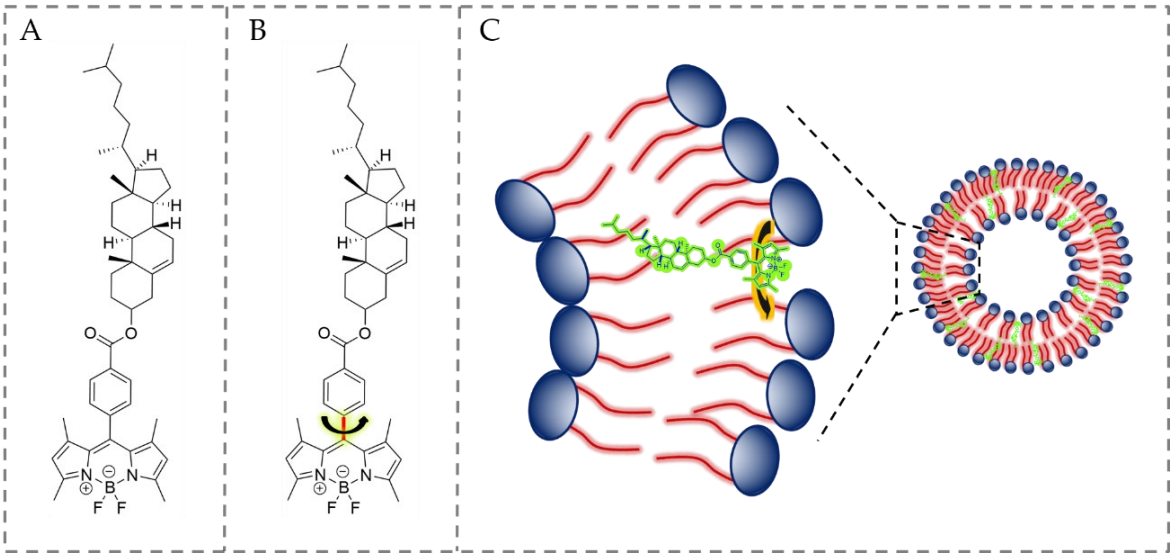

Figure 4.1: (A) Molecular structure of the BODIPY-Ar-Chol molecule (B) Intramolecular rotation between the BODIPY-moiety and phenyl-moiety as a molecular rotor (aroow represents the rotation). (C) The schematic of the recontitution of GUV with the molecule and its possible rotation within the bilayer membrane.

4.2 Steady State Spectroscopy

4.2.1 Absorption and Emission Spectra of the BODIPY-Ar-chol

The steady-state absorption and emission spectra of the BODIPY-Ar-chol molecule in DCM and GUVs are illustrated in Figures 4.2A and 4.2B respectively. The absorption from the electronic ground state (S_0) to the first excited state (S_1) occurs at wavelengths centered at 500 nm. Subsequently, the fluorescence emission peak is at wavelength 514 nm. The extinction coefficient measured at wavelength 503 nm is $6.34 \cdot 10^4$ mol^{-1} cm^{-1}, which is consistent with the literature reports.[63] When the molecule was dissolved in water, no emission was detected. Upon reconstitution into giant unilamellar vesicles (GUVs), the molecule exhibited fluorescence emission that is spectrally identical to the fluorescence observed from DCM solutions, see Figure 4.2B.

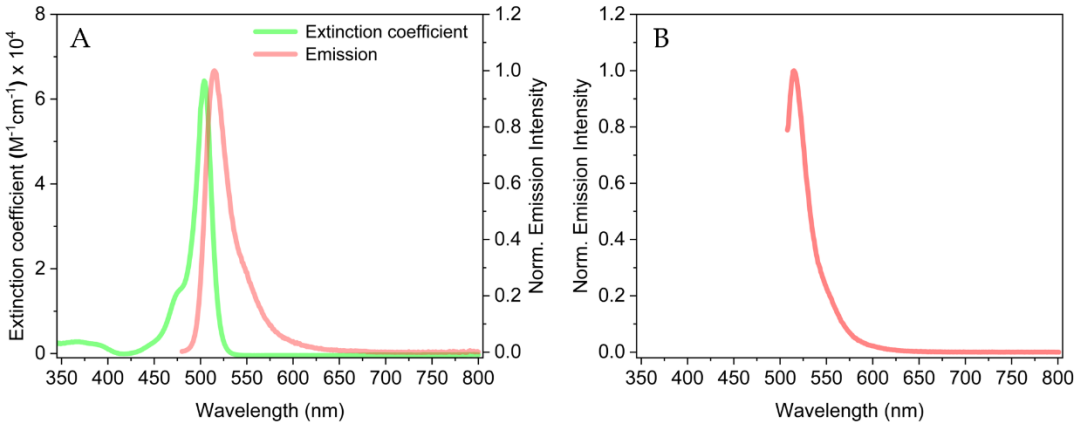

Figure 4.2: (A) Steady-state absorption and emission spectra of BODIPY-Ar-Chol in DCM (B) steady-state emission of the molecule from reconstituted GUV.

4.2.2 Confocal Microscopy and Steady State Anisotropy

The fluorescence image of the BODIPY-Ar-chol molecule reconstituted with GUV is shown in Figure 4.3 indicating that the molecules are embedded into the lipid bilayer membrane.

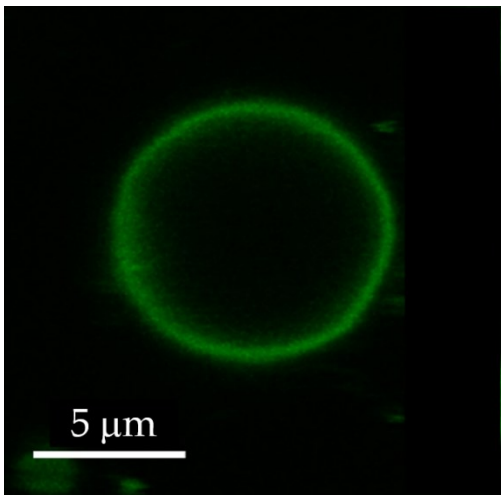

Figure 4.3: Confocal microscopy image of the BODIPY-Ar-chol reconstituted GUV at the equatorial plane. The excitation wavelength is 503 nm using a white light-emitting LED without an excitation polarizer. The emission is collected within the range 511-570 nm, without the use of an analyzer.

The emission from the GUV (Figure 4.3), which is unpolarized, exhibits a uniform distribution throughout the lipid bilayer confirms the synthesized GUVs are homogeneous in nature. However, in the event that the GUV is excited with polarized light and the resulting emission is observed at specified polarization angles, the

emission from the GUV appears uneven (Figures 4.4A and 4.4B). The BODIPY-Ar-chol molecule possesses transition dipole moment (TDM) along the long axis of the BODIPY-moiety;[53,55,209,210] when the TDM aligns with the excitation polarization (as indicated by bidirectional arrows in Figure 4.4A and 4.4B and 4.4E), the BODIPY-Ar-chol molecule becomes excited due to photoselection.[53] The schematic of the photoselection is shown in Figure 4.4E.

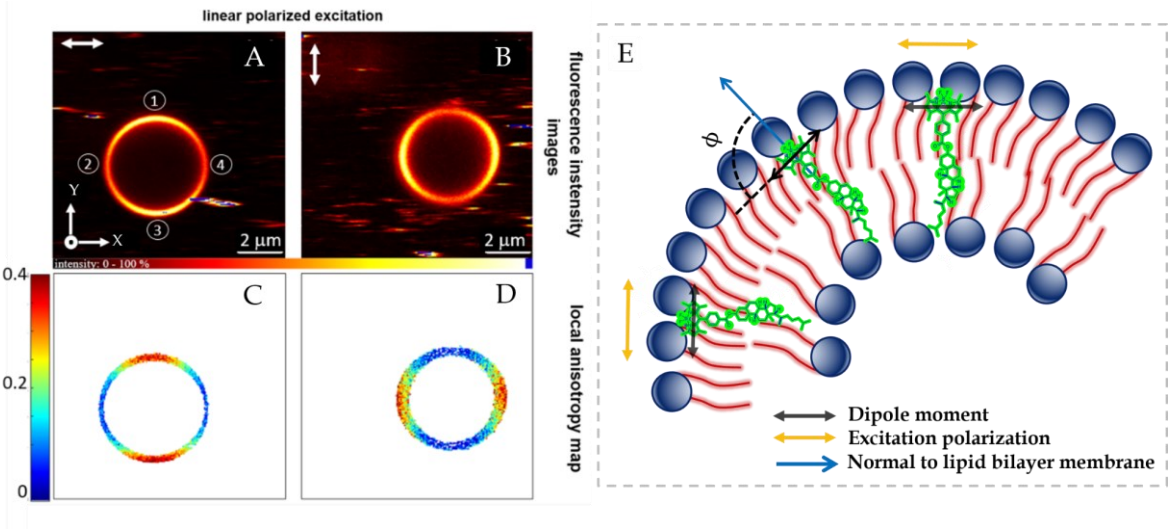

Figure 4.4: Confocal fluorescence images of the equatorial plane of a GUV reconstituted with BODIPY-Ar-Chol. (A,B): The images of the fluorescence intensity (normalized) are obtained by employing two orthogonal linearly polarized excitations. The direction of excitation polarization is indicated by the arrows, and the detected emission is parallel-polarized and denoted as $I_{\parallel}$. The numbers depicted in the image correspond to distinct positions within the equatorial plane of the GUV. (C,D): The anisotropy maps of BODIPY-Ar-Chol within the lipid bilayer membrane for two perpendicular linearly polarized excitations, as depicted in figures (A) and (B) respectively. The color bar displays the color-coded anisotropy values. The intensity threshold was used to eliminate the non-membrane regions from the images. (E): Schemtic representation of the BODIPY-Ar-chol molecule in the GUV and when it gets aligend to the excitation polarization and photoselection. ϕ shows the angle between the transition dipole moment of the BODIPY-Ar-chol molecule and normal to the lipid bilayer membrane.

When excited in the X-direction, higher emission is detected at positions 1 and 3 (as shown in Figure 4.4A) of the Giant Unilamellar Vesicle. This suggests that the molecules located in these positions have dipole moment oriented along the X-axis direction. Similarly, for the excitation along Y-axis (as depicted in Figure 4.4B), it can be observed that there is a significantly higher emission emanating from locations 2 and 4. This can be attributed to the presence of molecules that possess dipole moments oriented along the Y-axis on both sides of the GUV. The photoselection reveals the presence of well-organized BODIPY molecules in the lipid bilayer membrane plane.

The anisotropy is derived from the difference between two fluorescence intensities that are perpendicular to each other (see Equation 1.35); its values are significantly high (r ~ 0.4) in the locations where the emission of a specific polarization is high, while the emission (as well as anisotropy) along the orthogonal direction is diminished by a factor of two. When the excitation polarization is oriented along the X-direction (as depicted in Figure 4.4C), both fluorescence intensity and anisotropy exhibit high values at the top-bottom region of the GUV. Likewise, when the excitation polarization is oriented along the Y-direction, high anisotropy values are observed at the left-right section of the GUV (Figure 4.4D).

The determination of the angle between the dipole moment of the BODIPY chromophore and the normal to the membrane plane is calculated using the fluorescence intensities obtained from the orthogonal positions depicted in Figure 4.4A. The mean value of 40 pixels from two orthogonal locations 1 and 2 or 3 and 4, are substituted in Equation 4.1 to calculate the angle (ϕ) between the dipole moment and the normal to the membrane plane.

$$\frac{I_{\perp}}{I_{\mathrm{II}}} = \frac{1}{2}\tan^2\phi \qquad \text{Equation 4.1}$$

The fluorescence intensity along the axis perpendicular to excitation polarization is denoted as $I_{\perp}$, while the fluorescence intensity along the axis parallel to excitation polarization is represented by I_{II}. This equation is valid for application in homogeneous lipid bilayer membranes. The derivation of Equation 4.1 is published by Grudzinski *et al.*;[211] therefore, not presented in this thesis.

The homogeneity of the GUV membrane is demonstrated using a confocal microscopy image in Figure 4.3 as well as using a fluorescence lifetime imaging microscopy (FLIM) image shown in Figure 4.5. Each pixel in the FLIM image represents the average lifetime of the BODIPY-Ar-chol molecules embedded in the lipid bilayer membrane within the pixel; it is evident that, the lifetime of each pixel is *ca.* 5 ns; which confirms the homogeneity of the lipid bilayer membrane. The substitution of the average of 40 pixels from two orthogonal positions in Equation 4.1 reveals the angle between the transition dipole moment and the normal to the lipid bilayer membrane is 63±2° as depicted in Figure 4.6. As a result of averaging over multiple pixels, the obtained angle is an average of all BODIPY-Ar-chol molecules within the pixels. Karolin *et al.* proposed a similar situation in which BODIPY-derivatives were incorporated into the lipid bilayers of DOPC.[55] The authors observed the transition dipole moment of the BODIPY was oriented perpendicular to the normal to the bilayer

plane. The authors utilized fluorescence anisotropy of giant unilamellar vesicles (GUVs) and formulated their structural hypothesis by analyzing the fluorescence anisotropy measurements, considering an order parameter and linear dichroism measurements.[55]

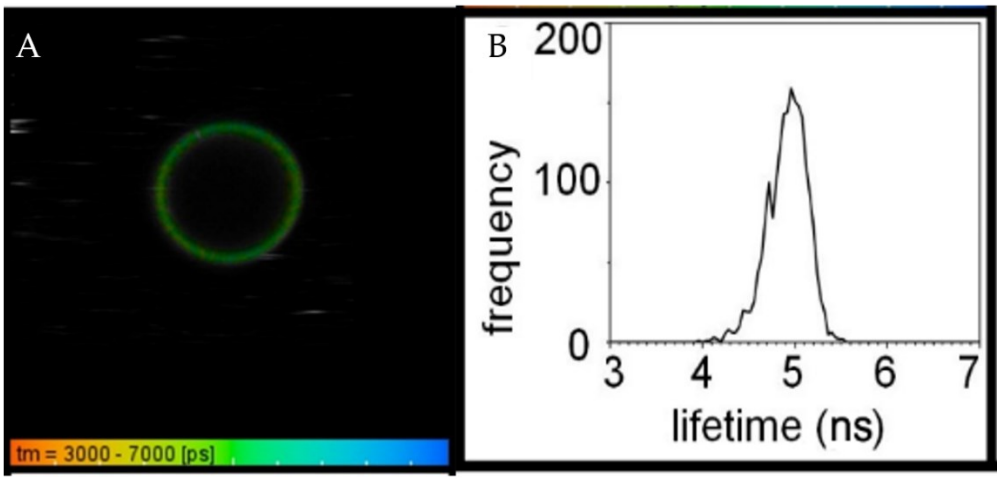

Figure 4.5: Fluorescence Lifetime Image (FLIM) of BODIPY-Ar-Chol reconstituted GUV at the equatorial position. (A): The FLIM image, each pixel represents a lifetime. The selection of pixels is based on intensity thresholds. The GUVs depicted in this figure and Figure 4.4 are identical. (B) The distribution of lifetimes derived from pixels, as depicted in the accompanying image (A).

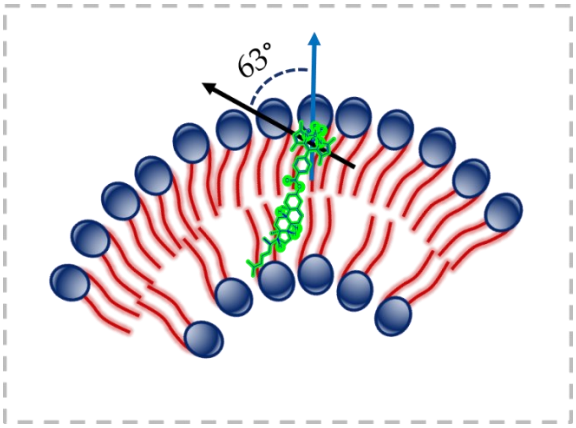

Figure 4.6: The figure depicts a schematic representation of the BODIPY-Ar-chol molecule placed within the lipid bilayer. The molecule's long axis is indicated by a black arrow, which represents the transition dipole moment. Additionally, the vertical blue arrow denotes the normal axis to the surface of the bilayer membrane. The schematic diagram presented does not accurately depict the dimensions of the lipid and BODIPY-Ar-Chol molecules.

Similar observations have been made for the fluorescence intensity and anisotropy of Nile Blue[212] and other molecules in orthogonal sections of the lipid bilayer membrane.

These observations indicate that when the angle between the transition dipole moment of the molecule and the normal to the membrane plane exceeds the magic angle (54.7°) distinct high and low fluorescence intensity as well as anisotropy are observed.[53,213,214]

The orientation and placement of the BODIPY-Ar-chol in lipid bilayer membrane are established; now the rotational dynamics of the BODIPY-fluorophore upon excitation is to be investigated within the lipid bilayer membrane. Two distinct molecular rotations can occur in a BODIPY-phenyl fluorescence molecular rotor (FMR). First, the intramolecular rotation, also known as segmental mobility, involves the rotation of the phenyl ring at a faster rate than the BODIPY-moiety due to the smaller moment of inertia of the phenyl ring.[44] The BODIPY-Ar-chol molecule under investigation exhibits restricted rotation of the phenyl group due to the presence of a methyl group at position 1,7. However, there is some degree of rotation, albeit restricted, between the BODIPY and phenyl moieties. Previous report suggests that, the emission quantum yield can be further enhanced by adding substituents on the ortho and meso position of the phenyl ring. This is attributed to the increased restriction on the rotation of the phenyl ring.[49,197,202,215] Consequently, the segmental mobility exits between the BODIPY-moiety and phenyl ring. The angle of rotation is investigated using the TDDFT calculation and described in the next section. Second, the BODIPY-phenyl fluorophore exhibits a rotational motion as one unit. The comparatively large moment of inertia of the BODIPY-moiety results in a significantly slower rotation in comparison to the intramolecular rotation.[216,217] As a result, it can be observed that within solvents of low viscosity, the decay properties of emission are primarily influenced by intramolecular rotation. In media with high viscosity, both intramolecular rotation and the overall rotation of the FMR are slowed down.[200,218]

4.3 Computational Simulations on the Transition Dipole Moment

4.3.1 The Orientation of Absorption and Emission Transition Dipole Moments

The computational simulations are performed to investigate the change in the orientation of transition dipole moment (TDM) due to intramolecular rotation and solvent reorganization. The simulations are performed by Dr. Julien Guthmuller and Mr. Rengel Cane Sia. The details of the methods are described in section 2.5.

The Cartesian coordinates of the transition dipole moments of BODIPY-Ar-Chol at the S_0 and S_1 geometries, as well as the angle between the TDMs, are given in Table 4.1 (the TDM at S_0 geometry is considered as the reference). The simulations indicate a

marginal angle 0.13° between the TDM of S_0 and S_1 geometry *i.e.* the absorption and emission dipole moments are collinear.

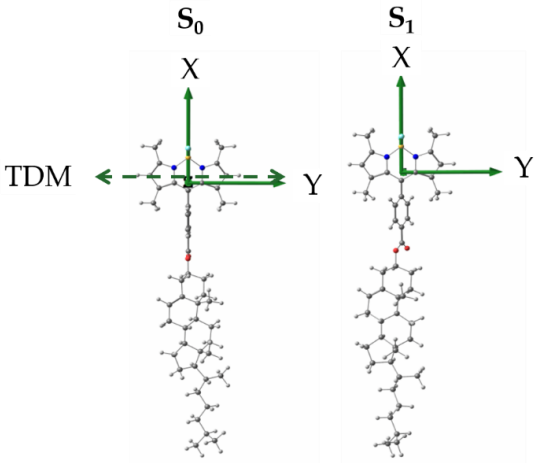

Figure 4.7: The molecule-fixed Cartesian frame and the optimized geometries of the S_0 and S_1 states of BODIPY-Ar-Chol. The TDM is along the long axis of BODIPY-core and parallel to Y-axis, it is shown as bidirectional dashed line.

Table 4.1: Cartesian coordinates of the TDM at S_0 and S_1 geometry and the angle between TDMs at S_0 and S_1 geometry of the BODIPY-Ar-Chol.

Geometry	X (a.u.)	Y (a.u.)	Z (a.u.)	Angle between TDMs (°)
S_0	-0.0049	2.9738	-0.0303	0.00
S_1	0.0022	3.3900	-0.0356	0.13

The atomic numbering of the BODIPY-Ar-chol molecule is shown in Figure 4.8, based on the atomic numbers dihedral angles are calculated and shown in Table 4.2.

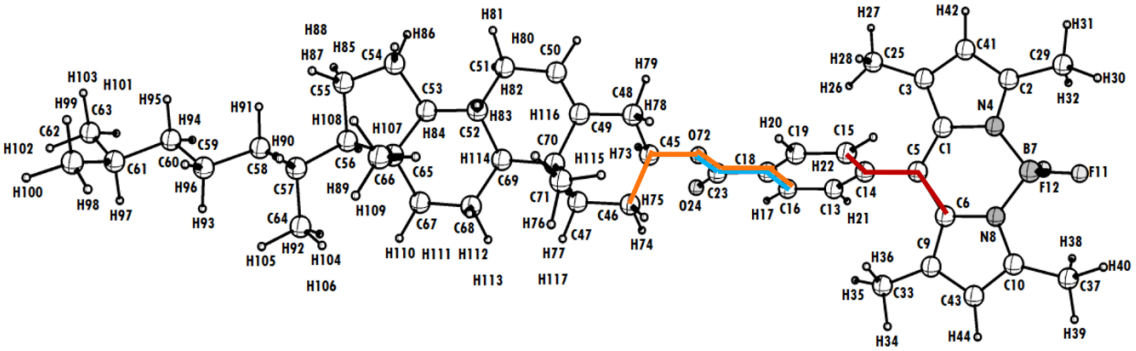

Figure 4.8: The numbering of the atoms of BODIPY-Ar-chol molecule. The dihedral C6-C5-C14-C15 is shown in red, dihedral C16-C18-C23-O72 is shown in blue, dihedral C23-O72-C45-C46 is shown in orange color.

4.3.2 The Effect of Intramolecular Rotation on TDM

The intramolecular rotation between the BODIPY-moiety and phenyl ring is given in Table 4.2 and discussed thereafter. The transition from the Franck-Condon geometry (S_0 state) to the emissive state (S_1 state) results in a rotation of approximately 24° around the BODIPY and phenyl ring. However, negligible rotations are observed along the C18-C23 and O72-C45 bonds that link the aryl, ester, and cholesterol groups. The directional orientation of TDM exhibits no significant changes in the geometrical relaxation, with an angle of *ca.* 0.1°; therefore, TDM remains predominantly aligned along the long axis of the BODIPY-Ar-chol (Y-axis). Since, there is no rotation between the phenyl ring and cholesterol, the cholesterol group is removed to simplify the calculations. Consequently, further calculations are based on the BODIPY-Ar-COOH compound (shown in Figure 4.9).

Table 4.2: The dihedral angle between the BODIPY and phenyl ring as well as phenyl ring and cholesterol, the dihedrals are shown in colors in Figure 4.8.

Geometry	C6-C5-C14-C15	C16-C18-C23-O72	C23-O72-C45-C46
S_0	90.8	180.0	80.8
S_1	114.4	179.8	80.8
Difference in angle (°)	23.6	-0.2	0.0

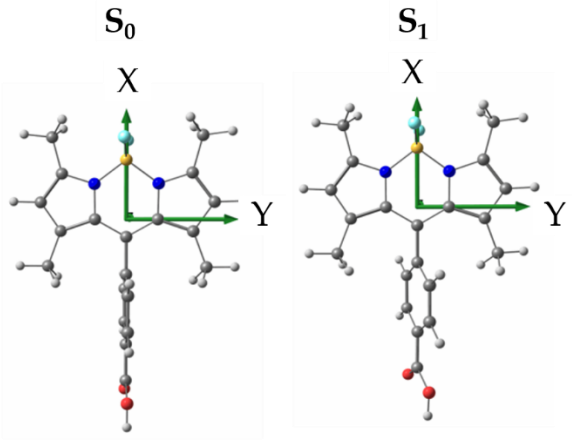

Figure 4.9: The molecule-fixed Cartesian frame and the optimized geometries of the S_0 and S_1 states of BODIPY-Ar-COOH. The TDM is along the Y-axis, as shown in the figure.

Table 4.3: Cartesian coordinates and the angle between TDMs of BODIPY-Ar-COOH at S_0 and S_1 geometry.

Geometry	X (a.u.)	Y (a.u.)	Z (a.u.)	Angle between TDMs (°)
S_0	-0.0007	3.0648	-0.0347	0.00
S_1	-0.0004	3.5934	0.0182	0.94

Table 4.4: The dihedral angle between the BODIPY and phenyl ring

Geometry	BODIPY-Ar (°)
S_0	83.8
S_1	66.6
Difference	17.2

At the Frank-Condon geometry (S_0), it can be observed that the BODIPY and phenyl moieties exhibit a near-orthogonal configuration, characterized by a dihedral angle of 83.8°. The BODIPY-phenyl dihedral angle is 66.6° at the S_1 geometry. The impact of the phenyl ring rotation on the TDM during the transition of the molecule from its Franck-Condon geometry to its first excited state (S_1) geometry with a BODIPY-phenyl rotation of 17.2° is observed to be 0.94°. The obtained values for BODIPY-Ar-COOH are consistent with the computed data for BODIPY-Ar-Chol.

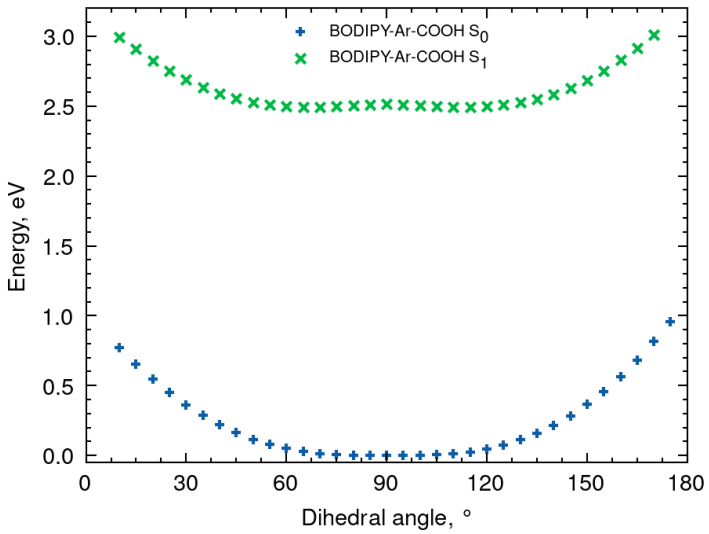

Figure 4.10: Scan of the relaxed potential energy surface of S_0 and S_1 states of BODIPY-Ar-COOH along the BODIPY-Ar dihedral angle.

The potential energy surface (PES) of S_0 state indicates that the minimum dihedral

angle is in close proximity to 90° (Figure 4.10). Additionally, rotations between 65° and 115° are attainable at room temperature, where kT equals 0.026 eV. This particular rotation results in a maximum angle deviation of *ca.* 2.8 degrees in TDM. The S_1 PES indicates that the lowest dihedral angle is approximately 65° and dihedral angles ranging from 55-125° are attainable at room temperature. This results in a TDM deviation of a similar magnitude to S_0 geometry, *ca.* 3°.

4.3.3 The Effect of Solvent Reorganization on TDM

The impact of solvent reorganization on the TDM at the ground state (S_0) and excited state (S_1) geometries is insignificant, as evident by a maximum TDM angle deviation of 0.36° (Tables 4.5 and 4.6).

Table 4.5: The Cartesian coordinates of the TDMs of BODIPY-Ar-COOH at the S_0 geometry computed using both non-equilibrium and equilibrium dichloromethane (DCM) solvation models. Additionally, the angle between the TDMs are given. (the TDM calculated for the non-equilibrium is the reference).

Solvation	X (a.u.)	Y (a.u.)	Z (a.u.)	Angle between TDMs (°)
non-equilibrium	-0.0007	3.0648	-0.0347	0.00
equilibrium	0.0002	3.6419	-0.0644	0.36

Table 4.6: The Cartesian coordinates of the TDMs of BODIPY-Ar-COOH at the S_1 geometry computed using both non-equilibrium and equilibrium dichloromethane (DCM) solvation models. Additionally, the angle between the TDMs is given. (the TDM calculated for the non-equilibrium is the reference).

Solvation	X (a.u.)	Y (a.u.)	Z (a.u.)	Angle between TDMs (°)
non-equilibrium	-0.0005	3.0117	0.0291	0.00
equilibrium	-0.0004	3.5934	0.0182	0.26

4.4 Time-resolved Anisotropy of BODIPY-Ar-chol in DCM and Lipid Bilayer Membrane

4.4.1 Anisotropy Decay of a Non-spherical molecule

The decay components of time-resolved anisotropy of a rigid molecule depend on its shape. A rigid spherical molecule which has the same axes length in three-dimensions has only one rotational diffusion coefficient and contains only one anisotropy decay

component and associated rotational relaxation times. Its rotational relaxation time is obtained by fitting the anisotropy decay curve using a mono-exponential decay as described in Equation 1.40.[59] However, for a non-spherical molecule the anisotropy decays multi-exponentially due to different rotational diffusion along the three axes (see Figure 4.11). Three different rotational relaxation times are obtained by fitting the anisotropy decay curve using the multi-exponential decay as described in Equation 1.41.[41,59,105]

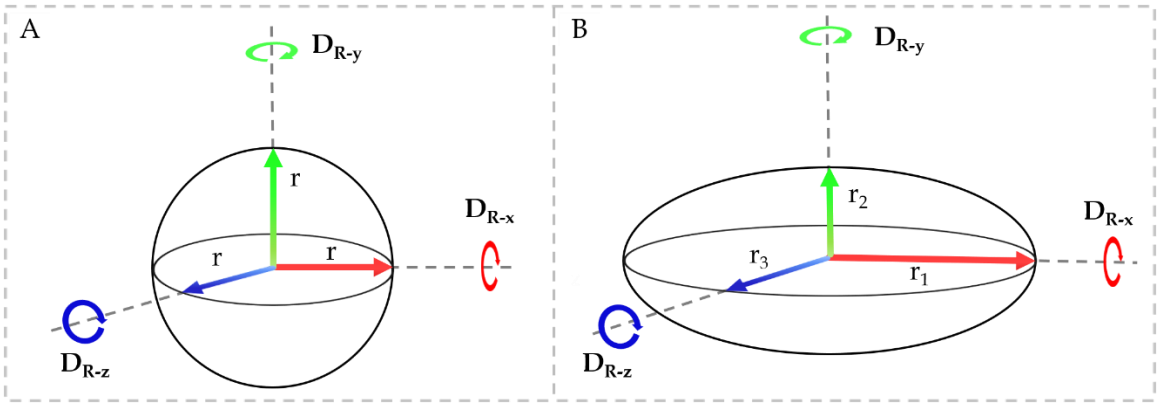

Figure 4.11: (A) Rotational diffusion of a spherical shape along three axes are same; $D_{R-X} = D_{R-y} = D_{R-z}$; D_{R-X}, D_{R-y} and D_{R-z} are the rotational diffusion along X, Y and Z axis respectively. (B) Rotational diffusion of a non-spherical shape along the three axes are different; $D_{R-X} \neq D_{R-y} \neq D_{R-z}$.

4.4.2 Time-resolved Emission Anisotropy and Transient Absorption Anisotropy

The rotational dynamics of a molecule is obtained through TEA and TAA. Figure 4.12 depicts the magic angle kinetics of transient emission (observed at 514 nm) and transient absorption (observed at 525 nm) along with the corresponding anisotropy of BODIPY-Ar-chol in both DCM and GUV. The magic angle signal and time-resolved anisotropy are calculated using Equations 1.37 and 1.39 respectively. The kinetics of the magic angle (as depicted in Figures 4.12B and 4.12D) exhibit negative differential absorbance (ΔAbsorbance) signals at approximately 525 nm, indicating the contribution from ground-state bleach (GSB) and stimulated emission (SE). This observation is in line with the steady-state spectra (as shown in Figure 4.2) and previous studies on BODIPY-derivatives.[134,216] The anisotropy data depicted in Figures 4.12B and 4.12D are within the range of 0.4 to 0.04. However, a few data points that exceed 0.4, as observed in the GUV samples (Figure 4.12D), are considered outliers due to the higher margin of error (±20%) of the measured differential

absorbance signal.

In general, a comparison between the BODIPY-Ar-chol fluorophore in solution and anchored to GUVs reveals different anisotropy values at long delay times (*ca.* 2 ns). The fluorophore in the DCM solution exhibits a high initial anisotropy (*ca.* 0.4) and decays to approximately 0.04 within 2 ns. The anisotropy of the fluorophores anchored to GUVs is approximately 0.1 within the same 2 ns timescale. The high initial anisotropy indicates that the absorption and emission transition dipoles are collinear.[59,212] This finding is supported by TDDFT calculations, which predicted a small angle of 0.13° between the two transition dipoles (see Table 4.1).

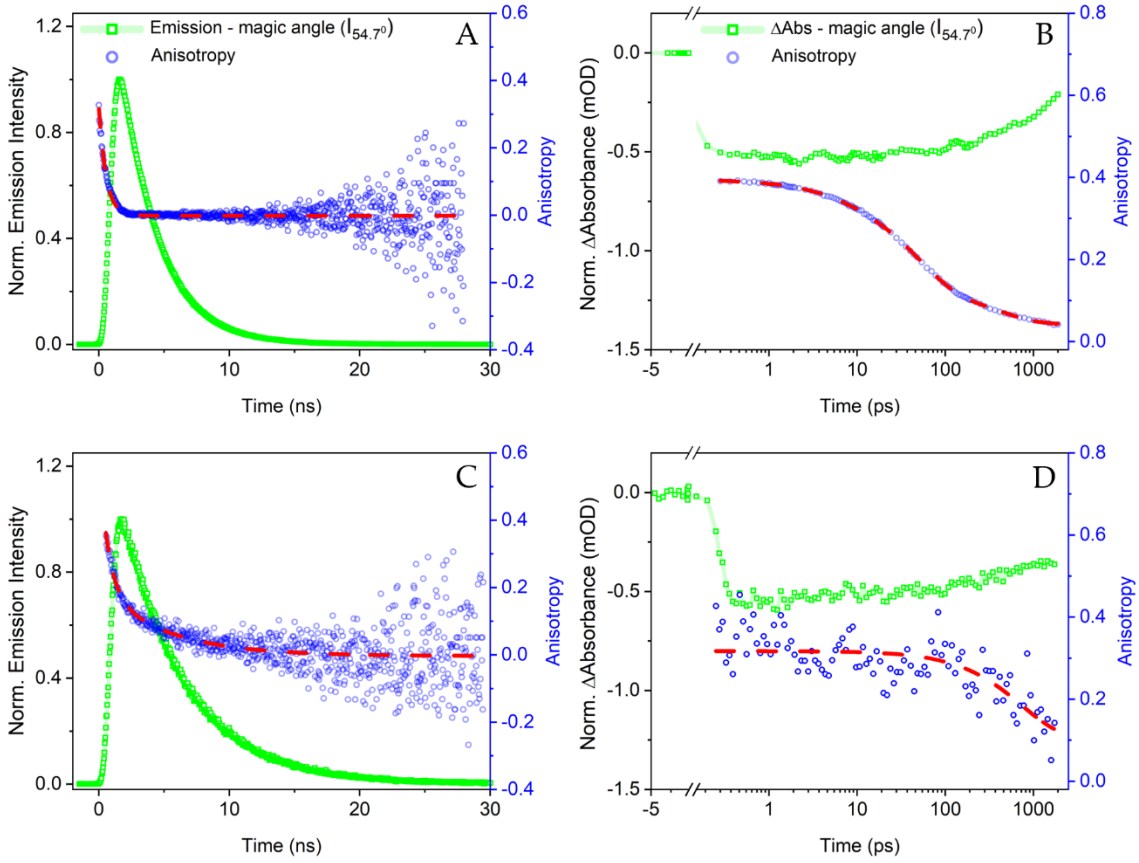

Figure 4.12: Magic angle kinetics in green and anisotropy decay in blue for BODIPY-Ar-chol molecule (A) TEA in DCM, mono-exponential fit in red with lifetimes 550 ps, error value is within 20% of the given value, χ^2 (reduced) = 0.03 (B) TAA in DCM, triexponential fit in red with lifetimes 2 ps, 43 ps, 440 ps, the error value is within 5% of the given value, χ^2 (reduced) < 10^{-5} (C) TEA in GUV, biexponential fit in red with lifetimes 700 ps, 5.3 ns, error value is within 20% of the given value, χ^2 (reduced) = 0.04. (D) TAA in GUV, monoexponential fit in red with lifetime 700 ps, error value is within 20% of the given value, χ^2 (reduced) = 0.02. Legends for TEA (A, C) are the same and for TAA (B, D) are the same.

The BODIPY-Ar-Chol molecule has a non-spherical body, resembling an ellipsoid

with distinct axes, as depicted in Figure 4.13. The ellipsoid's principal semi-axes measure 21.6 Å, 6.132 Å, and 4.507 Å along the X, Y, and Z axes respectively. The dimensions of the axis suggest that the molecular structure closely resembles that of a prolate ellipsoid, with one long axis oriented along the X-axis, and two shorter axes oriented along the Y and Z axes, respectively. In the depicted molecular frame, as presented in Figure 4.13, the transition dipoles for absorption and emission are oriented along the Y-axis and are perpendicular to the long axis (X-axis). The rotation around the X-axis is considered to be faster due to the comparatively less displacement of solvent molecules along this axis. Conversely, the rotation around the Y-axis is considered to be slower due to the large displacement of solvent molecules. The rotational movement around the Z-axis is expected to exhibit similarities to that of the Y-axis, due to the comparable moment of inertia.[59]

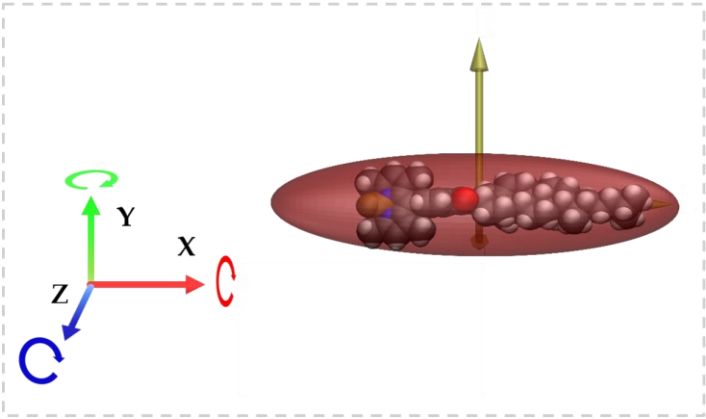

Figure 4.13: The van-der-Waals surface of the BODIPY-Ar-Chol molecule along with the depiction of its principal axes as arrows and the associated Löwner-John ellipsoid. The dimensions of the ellipsoid are depicted along the X-axis (in red), Y-axis (in green), and Z-axis. (blue). The circular arrow denotes the rotational diffusion that occurs around each respective axis.

The decay of TAA in DCM exhibits three distinct time-constants 2 ps, 43 ps, and 440 ps, see Figure 4.12B. The anisotropy decay time-constants are tabulated in Table 4.7. The time-constant 440 ps, which is the slowest component, may be attributed to the rotational diffusion along the Y-axis as well as the Z-axis of the prolate ellipsoid. Subsequently, the time-constants of 43 ps may arise from the rotational diffusion around the X-axis. It is improbable that the fastest anisotropy decay component (2 ps) is originating from rotational diffusion around any of the three axes.

In a previous study, Ariola *et al*. determined two distinct time-constants 180 ps and 800 ps for a structurally similar BODIPY-col molecule, it was obtained using time-resolved emission anisotropy measurements in dimethyl sulfoxide (DMSO, with viscosity 2 cP at 293 K),[38] two time-constants might associate with long and short axis

of the molecule respectively. The BODIPY-Ar-Chol molecule used in this work, on the other hand, was measured in DCM, which has viscosity 0.43 cP at 293 K.[219] As a result of lower viscosity, the rotational relaxation time for this molecule is determined to be 550 ps using time-resolved emission anisotropy (TEA), see Figure 4.12A. The higher resolution of the TAA anisotropy employed in this work facilitated to resolve all three rotational relaxation times. In line with the TEA anisotropy decay obtained in this thesis work, various other reports indicated only one rotational relaxation time for various other BODIPY-derivatives using TEA.[216,217]

Table 4.7: Rotational relaxation times and pre-exponential factors of the anisotropy decays shown in Figure 4.12

	Time-Constants (ps)			Pre-exponential factor			Time Average (ps)
	τ_1	τ_2	τ_3	A_1	A_2	A_3	
TEA-DCM	550±100		-				-
TEA-GUV	700±140	5050±1100	-	0.41±0.14	0.20±0.044		2143±400
TAA-DCM	2±0.04	43±2	440±22	0.034±0.01	0.23±0.02	0.09±0.01	142±10
TAA-GUV	700±140	-	-	0.22±0.05			-

Previous studies have suggested that the intramolecular rotation (segmental mobility) of the chromophore may change the orientation of the TDM, thereby playing a role in the decay of the anisotropy.[59,220] The impact of intramolecular rotation on the orientation of the TDM within the molecular frame was examined through TDDFT calculations, as described in section 4.3.2. The transition from the S_0 state to the S_1 state results in a change of 1° in TDM orientation. Moreover, through an examination of the potential energy surface with respect to the BODIPY-phenyl dihedral angle, it is possible to approximate that the TDM orientation undergoes a change of 3°.

Similarly, previous reports have indicated that the solvation of solute-solvent pairs exhibit changes in anisotropy.[146,221] In this thesis work, TDDFT calculations in conjunction with a polarizable continuum model were employed to examine the decay of solvation-induced anisotropy, as described in section 4.3.3; it predicts a minor rotation of *ca.* 0.3° in the TDM orientation as a result of solvent relaxation.

The fastest 2 ps component may originate from the structural relaxation (change in

BODIPY-phenyl dihedral angle), which accounts for *ca.* 3° change in TDM. The pre-exponential factor for 2 ps time-constant is ~0.03, which is only ~7% to the initial anisotropy (see Table 4.7); where the sum of all pre-exponential factors is equal to the total anisotropy (r_0, initial anisotropy).[59] The time-scale of the structural relaxation process is similar to the 2 ps anisotropy decay component.[216,221,222]

When reconstituted into a GUV composed of DOPC, the movement of the BODIPY-Ar-chol is impeded,[38,42,44,56] resulting in an increased local viscosity experienced by the chromophore probed using TAA. The TAA demonstrates a decay of characteristic time constant 700 ps (Figure 4.12D). Nevertheless, the anisotropy did not exhibit complete decay within a time frame of 2 ns. It is to be noted that the TTA measurement was restricted to a maximum timescale of 2 ns, due to the limitation of the dynamic range of the optical delay line. The TEA measurement, which is not constrained to this limitation, recorded the anisotropy decay up to 25 ns (Figure 4.12C). The results indicate the presence of two time-constants 700 ps and 5.1 ns.

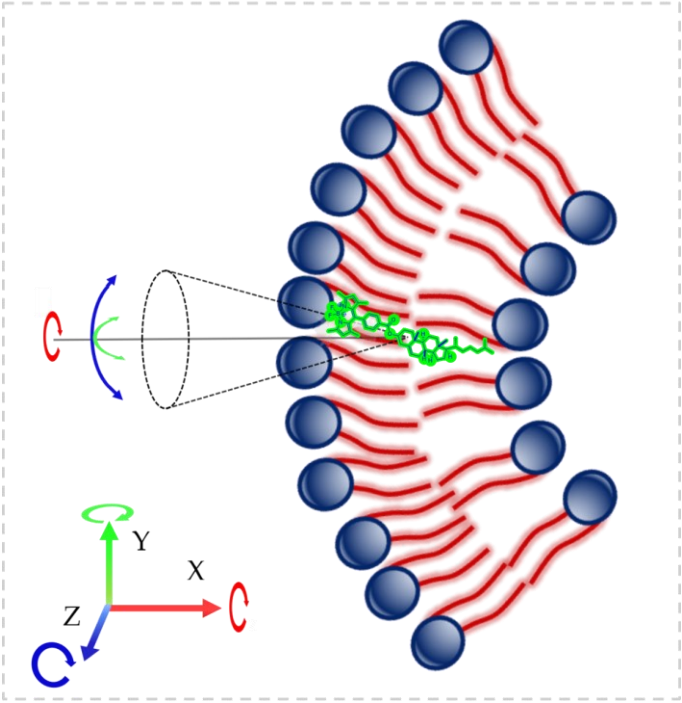

Figure 4.14: Possible orientation of the BODIPY-Ar-Chol in the lipid bilayer membrane as obtained using anisotropy measurements of GUV through confocal microscopy and corresponding wobble-in-cone motion.

The time-constants exhibited in the lipid bilayer medium are comparatively slower than those observed in DCM, due to the steric constraints imposed by the high viscosity of the lipid bilayer (*vide infra*). Most likely, the two time-constants are associated with the wobble-in-a-cone movement of the BODIPY-Ar-chol molecule

within lipid bilayer media of high viscosity.[39,223,224] In a wobble-in-a-cone motion, two kinds of motion takes place, the rotation around the normal to lipid bilayer membrane and wobble motion (back-and-forth) away from the normal to lipid bilayer membrane.[39,223,224]

The BODIPY-Ar-chol molecule is incorporated within the membrane, with its BODIPY moiety located in close proximity to the polar headgroups as previously mentioned. Additionally, the cholesterol is oriented parallel to the acyl-chain of the DOPC.[38,42,55,203] The observed time-constant 700 ps can be attributed to the fast rotation around the X-axis, while the slow back-and-forth flip (wobble) motion of the molecule away from the normal (as depicted in Figure 4.14) may account for the time-constant 5.1 ns.

4.4.3 The Calculation of Microviscosity of the Lipid Bilayer

$$\tau_{avg} = \frac{\Sigma_{i=1}^{n} A_i \tau_i}{\Sigma_{i=1}^{n} A_i} \qquad \text{Equation 4.2}$$

$$\frac{\tau_1}{\tau_2} = \frac{\eta_1}{\eta_2} \qquad \text{Equation 4.3}$$

The average rotational relaxation time for DCM and DOPC GUV are 142 ps and 2.1 ns, respectively. These values are obtained using Equation 4.2,[59] exponential decay factors are tabulated in Table 4.7. The microviscosity of the GUV is estimated to be 6.4±1.2 cP using Equation 4.3. This value is consistent with previous literature reports on the microviscosity of homogeneous GUVs composed of DOPC.[56]

In summary, the TAA offers advantages in obtaining the anisotropy of non-spherical molecules, resolving the fast anisotropy decay component (<50 ps) and measuring the anisotropy decay at a sub-picosecond timescale that surpasses the resolution limit of most time-resolved fluorescence emission measurement systems.[59,220,221] The investigation of the fast decay components of anisotropy provides the rotational diffusion around the smaller axis of the molecule. The slow components of anisotropy observed using TEA are critical for measuring rotational relaxation motion in highly viscous environments.[55,103,225]

The methodology has the potential to be extended for the purpose of measuring the microviscosity of ternary giant unilamellar vesicles consisting either emissive or non-

emissive chromophores, as well as in media where emission is quenched or restricted. This is due to the fact that the TAA technique solely relies on the absorption properties of the chromophore. These findings can be extended to the biological cell environment, where molecules of physiological significance have been previously examined in cells using transient absorption (TA) spectroscopy.[226] In the context of light-triggered drug delivery through TTAUC, wherein the diffusion of molecules has significant importance,[9,33] the selective observation of sensitizer and annihilator molecules within vesicles by TAA may serve to provide the rotational diffusion times (*i.e.*, local diffusion rates, D_R) of the sensitizer and annihilator molecules and provide deeper insight into the upconversion process in vesicles.

5. Triplet-Triplet Annihilation Upconversion in Model Membranes

5.1 The Objective and the Approach

In this chapter, objective 3 has been investigated. The first part of this chapter deals with the investigation of triplet formation in BODIPY-perylene dyads of non-orthogonal configuration, with and without iodine substitution using femtosecond transient absorption spectroscopy and TDDFT computation simulations. Subsequently, triplet state properties and the TTAUC mechanism are investigated using nanosecond transient absorption spectroscopy in both 1,4-dioxane and lipid bilayer membranes. The choice of the molecules (dyad) and suitability of the spectroscopic method are briefly explained before presenting the experimental results.

The triplet formation *i.e.* intersystem crossing (ISC) in a molecule or complex can occur through spin-orbit (SO) coupling,[227,228] spin-orbit charge transfer intersystem crossing (SOCT-ISC)[229–235] or radical pair intersystem crossing (RP-ISC), explained later in the text.[227,228,236,237] The SO coupling strength is a determining factor for effective triplet formation.[227,228] Transition metal complexes have faster ISC and higher triplet yield but relatively small (with respect to organic molecules) molar absorption coefficient (ε) in the visible region.[67] On the other hand, 4,4-difluoro-4-bora-3a,4a-diaza-s-indacene (BODIPY) fluorophores have much higher molar absorption coefficient and tunable photophysical properties but their triplet yield is much lower.[108,199,238,239] The substitution of heavy atoms in BODIPY enhances the triplet yield by coupling S_1-T_1 states;[108,240–244] however, the substitution of heavy atoms such as iodine or bromine also couples the T_1-S_0 states and effectively lowers the triplet lifetime.[233] Therefore, SOCT-ISC which does not couple T_1-S_0 states but, relies on charge separation and recombination to form a triplet species provides a longer triplet lifetime.[233] The triplet formation through SOCT-ISC needs an orthogonal geometry of donor-acceptor molecules to form a charge separation and charge recombination mechanism.[199] In this context, several BODIPY-based donor-acceptor pairs have been reported.[199,233,239,245–254] However, the effect of iodine and non-orthogonal configuration on SOCT-ISC is yet not explored. Therefore, in this thesis work ISC mechanism in non-orthogonal BODIPY-perylene dyads has been investigated, the molecular structure is given in Figure 5.1.

To perform TTAUC in lipid bilayer membrane, similar to solutions the sensitizer and annihilator need to have long triplet lifetimes (100 μs to several ms) which will allow

them to diffuse longer in the sterically hindered media (lipid environment) to provide high TTET and TTA yields.[65,98] The sensitizer needs to have a high Φ_{ISC} to form a large number of triplets. The reconstitution of the two molecules in the membrane can be done with a maximum of a few μM concentrations; otherwise, excess molecules will not be embedded into the bilayer but rather float in the solvent around the membrane. To work with low concentrations, the lipophilic molecules need to have high absorption (extinction) coefficient. BODIPY-perylene dyads along with a long triplet-lifetime have a very high absorption coefficient[233,255] and BODIPY-derivatives are lipophilic in nature,[63,65] these properties make BODIPY-perylene dyads suitable for upconversion studies in membranes.

The charge separation and recombination processes occur within a few nanoseconds; therefore, femtosecond transient absorption spectroscopy and computational simulations are employed to determine the intersystem crossing (ISC) rates.[251] The triplet state properties and TTAUC mechanism of BODIPY-perylene dyad as sensitizer and additional perylene as annihilator are investigated using nanosecond transient absorption spectroscopy.

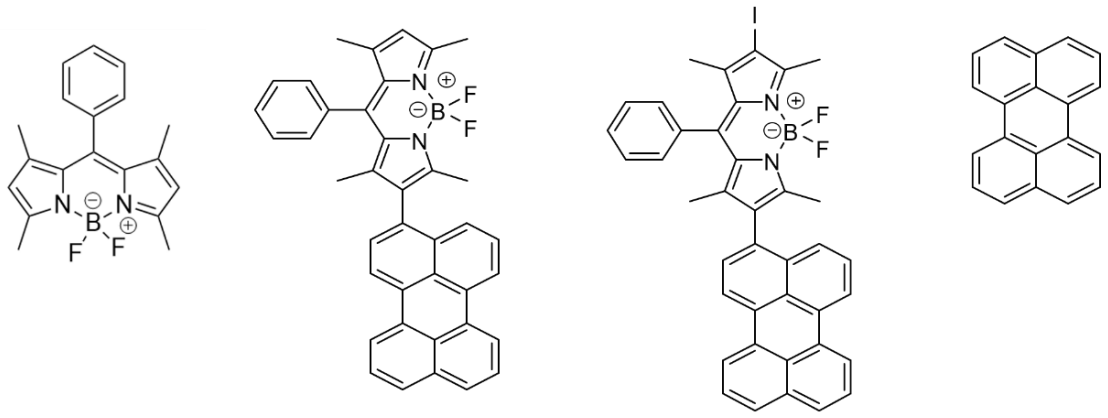

Figure 5.1: Molecular structure of (A) BODIPY-phenyl (B) B2P (C) B2PI (D) perylene

The perylene is linked at position 2 of the BODIPY: Ph-2-BODIPY-2_Perylene dyad without iodine is called B2P and Ph-2-BODIPY-2_Perylene-Iodine dyad with iodine is called as B2PI. The absorption and emission spectra are given in Figure 5.2. The details of synthesis and spectroscopic methods are given in Chapter 2.

5.2 Steady State Absorption and Emission Spectroscopy

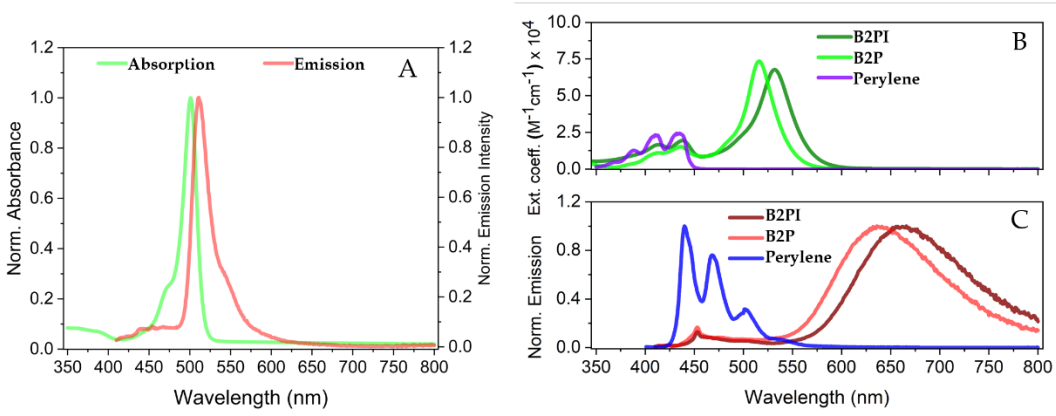

Figure 5.2: (A) Normalized absorption and emission spectra of BODIPY-phenyl molecule, excitation at 400 nm (B) absorption spectra of B2P, B2PI and perylene (C) emission spectra of B2P, B2PI and perylene, excitation at 400 nm. All spectra are meausred in 1,4-dioxane. Norm: normalized.

The absorption and emission peaks of BODIPY-phenyl molecule are 501 nm and 512 nm respectively, the measured spectra are in line with previous reports.[63] The absorption peak of the B2P is observed at 517 nm (Figure 5.2B), while that of the B2PI sample is observed at 532 nm. The observed bathochromic shift in the absorption spectra of B2PI is attributed to the incorporation of an iodine atom into the BODIPY-moiety.[256] The B2P exhibits an emission peak centered at 635 nm, while the B2PI exhibits an emission peak centered at 655 nm (Figure 5.2C). The excitation wavelength for both samples is 400 nm. The bathochromic shifts observed in emission spectra have previously been reported to be attributable to the iodine substitution.[108,246]

5.2.1 Steady State Upconversion in Solution

The steady-state upconversion emission measurements are performed in deaerated 1,4-dioxane. The samples were placed in 1 cm inert cuvettes and excited with a 532 nm laser diode as described in section 2.2.2. The sample containing B2PI (1 µM) and perylene (10 µM) is named as **BPI1-P10**; similarly, B2P (1 µM) and perylene (10 µM) is named as **BPI-P10**, the constituents of the samples and concentrations used for steady-state and time-resolved measurements are tabulated in the Table 5.1.

Figure 5.3 depicts the upconversion emission of B2P, B2PI (employed as a sensitizer), and perylene (employed as an annihilator). The spectral peaks observed at wavelengths 443 nm and 473 nm exhibit a resemblance to the characteristic fluorescence emission of perylene (see Figure 5.2C). The integrated upconversion

emission intensity of the **BPI1-P10** sample exhibits an 8.7-fold increase compared to that of the **BP1-P10** sample.

Table 5.1: The table presents nomenclature and constituents of samples used for the steady-state measurements.

Nomenclature	Constituent 1	Constituent 2	Solvent/ environment
BPI1-P10	B2PI - 1 μM	perylene - 10 μM	dioxane
BPI-P10	B2P - 1 μM	perylene - 10 μM	dioxane
LUV-BPI1-P10	B2PI - 1 μM	perylene - 10 μM	LUV
LUV-BPI1-P10	B2P - 1 μM	perylene - 10 μM	LUV

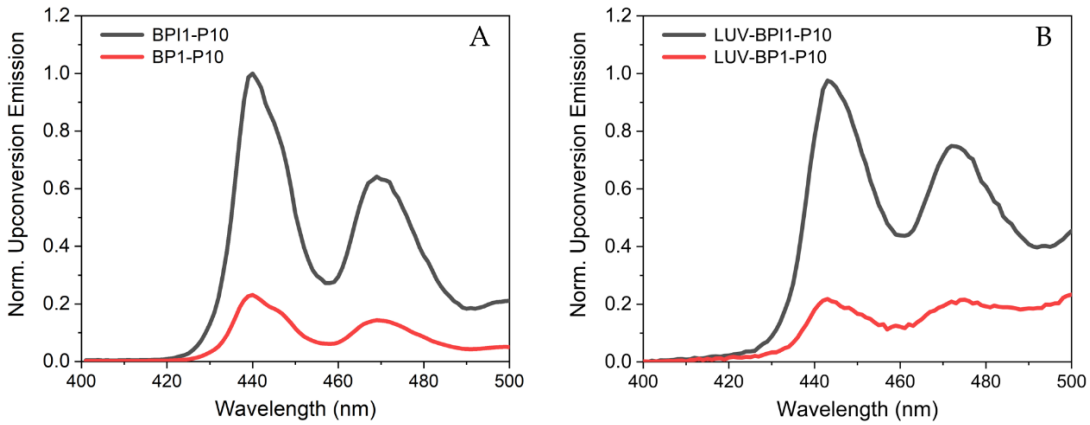

Figure 5.3: The normalized upconvesrsion emission spectra from (A) **BPI1-P10** and **BP1-P10** are measured in deaerated 1,4-dioxane (B) **LUV-BPI1-P10** and **LUV-BP1-P10** are measured in LUVs. Both measurements are carried out at an excitation wavelength of 532 nm. The normalization of the emission spectra are carried out with respect to the maximum of the emission peak (443 nm) from respective B2PI containing sample.

5.3 Femtosecond Transient Absorption Spectroscopy to Investigate Triplet Formation

To examine the photophysical mechanisms of charge separation and recombination mechanism to form triplet species, the femtosecond transient absorption (fs-TA) spectroscopy of B2P and B2PI in absence of perylene in 1,4-dioxane solvent is measured. The objective is to measure the timescale of charge separation and charge recombination processes occurring from sub-picoseconds to nanosecond timescales.

Figures 5.4A and 5.4B depict the fs-TA of B2P and B2PI, respectively. The negative differential absorbance signal observed for both samples within the wavelength range from 500 to 575 nm is attributed to the GSB of the BODIPY moiety. Additionally, the negative peaks observed below 450 nm are attributed to the GSB of the perylene moiety, as evidenced by its similarity to the inverted absorbance shown in green. Consistent with prior literature findings, absorption of the perylene-BODIPY cation-anion radical pair is observed at 575 nm.[233,251,254]

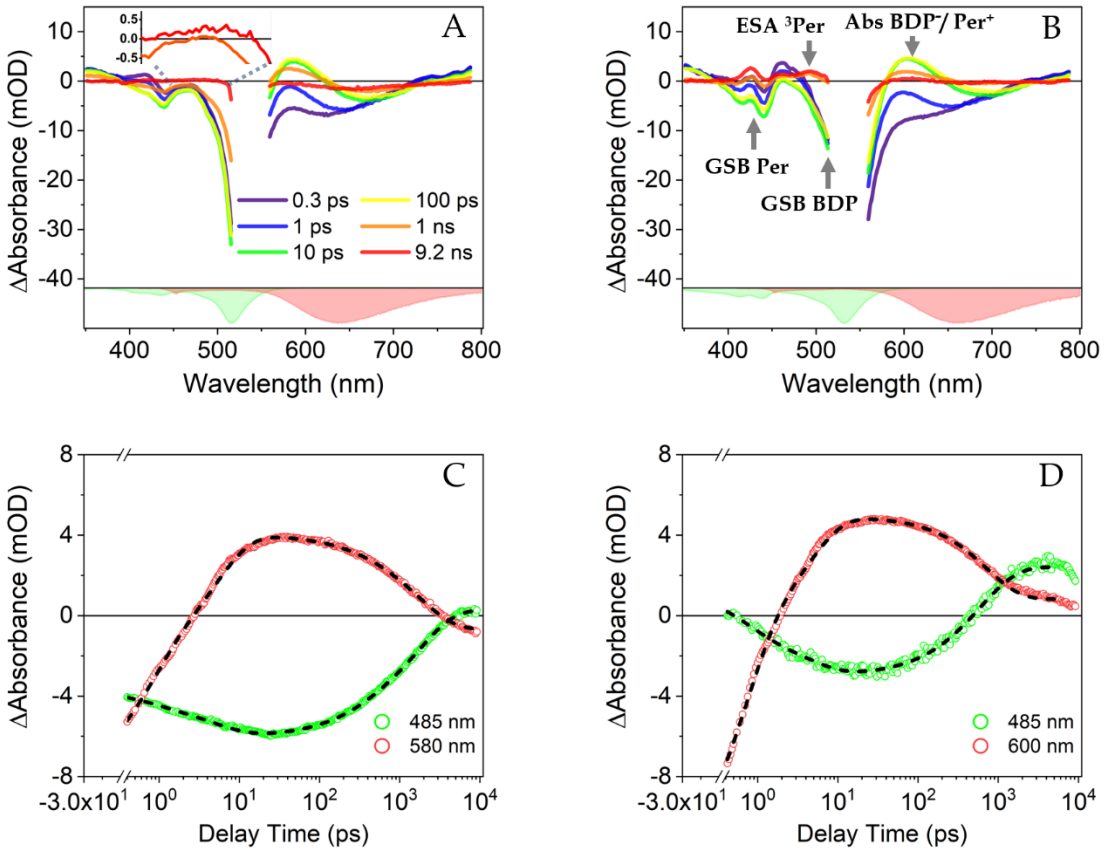

Figure 5.4: The femtosecond transient absorption spectra of B2P and B2PI are measured in 1,4-Dioxane. The inverted absorption spectra are represented in green, while the inverted emission spectra are represented in red for the corresponding samples. Both samples are excited at wavelength 532 nm. The legends are identical for A and B. The text refers to Per: perylene, BDP: BODIPY, ^{3}Per: perylene-centred triplet, Abs: absorbance. The kinetic traces of B2P and B2PI are presented in C and D respectively. The decay time constants are 0.6 ps, 5 ps, 273 ps, 1785 ps and an infinite component for B2P; and 0.6 ps, 4.5 ps, 288 ps, 662 ps and an infinite component for B2PI. The infinite component represents the decay of triplet species. The dashed black lines observed in B2P and B2PI are indicative of the fit to the corresponding kinetics. The error margin of the time constant falls within 10% of the given transient absorption value.

The emergence of GSB in both the BODIPY (*ca.* 500 nm) and perylene units (*ca.* 420

nm) and successive buildup of a positive differential absorbance at approximately 600 nm resulting from the formation of a charge-transfer state (^{1}CT). The simultaneous decay of ^{1}CT absorption band and increase in ESA of triplet species (perylene-centred triplet, *vide infra*) indicate the occurrence of triplet formation through charge recombination (see kinetic traces at 480nm and 580-600 nm, Figure 5.4C-D). These observations suggest the formation of triplet species through SOCT-ISC, which is consistent with the earlier observation by Wang *et al*. through time-resolved electron paramagnetic resonance (TREPR) spectroscopy.[233] The above-mentioned processes are formulated in Equations (5.1-5.5).

$$\text{BODIPY-Perylene} + h\nu\ (532\ \text{nm}) \rightarrow (^1\text{BODIPY-perylene})^* \qquad \text{Equation 5.1}$$

$$(^1\text{BODIPY-perylene})^* \rightarrow {}^1\text{CT}\ (\text{BODIPY}^{\circ-} + \text{perylene}^{\circ+}) \qquad \text{Equation 5.2}$$

$$^1\text{CT}\ (\text{BODIPY}^{\circ-} + \text{perylene}^{\circ+}) \rightarrow (^3\text{BODIPY})^* \qquad \text{Equation 5.3}$$

$$^1\text{CT}\ (\text{BODIPY}^{\circ-} + \text{perylene}^{\circ+}) \rightarrow (^3\text{perylene})^* \qquad \text{Equation 5.4}$$

$$^1\text{CT}\ (\text{BODIPY}^{\circ-} + \text{perylene}^{\circ+}) \rightarrow {}^3\text{CT}\ (\text{BODIPY}^{\circ-} + \text{perylene}^{\circ+}) \qquad \text{Equation 5.5}$$

The notation "BODIPY$^{\circ-}$" denotes the BODIPY anion, "perylene$^{\circ+}$" represents the perylene cation, while "*" represents the excited state of the associated molecule. The ^{3}BODIPY* refers to a BODIPY-centered triplet, while ^{3}perylene* denotes a perylene-centered triplet and ^{3}CT represents a triplet charge transfer state. Equations 5.3 and 5.4 represent SOCT-ISC; Equation 5.5 represents RP-ISC or any other pathway to form singlet charge transfer state to triplet charge transfer state,[247] the formation of ^{3}CT may occur through spin-orbit coupling as well, discusses later in the text.[257] Since the triplet formation is observed by charge recombination (*vide supra*), it is understood that the SOCT-ISC pathway remains the primary intersystem crossing (ISC) pathway. Three contributions to the triplet species are observed in the study, which may originate from BODIPY-centered, perylene-centered, and triplet charge transfer (^{3}CT) states, the

spectral range of each species is discussed in nanosecond transient absorption section.

The kinetics of the fs-TA data were analyzed through global fitting using the KiMoPack program.[258] Figures 5.4C and 5.4D display the kinetics from the GSB (485 nm) and absorption of ^{1}CT (580-600 nm) regions. The analysis reveals the presence of four distinct time constants and an additional infinite component for both the B2P and B2PI samples. Specifically, the B2P sample exhibits the time constants 0.6 ps, 5 ps, 273 ps, 1785 ps and an infinite component; while the B2PI sample exhibits time constants 0.6 ps, 4.5 ps, 288 ps, 662 ps and an infinite component. The values of τ_1 for both samples are identical. Additionally, the values of τ_2 and τ_3 for the two samples fall within their respective margin of error, indicating that the values of τ_2 for both samples are same, as well as the values of τ_3 for both the sample are same. There is a significant difference between the τ_4 values of the two samples.

The BODIPY-perylene dihedral angle exhibits 58° in the electronic ground state geometry (S_0) in both B2P and B2PI. However, in the first excited state (S_1), the dihedral angle is reduced to 41° (see Figure 5.5); the dihedral angles are obtained using TDDFT calculations. The relaxation from Franck-Condon geometry (S_0) to the relaxed S_1 geometry occurs within a timeframe of sub-picoseconds.[259] Hence, the fastest time constant τ_1 is assigned to the geometrical relaxation process. The absorption of ^{1}CT at approximately 600 nm experiences an increase up to *ca*. 20 ps, as illustrated in Figures 5.4C and 5.4D. This suggests a rise in the population of BODIPY$^-$ and perylene$^+$ species. Therefore, the time-constant of τ_2 is attributed to the buildup of the charge transfer state (^{1}CT). These time constants are in line with literature reports on BODIPY-dyads.[260]

The charge transfer band at *ca*. 580-600 nm is observed to decay beyond 20 ps for both B2P and B2PI. While, the GSB recovers and an ESA band emerges at wavelength 485 nm, which is assigned to the triplet state (the features of the triplet state is described in section 5.5.2). The concomitant decay of the charge transfer band at 580-600 nm and the emergence of the triplet ESA at 485 nm indicates the formation of (localized) triplet states through the process of charge recombination.[233] The GSB kinetics (485 nm) transitioning to the ESA of the triplet species at *ca*. 5 ns for B2P and *ca*. 1 ns for B2PI. This observation corroborates the faster formation of triplets in B2PI. Consequently, it is more likely that the time constant, denoted as τ_3, which exhibits identical values for B2P and B2PI, is not linked to intersystem crossing (ISC), but rather to charge recombination to the ground state (CR_S). Instead, ISC is associated with τ_4, which represents the timescale to form a triplet by charge recombination (CR_T). The results indicate that the rate of intersystem crossing (ISC) is 2.6 times higher in the B2PI

molecule containing iodine, thus signifying the role of the heavy atom in facilitating ISC. The kinetics of B2PI have been fitted up to a maximum of 6 ns due to the decay of its triplet state begins beyond this timeframe. However, it is not possible to accurately observe the decay time-constant of the triplet state using the dynamic range of the optical delay line used in the fs-TA experiments. The evolution of the triplet state of B2P persists up to 9.5 ns.[199,233,254,260]

5.4 Computational Simulations to Investigate Triplet Formation

The computational simulations are performed to calculate the energies of the singlet, triplet states and spin-orbit coupling strength between the singlet and triplet states. The computations were performed by Dr. Julien Guthmuller and Mr. Rengel Cane Sia from Gdańsk University of Technology, Poland. The details of the computational methods are given in section 2.5. The optimization of T_2 geometry was unsuccessful due to insufficient convergence; therefore, the energy levels of T_2 are not given.

5.4.1 Calculation of Spin-orbit Coupling and Energy of States

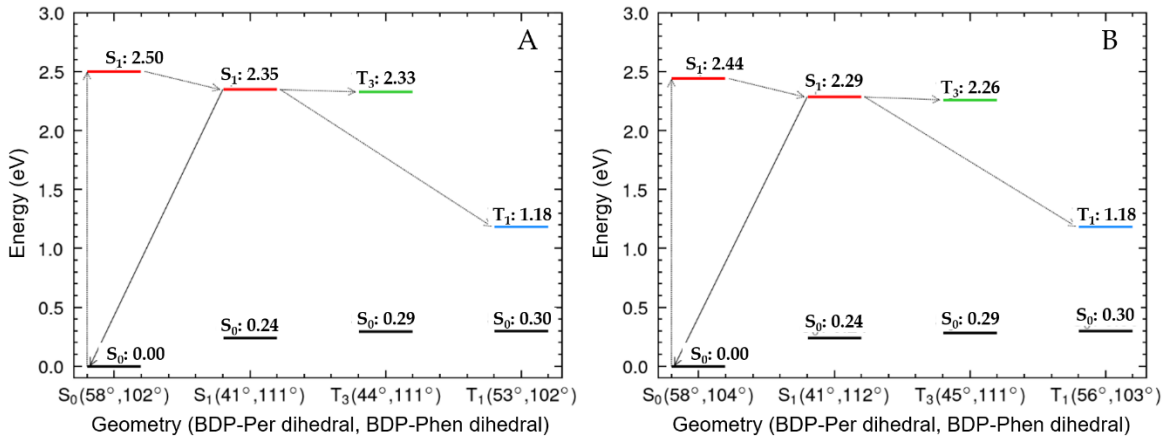

Figure 5.5: Dihedral angle and energies (eV) at S_0, S_1 (^{1}CT), T_3 and T_1 geometry (A) B2P (B) B2PI.

The strength of spin-orbit (SO) coupling is computed using Time-Dependent Density Functional Theory (TDDFT), see Table 5.2. The spin-orbit coupling between the charge transfer state (^{1}CT) and BODIPY-centered triplet (T_2) is 2.32 cm^{-1} for B2PI and 0.11 cm^{-1} for B2P. The spin-orbit coupling between ^{1}CT and perylene-centered triplet (T_1) is 0.59 cm^{-1} and 0.33 cm^{-1} for the B2PI and B2P, respectively; the computations support the notion of enhanced triplet formation in the iodinated-dyad. Figure 5.6 depicts the charge density difference for three lowest triplet states of B2PI, with T_3 being the

highest in energy followed by T_2 and T_1.

Table 5.2: The spin-orbit coupling (cm^{-1}) between $S_1(^1CT)$ and T_n geometries.

	$^1CT \rightarrow T_1$	$^1CT \rightarrow T_2$	$^1CT \rightarrow T_3$
B2P	0.33	0.11	0.40
B2PI	0.59	2.32	3.38

The spin-orbit coupling (SOC) for the $^1CT \rightarrow {}^3CT$ (*i.e.* T_3) state is similar to that of $^1CT \rightarrow T_2$ (BODIPY-centered state). In addition, it can be observed that the SOC for the triplet charge transfer state (^3CT) is enhanced in B2PI. For instance, the SOC values of 0.40 cm^{-1} and 3.38 cm^{-1} are determined at the ^1CT geometry for B2P and B2PI, respectively. This observation suggests the potential emergence of the ^3CT species through ISC from the ^1CT state.

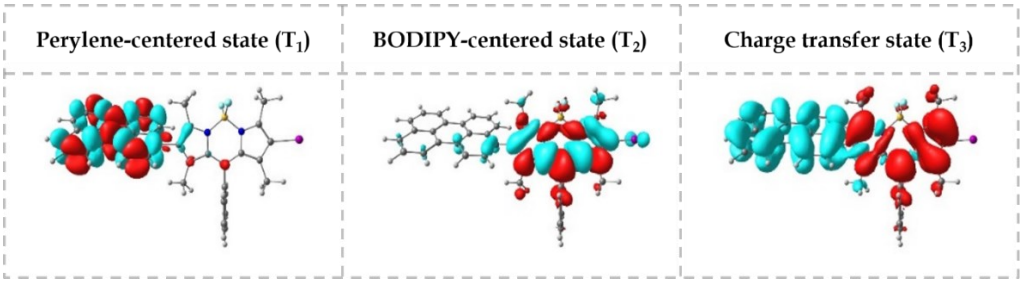

Figure 5.6: Iso-surfaces of Charge Density Difference for T_3, T_2 and T_1 states of B2PI. Electrons and holes are indicated in red and blur color respectively.

The presence of ^3CT species is also observed by the ns-TA analysis, described in the subsequent section (see Figure 5.10). The recombination of charge leads to the formation of BODIPY-centered triplet and perylene-centered triplet through SOCT-ISC (see Equations 5.3 and 5.4).[247,251] However, the transition from ^1CT to ^3CT does not take place via SOCT-ISC, but rather through radical pair intersystem crossing (RP-ISC). However, the RP-ISC process is not preferred for compact dyads such as BODIPY-perylene, where the two moieties are separated by a single bond and have an intramolecular distance of *ca.* 8 Å.[247,261] In contrast, RP-ISC occurs when the electron donor and acceptor moieties are separated by a bridge. The J value, a parameter that characterizes the energy gap between singlet and triplet states, serves as an indicator of the potential for RP-ISC. The computations have yielded J values exceeding 36 cm^{-1} for both B2P and B2PI (see the next section 5.4.2). However, for RP-ISC to occur

favorably, the J value must not exceed 0.1 cm^{-1}.[247,261] Based on this criterion, it is understood that RP-ISC is improbable. The overlap of donor and acceptor orbitals leads to different wavefunctions and energy for ^{1}CT and ^{3}CT states; this resulting in non-zero spin-orbit coupling, the non-zero spin-orbit coupling induces the $^1CT \rightarrow {}^3CT$ transition. Wang *et al*. reported a similar situation in their study, wherein the electron spin polarization obtained through time-resolved electron paramagnetic resonance spectroscopy (TREPR) revealed that SOCT-ISC was the primary intersystem crossing channel, while a minor contribution of ^{3}CT was observed. This observation was correlated to RP-ISC for compact BODIPY-anthracene dyads.[247] However, the current scenario involves a transition from ^{1}CT to ^{3}CT, which is facilitated by spin-orbit coupling.

5.4.2 Calculation of J Value

The J value as described above relates the energy difference between singlet and triplet states, given in Table 5.3 below.

Table 5.3: Singlet-triplet energy splitting and J value between S_1 and T_3 states

	S_1 (eV)	T_3 (eV)	ΔE_{ST} (eV) = 2 | J |	| J | (cm^{-1})
B2P	2.3496	2.3407	0.0089	36
B2PI	2.2793	2.2660	0.0132	54

5.5 Nanosecond Transient Absorption Spectroscopy

Nanosecond transient absorption study is performed on BODIPY-phenyl, B2P, B2PI samples with and without perylene to recognize the triplet species and to investigate energy transfer mechanisms of TTAUC process. The BODIPY-phenyl and perylene are examined first to recognize the triplet states of pristine BODIPY and pristine perylene molecules, followed by B2P and B2PI are investigated.

5.5.1 Nanosecond Transient Absorption Spectroscopy of BODIPY-phenyl and Perylene

The BODIPY-phenyl molecule exhibits poor intersystem crossing (ISC) yield.[108,199,238,239] The triplet ESA of BODIPY-phenyl is observed to be within the spectral region of 370-460 nm (see, Figure 5.7A).[33] Upon the addition of perylene to the BODIPY-phenyl solution and subsequent excitation at wavelength 510 nm results in the build-up of triplet ESA of perylene by TTET process.[33] The ESA of perylene is broad and observable in the visible region, as depicted in Figure 5.7B.

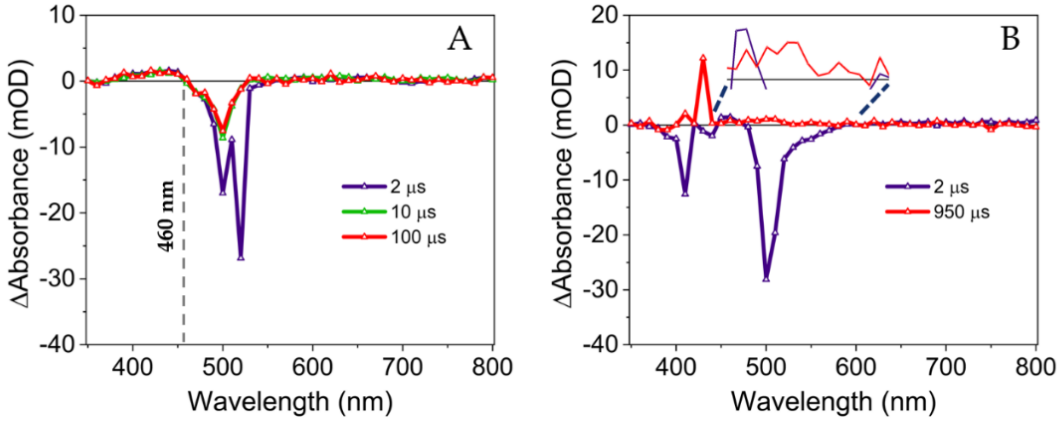

Figure 5.7: Nanosecond transient absorption spectra of (A) BODIPY-phenyl 20 µM (B) BODIPY-phenyl 20 µM and perylene 50 µM. Solvent-1,4-dioxane. The excitation wavelength used in the experiment was 510 nm. The excitation energy was 0.5 mJ.

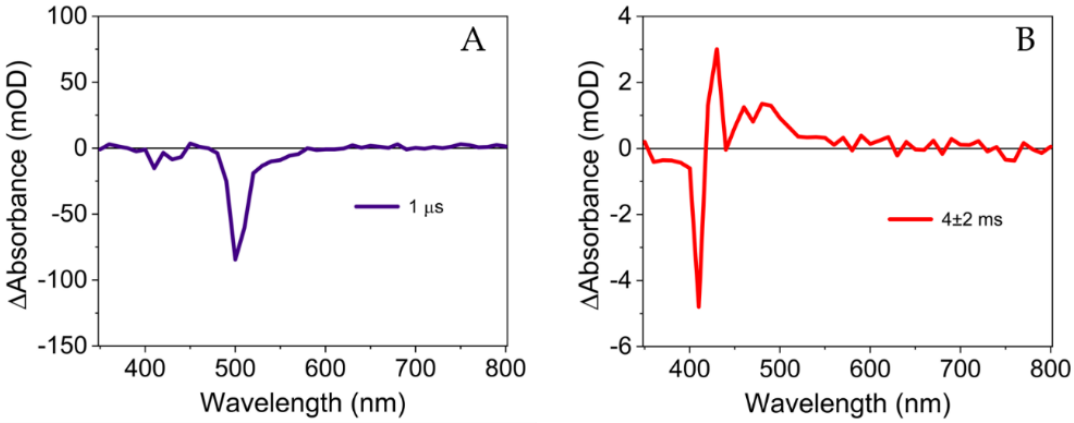

Figure 5.8: DAS of BODIPY-phenyl 20 µM with perylene 50 µM obtained through global fitting. The corresponding spectra are depicted in the Figure 5.7. Spectra shown in (A) and (B) are two distinct components of the global fit, with respective time constants of τ_1 = 1.0±0.3 µs and τ_2 = 4±2 ms respectively.

The global fit of the spectra shown in the Figure 5.7B reveals biexponential decay with

time-constants 1.0±0.3 μs and 4.0±2 ms. The decay associated spectra (DAS) of the fit is shown in Figure 5.8. The fast time-constant (1.0±0.3 μs) is assigned to the decay of the triplet BODIPY and the slow time-constant (4±2 ms) is assigned to the decay of the triplet perylene. The time-constants are in match with the literature reports.[33] The characteristics of DAS in Figure 5.8A exhibit similarities with those of BODIPY and perylene GSB, as depicted in Figure 5.7A. The characteristics of DAS shown in Figure 5.8B matches with the ESA of perylene.[33]

The triplet features of BODIPY-phenyl molecule with and without the perylene are useful to recognize the features of B2P and B2PI dyad molecules; since the dyads are formed by the linkage of BODIPY-phenyl and perylene molecules. In the next section, nanosecond transient absorption spectra of B2P and B2PI with and without perylene are described.

5.5.2 Investigation of TTAUC mechanism in Solution

The nanosecond transient absorption (ns-TA) studies were performed on B2P and B2PI in 1,4-dioxane solution, both in the presence and absence of additional perylene to investigate the energy transfer mechanism in TTAUC. The concentration of both sensitizer molecules (B2P and B2PI) used in the steady state upconversion emission measurements was 1 μM. However, the signal-to-noise ratio in ns-TA for the sample containing B2P (1 μM) was found to be poor. Therefore, the concentration of 5 μM for both B2P and B2PI, along with 50 μM of perylene was chosen for the time-resolved upconversion study.

Figures 5.9A and 5.9B depict the ns-TA spectra of B2P in absence and presence of external perylene, respectively. The spectra between 515 and 560 nm are dominated by GSB in both spectra. The ESA is dominant throughout the visible spectrum, with the exception of the dominant GSB region. The ESA features in B2P (as depicted in the Figure 5.9A) within the wavelength range 460 to 515 nm resemble to the ESA of the perylene triplet state (as depicted in the Figure 5.8B).[33] The ESA visible in the spectral region from 560 to 800 nm is attributed to the combined ESA of BODIPY and perylene triplet states.[262] The addition of perylene (50 μM) to the solution containing B2P (5 μM), increases the intensity of the differential absorption signal at 425 nm and 455 nm (see arrows in the Figure 5.9B). These changes in the spectral signatures arise from the transfer of energy from triplet sensitizers (5 μM) to additional external perylene (50 μM) molecules by TTET.[33,254]

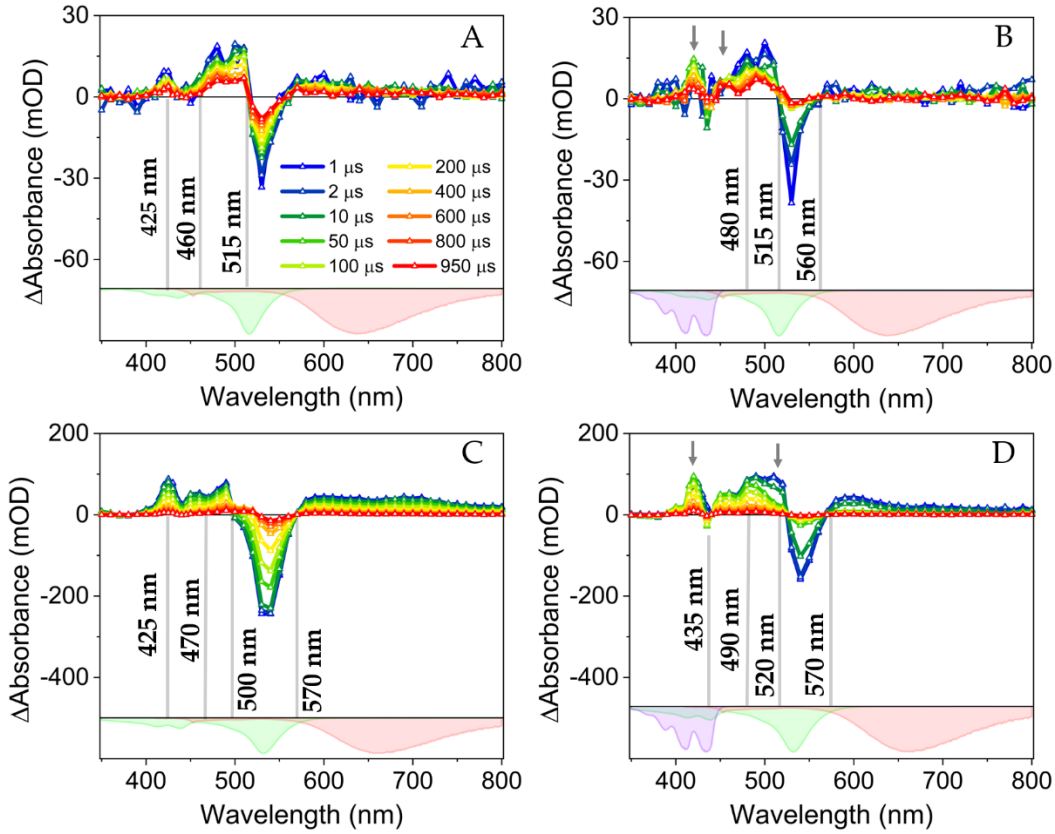

Figure 5.9: Nanosecond transient absorption spectra of: (A) B2P 5 µM (B) B2P 5 µM with perylene 50 µM (c) B2PI 5 µM and (d) B2PI 5 µM with perylene 50 µM. The absorbance (inverted) of the sensitizer is represented in green and emission (inverted) is depicted in red at the bottom. Additionally, the absorbance (inverted) of perylene is illustrated in violet in corresponding samples. The legend remains consistent across all figures. The changes in the spectra of (B) and (D) due to the addition of perylene are indicated by arrows in relation to (A) and (C) respectively. The wavelength of excitation is 532 nm.

Figures 5.9C and 5.9D depict the ns-TA spectra of B2PI in absence and presence of external perylene, respectively. Dominant GSB is visible within the 500-570 nm region, as depicted in Figure 5.9C; other than the GSB region, ESA is dominant everywhere between 350 and 800 nm with two peaks at 425 nm and 490 nm. The addition of 50 µM perylene (as shown in Figure 5.9D) results in an increase of the ESA at 425 nm, as well as within the range 490 nm to 520 nm (see arrows).

The comparison of Figures 5.9A and 5.9C reveals a red-shift of GSB by *ca.* 10 nm in B2PI, which is consistent with the bathochromic shift observed in the steady-state absorption spectra. The intensity of ESA (of triplet species) is significantly higher in B2PI as compared to B2P under identical experimental conditions; this is attributed to the formation of higher number of triplet species in B2PI facilitated by the presence of iodine. For instance, at 480 nm and 1 µs, the ESA of B2P and B2PI are 14 mOD and 58

mOD, respectively. Moreover, it can be observed from Figures 5.9A and 5.9B that, the addition of perylene does not result in an increase in the ESA between 490-520 nm for B2P. Conversely, for the B2PI sample, the addition of perylene leads to a substantial rise in the ESA within the same wavelength range (490-520 nm, see arrows in Figures 5.9C and 5.9D). The observed increase in the ESA is attributed to the transfer of energy from triplet sensitizer to the externally added perylene, resulting in an increase in the population of triplet perylene.

The absence of complete orthogonality between the BODIPY-perylene moieties in the dyad pair (as depicted in Figure 5.5) results in a significant overlap of orbitals between the BODIPY and perylene moieties. Consequently, it is anticipated that the triplet states will exhibit common characteristics of both BODIPY and perylene. The global fitting[258] of the kinetics of B2PI at concentrations of 1 µM and 5 µM reveals three distinct species with distinct characteristic lifetimes, as depicted in Figure 5.10. Given that the BODIPY triplet ESA signature is observed at wavelengths below 460 nm (see, Figure 5.7A), the DAS associated with τ_2 is attributed to the decay of BODIPY-centered (T_2) triplet state; the ESA of this spectra is observable until *ca*. 460 nm. (see Figure 5.10).[33] The DAS associated with τ_1 is assigned to the decay of perylene-centered (T_1) state; the ESA of this spectra extends up to *ca*. 540 nm, which resembles the ESA of triplet perylene (see Figure 5.7B).[33] The DAS associated with τ_3 is assigned to the decay time-constant of triplet charge transfer state (^{3}CT).

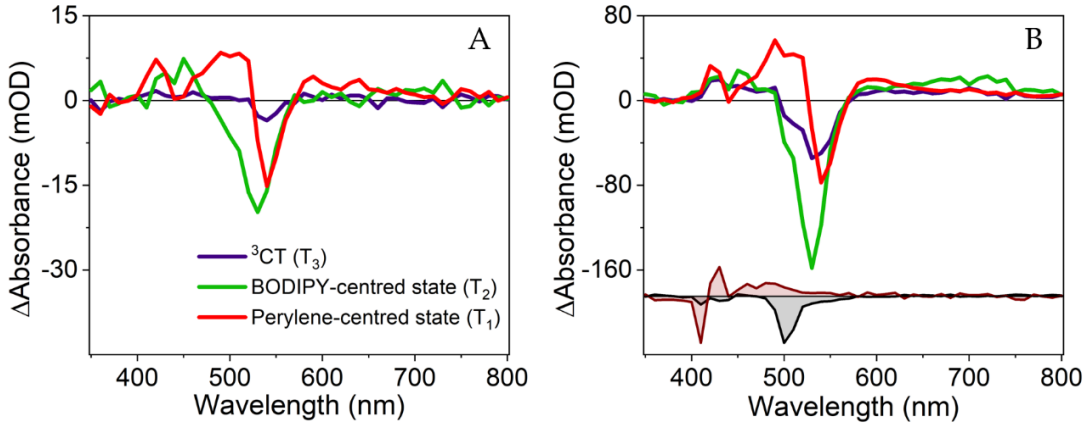

Figure 5.10: The decay-associated spectra (DAS) of the global fit of the kinetics of (A) B2PI 1 µM: ^{3}CT- triplet charge transfer state (T_3), τ_3 = 60±6 µs; BODIPY-centred state (T_2), τ_2 = 526±50 µs; and perylene-centred state (T_1), τ_1 = 1500±150 µs. (B) B2PI 5 µM, with lifetimes of τ_3 = 66±7 µs, τ_2 = 155±15 µs, and τ_1 = 560±50 µs. The DAS of BODIPY-phenyl 20 µM and perylene 50 µM are shown at the bottom in B (see Figure 5.8). The legends are identical for both figures.

Upon increasing the B2PI concentration (as depicted in Figure 5.10) from 1 µM to 5

μM, a reduction in the decay time-constant of the BODIPY-centered triplet (T_2) state from 525 μs to 155 μs is observed, this phenomenon is attributed to triplet-triplet annihilation (TTA) between T_2 states; similarly, the lifetime of the perylene-centered triplet (T_1) state reduces from 1.5 ms to 560 μs, which is associated with the TTA between T_1 states. Upon decreasing the concentration of B2PI to 0.25 μM, the signal-to-noise ratio was poor and a satisfactory fit could not be achieved. Therefore, the lifetimes 60 μs, 525 μs and 1.5 ms, which are obtained from 1 μM concentration are considered as intrinsic lifetimes of the three states: ^{3}CT, BODIPY-centered, and perylene-centered with negligible contribution from TTA. Lifetimes are tabulated in Table 5.4. The spectral shift observed in the GSB of BODIPY-phenyl (shown at the bottom of the Figure 5.10B) with respect to B2PI is due to the iodination of BODIPY-moiety, as explained in the steady state section of this chapter.[256]

Table 5.4: The table presents samples used for ns-TA measurements. The obtained lifetimes are determined through nanosecond transient absorption spectroscopy. The error in the lifetimes of B2PI samples is within 10%, while for B2P samples is within 20% of the given value.

Constituent 1	Constituent 2	Solvent/ environment	τ_1 (μs)	τ_2 (μs)	τ_3 (μs)
B2PI - 1 μM		LUV	60	315	1500
B2PI - 1 μM	perylene - 10 μM	LUV	10	115	850
B2PI - 1 μM	-	dioxane	60	525	1500
B2PI - 5 μM	-	dioxane	66	155	560
B2P - 5 μM	-	dioxane	80	900	2500
B2PI - 5 μM	perylene - 50 μM	dioxane	17	107	512
B2P - 5 μM	perylene - 50 μM	dioxane	18	812	2000

The kinetics of the B2P molecule exhibit three components with time-constants of 80 μs, 900 μs and 2.5 ms, which correspond to the decay time-constants of ^{3}CT, BODIPY-centered, and perylene-centered states respectively. However, the signal-to-noise ratio is poor due to lower triplet ESA, resulting in a large error margin of 20% for the lifetime values. The observed lifetimes of B2P and B2PI are higher than the corresponding iodo-BODIPY triplet lifetime (τ = 62 μs).[233,263] A fair signal is observed for the B2P sample at 12 μM concentration (shown in Figure 5.11).

The addition of external perylene into the solution of B2P and B2PI results in TTET

from sensitizer to annihilator molecules, which leads to reduction in the lifetime of the sensitizer triplet state.[10] For example, upon addition of 50 μM perylene to 5 μM B2PI, the observed lifetimes of the sample are 11 μs, 107 μs, and 512 μs (see Table 5.4). These lifetimes correspond to the quenched lifetimes of the decay of ^{3}CT (11 μs), BODIPY-centered triplet (107 μs), and perylene-centered triplet (512 μs). The triplet lifetimes of the B2P samples are also quenched upon the addition of perylene due to TTET, values are given in Table 5.4.

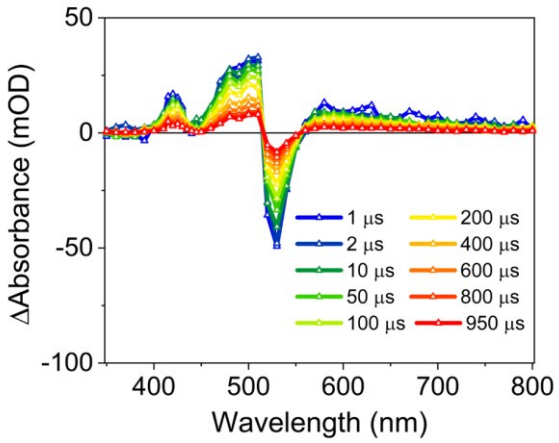

Figure 5.11: Nanosecond transient absorption spectra of B2P - 12 μM

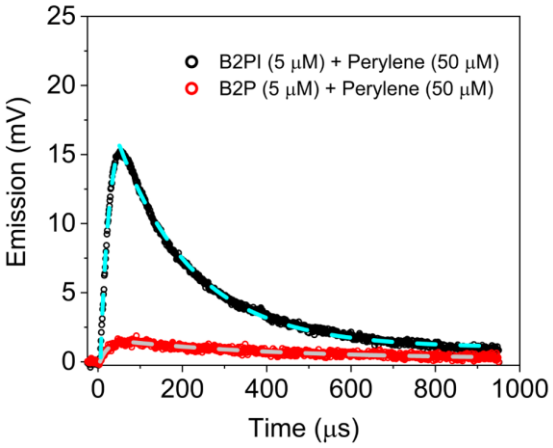

Figure 5.12: Time-resolved upconversion emission from B2P 5 μM and B2PI 5 μM with perylene 50 μM. The emission was measured at 470 nm with excitation at 532 nm. The dashed lines represent the fit to the exponential decay curve. The B2P sample exhibits τ_{inc} = 20 μs and τ_{dec} = 390 μs. The B2PI sample exhibits τ_{inc} = 20 μs and τ_{dec} = 180 μs. Reduced chi square (χ^2) < 10^{-7}.

The time-resolved emission kinetics of B2P and B2PI samples with perylene at 470 nm are shown in Figure 5.12. The growing part of the emission curve represents the population growth of the triplet perylene species through TTET, while the decaying

segment of the curve represents the decay of perylene triplets through TTA.[235,247,264] The decay time for the B2P sample is longer than the B2PI sample, which indicates slow TTA between triplet perylene molecules. The TTA time depends upon the relative distance between two triplet perylene molecules,[94] the B2PI sample will generate larger number of triplet perylene species (with respect to B2P) due to presence of a larger number of sensitizer molecules through ISC; therefore, relatively smaller distance between two triplet perylene molecules leads to faster TTA process; whereas, the B2P sample has relatively slow TTA.

5.5.3 Investigation of the TTAUC mechanism in Lipid Bilayer Membrane

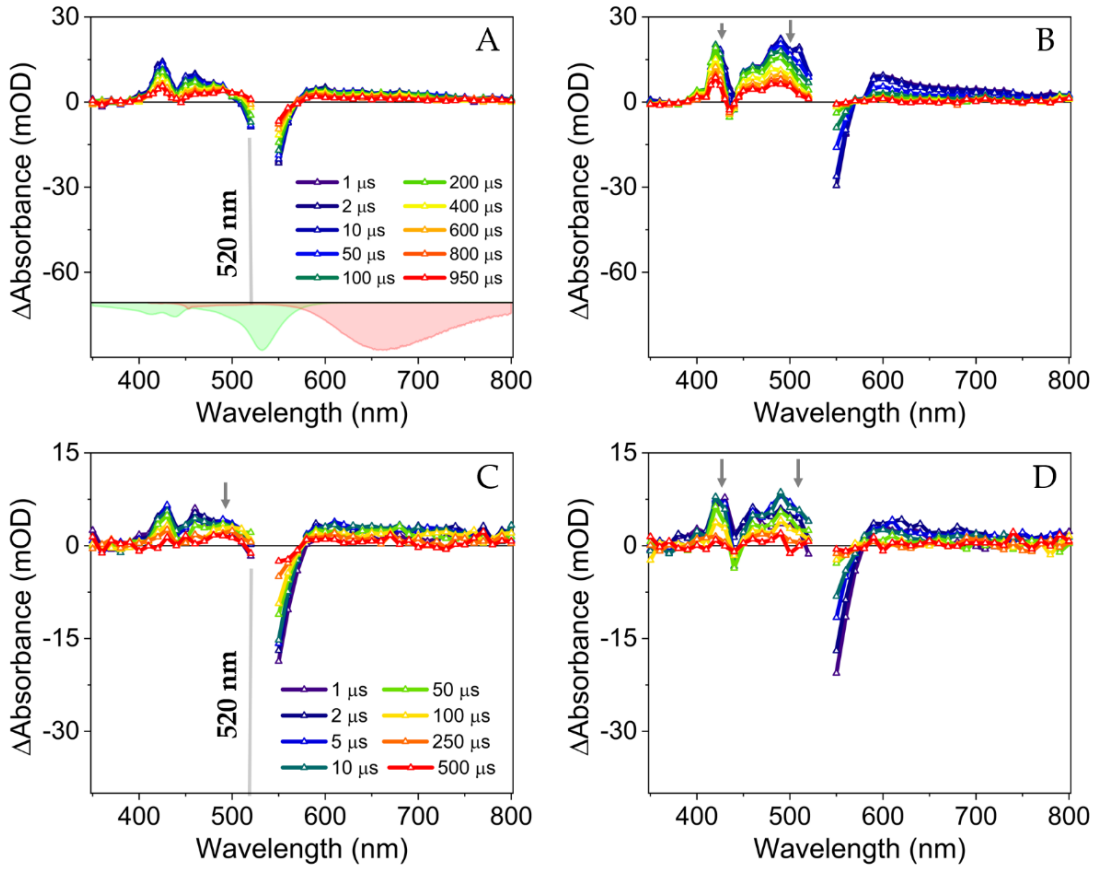

Figure 5.13: Nanosecond transient absorption spectra of (A) B2PI 1 µM in dioxane (B) B2PI 1 µM & perylene 10 µM in dioxane (C) B2PI 1 µM in LUV (D) B2PI 1 µM & perylene 10 µM in LUV. The spectra in pump wavelength region 530-540 nm are removed due to high scattering in LUV samples. LUV is made of 5 mM DOPC lipid. In the bottom: absorbance spectra of B2PI (inverted) in green, emission spectra (inverted) of B2PI in red.

The ns-TA spectra of B2PI with and without perylene in large unilamellar vesicles (LUVs) are depicted in Figures 5.13C and 5.13D respectively, the difference absorption

signal (ΔAbsorbance) features exhibit similarities to the corresponding spectra observed in solution (Figures 5.13A and 5.13B).

However, a careful analysis indicates significant differences as illustrated by arrows. The dominant ESA feature near 510 nm observed in the B2PI-LUV sample appears as dominant GSB feature in solution. It may arise from the fact that the hydrophobic B2PI molecules are strongly confined within the 2-dimensional lipid bilayer membrane, resulting in a significantly higher local concentration of B2PI molecules within the lipid bilayer *i.e.* exceeding 1 μM. The increased concentration of the molecule in a confined space enhances the likelihood of a collision, thereby increasing the probability of TTET from BODIPY-centered triplet (T_2) to a ground state molecule; therefore, forming perylene-centered triplets (T_1). Consequently, a large population of perylene-centered triplet species is generated through TTET mechanisms, which is an addition to perylene-centered triplet species formed through SOCT-ISC, as discussed in section 5.3. Consequently, the ESA feature in the vicinity of 500 nm, which originates from the absorption of perylene-centered triplet species, appears higher in the B2PI-LUV sample.

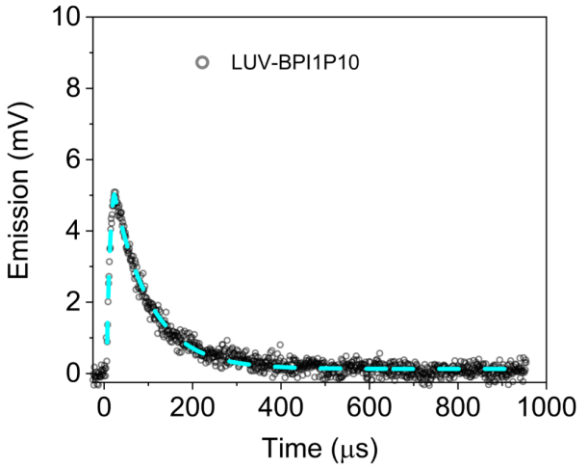

Figure 5.14: Time-resolved upconversion emission from **LUV-BPI1P10**: B2PI 1 μM and perylene 10 μM in LUV. The emission was measured at 470 nm with excitation at 532 nm. The dashed lines represent the fitting to the exponential decay curve. The exponential fit reveals τ_{inc} = 8 μs and τ_{dec} = 80 μs. Reduced chi-square (χ^2) < 10^{-7}.

Similarly, the addition of external perylene (annihilator) to B2PI samples results in the occurrence of TTET from sensitizer to perylene molecules. This leads to increased ESA associated with perylene in the vicinity of 500 nm, as depicted in Figures 5.13B and 5.13D. The increased concentration of molecules in a confined region promotes self-quenching; therefore, the lifetime of the BODIPY-centered triplets in the lipid bilayer is comparatively shorter than that in the solution (see Table 5.4). This observation

indicates that, despite higher viscosity of the DOPC lipid bilayer (η = 6.4±1.2 cP, see section 4.4.3) with respect to dioxane (η = 1.3 cP at 293 K),[265] the sensitizer and annihilator molecules can diffuse effectively in the lipid bilayer and participate in energy transfer processes (TTET and TTA).

The measurement of ns-TA of B2P molecules in lipid bilayer was not successful at 1 µM concentration due to poor signal-to-noise ratio, increasing the concentration resulted in molecules floating out of the lipid bilayer; therefore, not opted for investigation in this thesis.

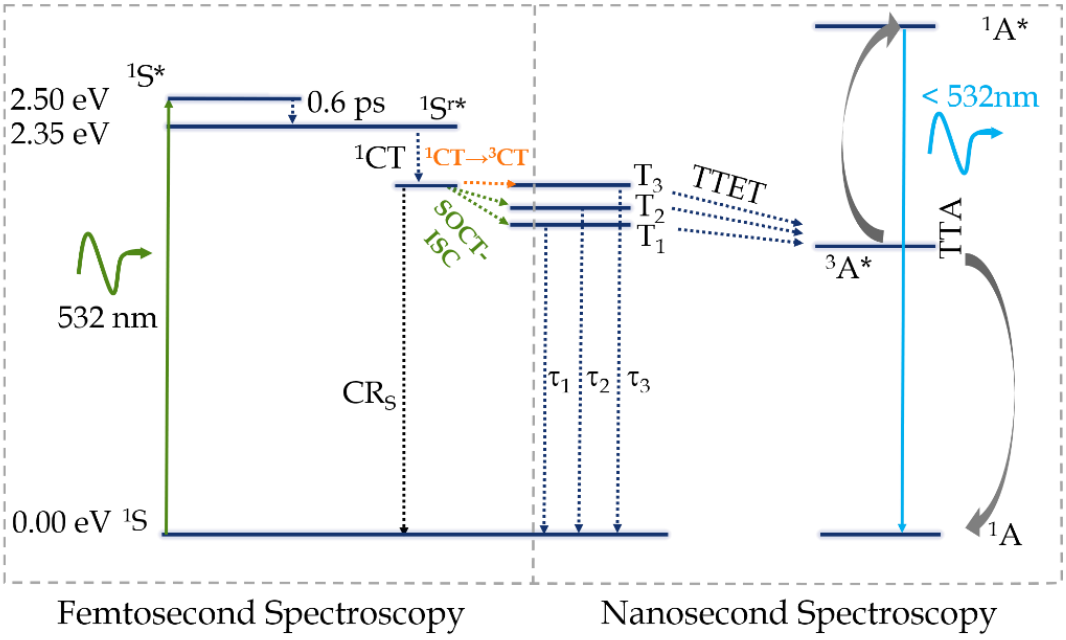

Figure 5.15: The model depicts the processes following absorption of 532 nm photon by a B2P or B2PI molecule and subsequent emission of an anti-Stokes shifted blue photon. The ISC time-constants for B2PI and B2P as determined by SOCT-ISC are 662 ps and 1785 ps respectively. The order of energy levels of the triplet states are $T_3 > T_2 > T_1$, where T_3 refers to the triplet charge transfer state, T_2 refers to the BODIPY-centred triplet and T_1 refers to the perylene-centered triplet state. The energy levels are illustrated in Figure 5.5. Additionally, Table 5.4 provides information on the decay time-constants. The ^{1}S* and ^{1}Sr* refer to the locally excited state and locally relaxed excited state respectively, while CR_S denotes the charge recombination to the ground state.

The time-resolved emission from LUVs consisting B2PI (1 µM) and perylene (10 µM) is shown in Figure 5.14. Similar to solution measurements, the growing part of the curve indicates the population growth of triplet species through TTET and the decaying part of the curve depicts decay of perylene triplets by TTA. The growing time-constants of the LUV sample is 8 µs; whereas, five times higher concentration of sensitizer and annihilator (B2PI 5 µM and perylene 50 µM, Figure 5.12) in dioxane shows growing time-constants of 20 µs, *i.e.* faster TTET in LUV sample. Similarly,

decaying time-constants of LUV and dioxane samples are 80 μs and 180 μs, respectively; *i.e.* faster TTA in the LUV sample. Despite higher viscosity of the DOPC lipid bilayer membrane, localized high concentration and long triplet lifetime of sensitizer and annihilator molecules enables efficient TTET (sensitizer to annihilator) and TTA (between triplet perylenes) processes. Previous studies have reported very high bimolecular energy transfer rates in polymer networks featuring confined pairs of sensitizer and annihilator;[33,34] TTA rate is observed to be higher in the polymeric system investigated in Chapter 3 as well. The spectroscopic investigation performed by fs-TA and ns-TA are summarized in Figure 5.15.

6. Summary

Triplet-triplet annihilation upconversion (TTAUC) is gaining prominence in the field of optical spectroscopy and holds the potential to revolutionize various emerging technologies such as solar cells, bioimaging and light-activated drug release. This is attributed to its capability of converting long-wavelength photons to higher energy photons, even at low excitation power densities (~5 mW cm^{-2}). A large spectrum of solar radiation is beyond the absorption window of photovoltaics, the implementation of TTAUC system in solar cells can upconvert this part of solar radiation to the absorption window of the photovoltaics and thereby increasing the energy conversion efficiency. Similarly, the low excitation power density can activate the drug release without damaging the tissue by excitation radiation.

The implementation of TTAUC in solar cells or light-activated drug release necessitates the transfer of the upconversion system comprising sensitizer and annihilator, from solution to solid phase. However, TTAUC is most efficient in solutions and needs inert conditions. The challenge lies in the fact that diffusion plays a crucial role in molecular processes for triplet-triplet energy transfer (TTET) and triplet-triplet annihilation (TTA). In this context, tremendous efforts have been made by the scientific community; such as, to perform the TTAUC in solid state media, several methodologies have been developed to effectively incorporate both sensitizer and annihilator into polymers, or to combine a macromolecular annihilator with monomeric sensitizers. For drug delivery application, liposomes reconstituted with sensitizer, annihilator and drug molecules have been synthesized. The red to blue light upconversion from liposomes has enabled the drug release. Despite these advancements, the technology is still in the development phase.

This thesis work fills selected gaps in the advancement of these promising applications. It is divided into three parts. In the context of solid-state application of TTAUC, macromolecule sensitizer (sensitizer molecules linked to polymer chain) has been investigated with monomeric annihilator as a TTAUC system, this scientific objective has been achieved in Chapter 3. In the context of light-activated drug release, two scientific problems have been addressed. First, the viscosity of the medium, which plays a crucial role in the diffusion of molecules and affects the crucial TTET and TTA process has been obtained using time-resolved anisotropy methods in Chapter 4. Second, triplet state lifetime of sensitizer and annihilator, which plays a vital role in determining the efficiency of energy transfer processes has been investigated in the lipid bilayer medium in Chapter 5. These studies are vital to optimize a TTAUC

process in the lipid bilayer system. These scientific objectives have been investigated using steady-state, time-resolved spectroscopy and computational simulation methods.

In Chapter 3, ester decorated Ru(2,2-bipyridine)$_2$ molecular sensitizer has been polymerized into the side chains of a poly methyl methacrylate (PMMA) polymer. The polymerized sensitizer serves as a macromolecular photosensitizer and is co-dissolved with 9,10-diphenylanthracene as an annihilator.

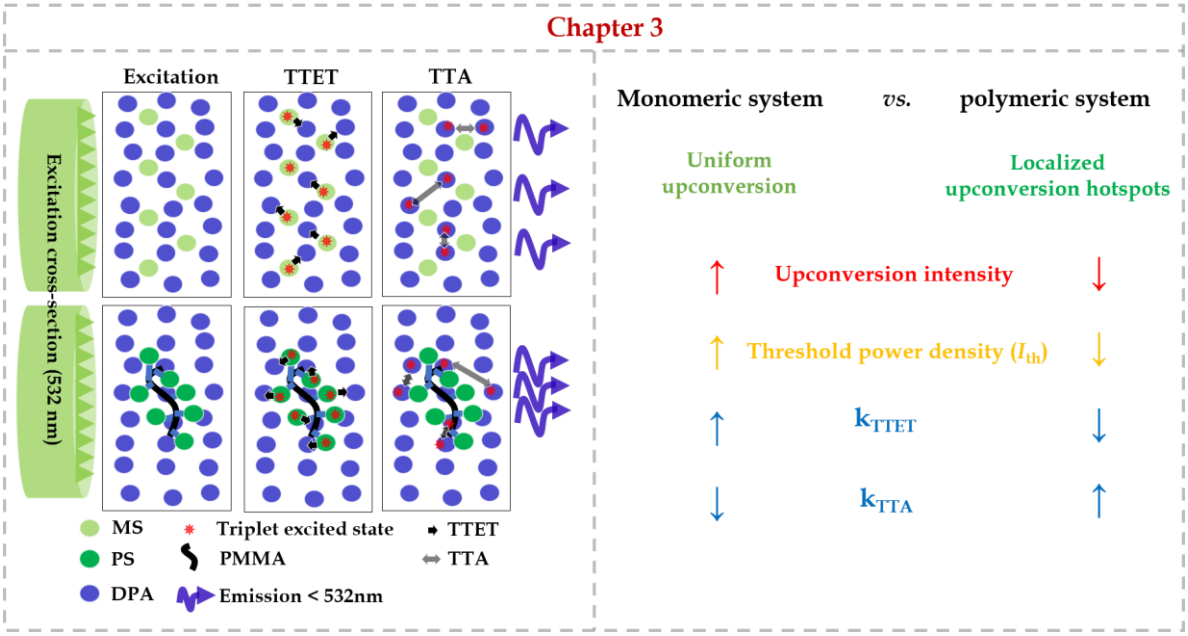

Figure 6.1: Graphical summary of Chapter 3. Left: Representation of upconversion emission from monomeric and polymeric sensitizers with monomeric annihilators. Right: the characteristics of the upconversion systems. Upward and downward arrows represent higher and lower values with respect to each other.

The study demonstrates that the macromolecular sensitizer and monomeric annihilator can produce upconversion photons at very low excitation power densities (6 mW cm^{-2}). Although, the upconversion intensity remains lower than that of the monomeric counterparts; the threshold power density (I_{th}) where upconversion system achieves its 50% efficiency is lower in the case of polymeric systems. The polymeric sensitizer, which is much larger than the monomeric sensitizer shows 1.6 times lower TTET rate due to slow diffusion of larger size; but produces localized triplet annihilators for TTA process, which results in 2.2 times higher TTA rate than monomeric counterpart, high TTA rate is also responsible for low I_{th} in polymeric systems. The low I_{th} observation made in the polymeric system shows the effectiveness of the system at low excitation power density. This is useful in designing TTAUC system for application in solar cells to harness solar radiation of longer

wavelengths. The summary of Chapter 3 is illustrated in Figure 6.1.

In Chapter 4, rotational diffusion of BODIPY-derivative (BODIPY-Ar-chol) is investigated in dichloromethane (DCM) and 1,2-Dioleoyl-sn-glycero-3-phosphocholine (DOPC) made giant unilamellar vesicles (GUVs) using polarization resolved confocal microscopy, time-resolved emission anisotropy and transient absorption anisotropy. The polarization resolved confocal microscopy of a GUV at the equatorial plane reveals the placement of the BODIPY-moiety in close proximity to the polar headgroups of the lipids, while the cholesterol-moiety is situated along the acyl-chain of the lipids within the membrane.

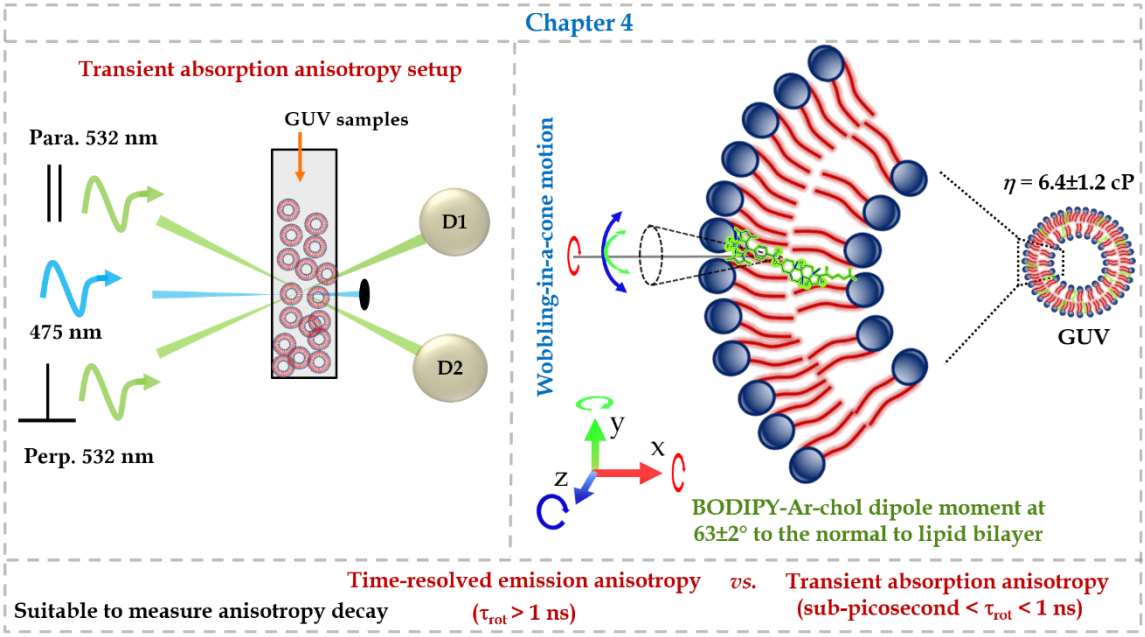

Figure 6.2: Graphical summary of the Chapter 4. Left: transient absorption anisotropy measurement setup for BODIPY-Ar-chol in DCM and GUVs. Right: orientation of the BODIPY-Ar-chol molecule and its rotation in a GUV. Para: parallel to pump polarization; Perp: perpendicular to pump polarization. D1 and D2 are two detectors employed to measure the transmitted light. τ_{rot}: rotational relaxation times.

Transient absorption anisotropy (TAA) does not rely on the emission of the chromophore to measure the rotational relaxation times and possesses higher resolution than time-resolved emission anisotropy (TEA). The spheroid shape of the BODIPY-Ar-chol results in tri-exponential decay of anisotropy in DCM; whereas, rigid embedment in GUVs leads to biexponential decay to anisotropy. The microviscosity is estimated to be 6.4±1.2° cP. The observations made using transient absorption anisotropy (TAA) measurements are crucial in determining the true rotational dynamics of a molecule. Most of the molecules in applications are of non-spherical shapes, but most of the time-resolved anisotropy systems cannot resolve all rotational

relaxation times due to poor resolution, there TAA can be advantageous. This method can be used to determine the rotational relaxation times of non-emissive molecules as well. The summary of Chapter 4 is illustrated in Figure 6.2.

In Chapter 5, BODIPY-perylene dyads are selected as sensitizer due to long triplet lifetime. The intersystem crossing pathway is investigated using femtosecond transient absorption spectroscopy and computational simulations. The dyads go through charge separation and recombination to form triplet species; this indicates the spin-orbit charge transfer intersystem crossing (SOCT-ISC) as triplet formation pathway. The non-orthogonal geometry of the dyads leads to the formation of triplet charge transfer species through spin-orbit coupling. The presence of iodine on dyad enhances the triplet yield and upconversion emission intensity. The species formed through ISC possess long triplet lifetime.

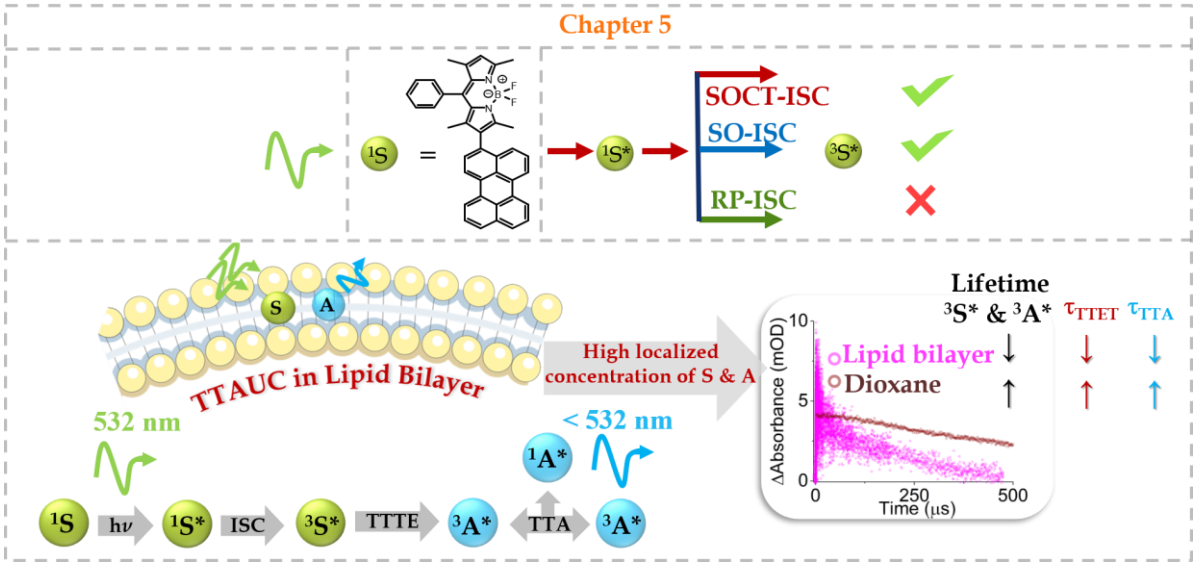

Figure 6.3: Graphical summary of the Chapter 5. Top: intersystem crossing in BODIPY-perylene dyad. Bottom: TTAUC in lipid bilayer. S: sensitizer, A: annihilator. SOCT: spin-orbit charge transfer, SO: spin-orbit, RP: radical pair. τ_{TTET}: TTET timescale, τ_{TTA}: TTA timescale. Upward and downward arrows represent higher and lower values with respect to each other.

The reconstitution of sensitizer and annihilator in large unilamellar vesicles (LUVs) localizes the molecule within the lipid bilayer. Therefore, increasing the local concentration leads to self-quenching of sensitizer triplets, but localization enhances the energy transfer rates. The observations made using time-resolved study of TTAUC in LUVs indicate despite higher viscosity of the medium, energy transfer is faster in lipid bilayer system. Long triplet lifetimes of the sensitizer and annihilators are advantageous in getting high upconversion yield, this study will be crucial in designing efficient light-activated drug delivery systems using liposomes. The

summary of Chapter 5 is illustrated in Figure 6.3.

The scientific investigations conducted in this thesis are summarized in Figure 6.4. The subsequent steps of this thesis endeavor will entail an examination of polymer-constrained sensitizer and annihilator (TTAUC systems) within gel media, as well as time-resolved investigation of sensitizer, annihilator and drug-containing liposomes. The findings of this thesis will be pivotal in comprehending these objectives, which will pave the way to find applications in solar cells and light-activated drug release from lab to practical applications.

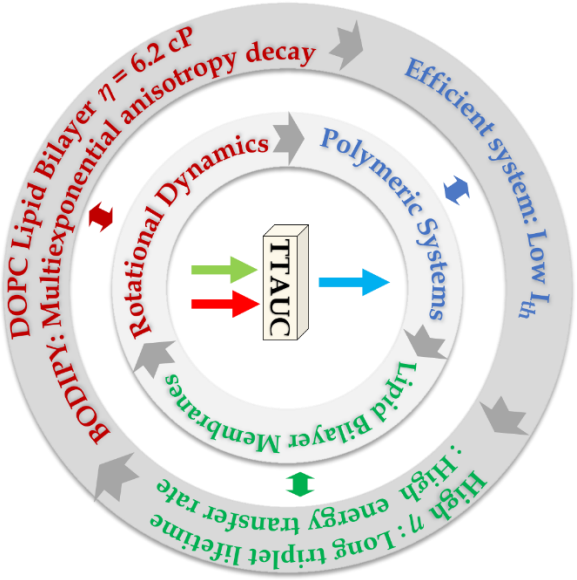

Figure 6.4: Schematic conclusion of the thesis.

7. Zusammenfassung

Die Triplett-Triplett-Annihilations-Hochkonversion (engl. Upconversion) (TTAUC) gewinnt auf dem Gebiet der optischen Spektroskopie zunehmend an Bedeutung und birgt ein immenses Potenzial verschiedene neue Technologien wie Solarzellen, Bioimaging und lichtaktivierte Arzneimittelfreisetzung zu revolutionieren. Dies ist auf die Fähigkeit zurückzuführen selbst bei niedrigen Anregungsleistungsdichten (~5 mW cm^{-2}) langwellige Photonen in energiereichere Photonen umzuwandeln. Ein großer Teil der Sonnenstrahlung liegt jenseits des Absorptionsfensters von Fotovoltaik; die Implementierung des TTAUC-Systems in Solarzellen kann diesen Teil der Sonnenstrahlung in das Absorptionsfenster der Fotovoltaik hochkonvertieren. Ebenso kann durch die niedrige Anregungsleistungsdichte die Freisetzung von Medikamenten aktiviert werden, ohne das Gewebe durch die Anregungsstrahlung zu schädigen.

Die Anwendung von TTAUC in Solarzellen oder bei der lichtaktivierten Medikamentenfreisetzung erfordert den Transfer des Hochkonversionsystems, bestehend aus Sensibilisator und Annihilator, von der flüssigen in die feste Phase. Die TTAUC ist jedoch in Lösungen am effizientesten und benötigt inerte Bedingungen. Die Herausforderung besteht darin, dass die Diffusion eine entscheidende Rolle bei den molekularen Prozessen des Triplett-Triplett-Energietransfers (TTET) und der Triplett-Triplett-Annihilation (TTA) spielt. Um die TTAUC in Festkörpermedien durchzuführen wurden von der Wissenschaft enorme Anstrengungen unternommen; zum Beispiel wurden verschiedene Methoden entwickelt, um sowohl Sensibilisator als auch Annihilator effektiv in Polymere einzubauen oder einen makromolekularen Annihilator mit monomeren Sensibilisatoren zu kombinieren. Für die Verabreichung von Medikamenten wurden Liposomen synthetisiert, die mit Sensibilisator, Annihilator und Medikamentenmolekülen rekonstituiert wurden. Die Umwandlung von rotem in blaues Licht durch die Liposomen hat die Freisetzung des Medikaments ermöglicht. Trotz dieser Fortschritte befindet sich die Technologie noch in der Entwicklungsphase.

Die vorliegende Arbeit füllt ausgewählte Lücken bei der Weiterentwicklung dieser vielversprechenden Anwendungen. Sie ist in drei Teile gegliedert. Im Zusammenhang mit der Festkörperanwendung von TTAUC wurden Makromolekül-Sensibilisatoren (Sensibilisatormoleküle, die an eine Polymerkette gebunden sind) mit monomerem Annihilator als TTAUC-System untersucht; dieses wissenschaftliche Ziel wurde in Kapitel 3 erreicht. Im Zusammenhang mit der lichtaktivierten Wirkstofffreisetzung wurden zwei wissenschaftliche Fragestellungen angegangen.

Erstens wurde die Viskosität des Mediums, die eine entscheidende Rolle bei der Diffusion von Molekülen spielt und die entscheidenden TTET- und TTA-Prozesse beeinflusst, mit Hilfe zeitaufgelöster Anisotropiemethoden in Kapitel 4 bestimmt. Zweitens wurde in Kapitel 5 die Triplett-Zustandslebensdauer, die die Effizienz der Energietransferprozesse bestimmt, im Medium der Doppellipidschicht untersucht. Diese Studien sind für die Optimierung eines TTAUC-Prozesses in einem Doppellipidschichtsystem unerlässlich. Diese wissenschaftlichen Ziele wurden mit Hilfe von stationärer, zeitaufgelöster Spektroskopie und computergestützten Simulationsmethoden untersucht.

In Kapitel 3 wurde ein esterverbundenes molekularer Ru(2,2-Bipyridin)$_2$-Sensibilisator in die Seitenketten eines Polymethylmethacrylat (PMMA)-Polymers polymerisiert. Der polymerisierte Sensibilisator dient als makromolekularer Photosensibilisator und wird zusammen mit 9,10-Diphenylanthracen als Annihilator aufgelöst.

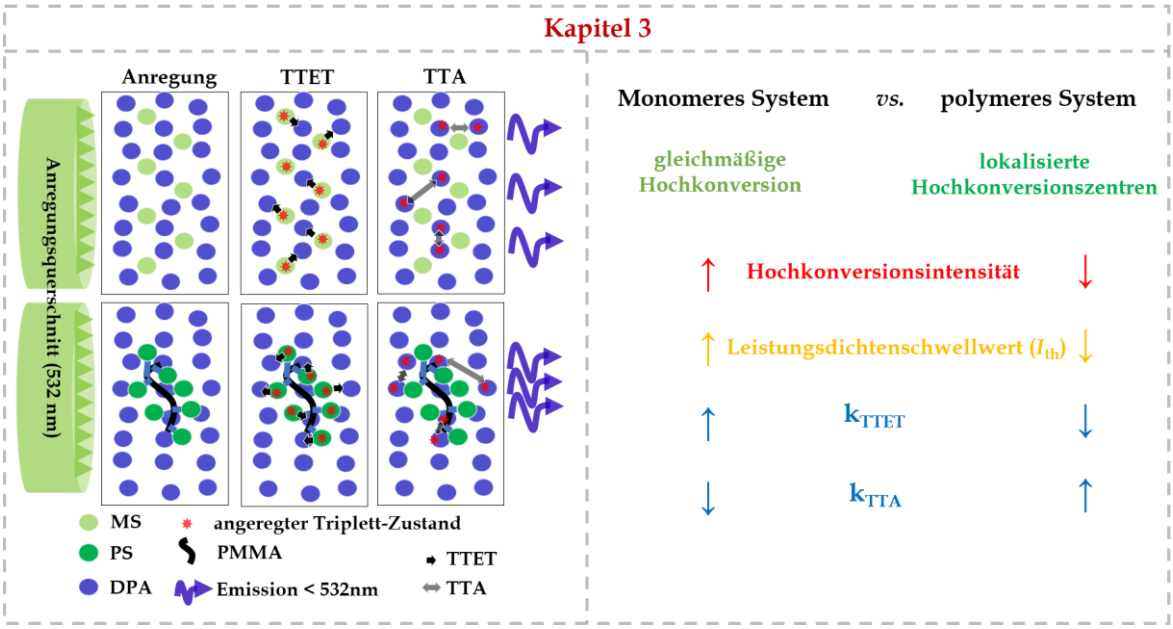

Abbildung 7.1: Grafische Zusammenfassung von Kapitel 3. Links: Darstellung der Hochkonversionsemission von monomeren und polymeren Sensibilisatoren mit monomeren Annihilatoren. Rechts: Charakteristika der Hochkonversionssysteme. Pfeile nach oben und unten weisen auf verhältnismäßig größere und kleinere Werte hin.

Die Studie zeigt, dass der makromolekulare Sensibilisator und der monomere Annihilator Hochkonversionsphotonen bei sehr niedrigen Anregungsleistungsdichten (6 mW cm^{-2}) erzeugen können. Obwohl die Intensität der Hochkonversion geringer ist als die der monomeren Gegenstücke, ist die Leistungsdichtenschwellwertes (engl. threshold intensity, I_{th}), bei der das Hochkonversionssystem seine 50%ige Effizienz erreicht, im Falle der polymeren Systeme niedriger. Der polymere Sensibilisator, der viel größer ist als der monomere

Sensibilisator, zeigt eine 1,6-mal niedrigere TTET-Rate aufgrund der größenbedingten langsameren Diffusion. Er erzeugt aber lokalisierte Triplett-Annihilatoren für den TTA-Prozess, was zu einer 2,2-mal höheren TTA-Rate als bei dem monomeren Gegenstück führt. Die hohe TTA-Rate ist auch für die niedrige I_{th} in polymeren Systemen verantwortlich. Die Beobachtung des niedrigen Leistungsdichtenschwellwertes (I_{th}) im Polymersystem zeigt die Wirksamkeit des Systems bei niedriger Anregungsleistungsdichte, was bei der Entwicklung von TTAUC-Systemen für die Anwendung in Solarzellen nützlich sein kann, um Sonnenstrahlung längerer Wellenlängen zu nutzen. Eine Zusammenfassung des Kapitels 3 ist in Abbildung 7.1 dargestellt.

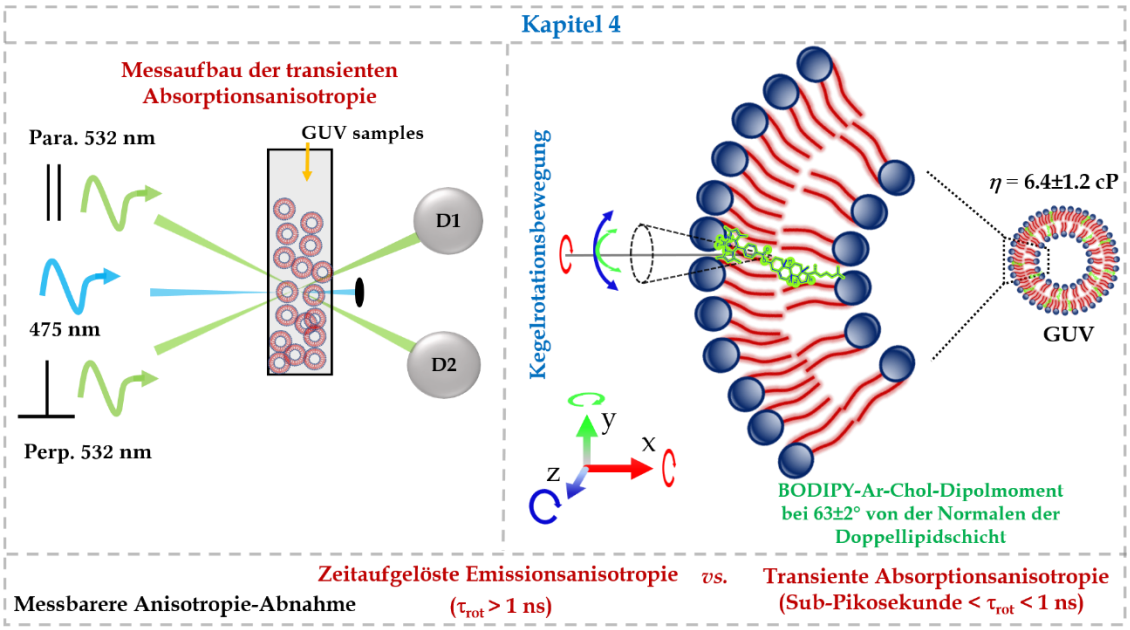

Abbildung 7.2: Grafische Zusammenfassung von Kapitel 4. Links: Aufbau der transienten Absorptionsanisotropiemessung für BODIPY-Ar-Chol in DCM und GUVs. Rechts: Orientierung des BODIPY-Ar-Chol-Moleküls und seine Rotation in einem GUV. Para: parallel zur Pump-Polarisation; Perp: senkrecht zur Pump-Polarisation. D1 und D2 sind zwei Detektoren, die zur Messung des durchgelassenen Lichts verwendet werden. τ_{rot}: Rotationsrelaxationszeit.

In Kapitel 4 wird die Rotationsdiffusion des BODIPY-Derivats (BODIPY-Ar-Chol) in Dichlormethan (DCM) und 1,2-Dioleoyl-sn-Glycero-3-Phosphocholin (DOPC) in riesigen unilamellaren Vesikeln (engl. giant unilamellar vesicles, GUVs) mittels polarisationsaufgelöster konfokaler Mikroskopie, zeitaufgelöster Emissionsanisotropie und transienter Absorptionsanisotropie untersucht. Die polarisationsaufgelöste konfokale Mikroskopie eines GUV in der Äquatorialebene zeigt die Platzierung der BODIPY-Moleküle in unmittelbarer Nähe der polaren Kopfgruppen der Lipide, während die Cholesterin-Moleküle entlang der Acyl-Kette der Lipide innerhalb der Membran angeordnet sind.

Die transiente Absorptionsanisotropie (TAA) benötigt nicht die Emission des Chromophors, um die Rotationsrelaxationszeiten zu messen, und besitzt eine höhere Auflösung als die zeitaufgelöste Emissionsanisotropie (TEA). Die sphäroidische Form des BODIPY-Ar-Chols führt zu einer tri-exponentiellen Abnahme der Anisotropie in DCM, während die starre Einbettung in GUVs zu einer bi-exponentiellen Abnahme der Anisotropie führt. Die Mikroviskosität wird auf 6,4±1,2° cP geschätzt. Die Beobachtungen, die mit Hilfe von Messungen der transienten Absorptionsanisotropie (TAA) gemacht wurden, werden bei der Bestimmung der wahren Rotationsdynamik eines Moleküls vorteilhaft sein. Die meisten verwendeten Moleküle sind nicht kugelförmig, aber die meisten zeitaufgelösten Anisotropiesysteme können aufgrund der schlechten Auflösung nicht alle Rotationsrelaxationszeiten auflösen, daher ist TAA hilfreich. Diese Methode kann auch zur Bestimmung der Rotationsrelaxationszeiten von nicht-emissiven Molekülen nützlich sein. Eine Zusammenfassung des Kapitels 4 ist in Abbildung 7.2 dargestellt.

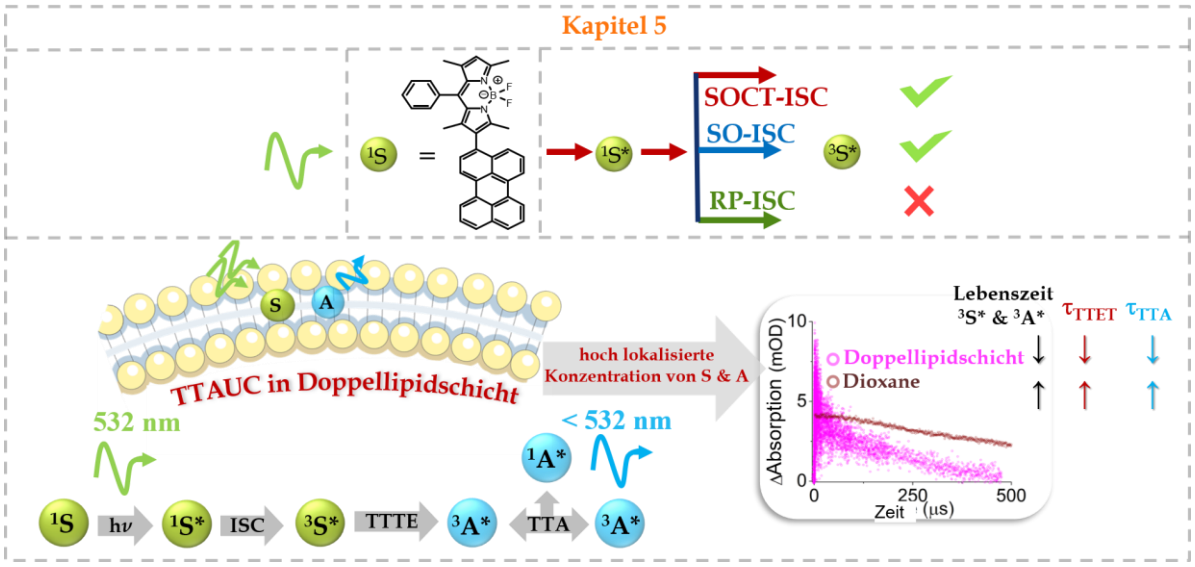

Abbildung 7.3: Grafische Zusammenfassung von Kapitel 5. Oben: Kreuzung der Systeme in der BODIPY-Perylen-Dyade. Unten: TTAUC in einer Doppellipidschicht. S: Sensibilisator, A: Annihilator. SOCT: Spin-Orbit-Ladungstransfer, SO: Spin-Orbit, RP: Radikalpaar. τ_{TTET}: TTET Zeitskala, τ_{TTA}: TTA Zeitskala. Pfeile nach oben und unten weisen auf verhältnismäßig größere und kleinere Werte hin.

In Kapitel 5 werden BODIPY-Perylen-Dyaden aufgrund ihrer langen Triplett-Lebensdauer als Sensibilisatoren ausgewählt. Der Weg des Übergangs zwischen den Systemen wird mit Hilfe von Femtosekunden-Absorptionsspektroskopie und Computersimulationen untersucht. Die Dyaden durchlaufen Ladungstrennung und Rekombination, um Triplett-Spezies zu bilden, was auf den Spin-Orbit-Ladungstransfer-Intersystemübergang (engl. spin-orbit charge transfer intersystem crossing, SOCT-ISC) als Triplett-Bildungsweg hinweist.

Die nicht orthogonale Geometrie der Dyaden führt zur Bildung von Triplett-Ladungstransferspezies durch Spin-Orbit-Kopplung. Das Vorhandensein von Iod auf der Dyade erhöht die Triplettausbeute und die Intensität der Hochkonversions-Emission. Die durch beide ISC-Wege gebildeten Triplett-Spezies besitzen eine lange Lebensdauer. Die Rekonstitution von Sensibilisator und Annihilator in großen unilamellaren Vesikeln (engl. large unilamellar vesicles, LUVs) lokalisiert die Moleküle innerhalb der Doppellipidschicht und erhöht somit die lokale Konzentration, was zum Selbst-Quenching der Sensibilisator-Tripletts führt; die Lokalisierung erhöht jedoch die Energietransferraten. Die Beobachtungen, die mit der zeitaufgelösten Studie von TTAUC in LUVs gemacht wurden, zeigen, dass trotz der höheren Viskosität des Mediums die Energieübertragungsraten in Doppellipidschichtsystemen höher sind, dass lange Triplett-Lebensdauern des Sensibilisators und der Annihilatoren hilfreich sind, um eine höhere Upconversion-Ausbeute zu erhalten, und dass diese Studie bei der Entwicklung effizienter lichtaktivierter Medikamentenfreisetzungssysteme mit Liposomen hilfreich sein wird. Eine Zusammenfassung des Kapitels 5 ist in Abbildung 7.3 dargestellt. Eine Übersicht aller wissenschaftlichen Untersuchungen dieser Arbeit ist in Abbildung 7.4 zu sehen. Die weiteren Schritte dieser Arbeit umfassen eine Untersuchung der Polymer-basierten Sensibilisator und Annihilatoren in Gelmedien sowie zeitaufgelöste Analysen von Sensibilisatoren, Annihilatoren und arzneimittelhaltigen Liposomen. Die Ergebnisse dieser Arbeit werden entscheidend zum Verständnis dieser Ziele beitragen, die den Weg für Anwendungen in Solarzellen und für die lichtaktivierte Freisetzung von Arzneimitteln vom Labor in die Praxis ebnen werden.

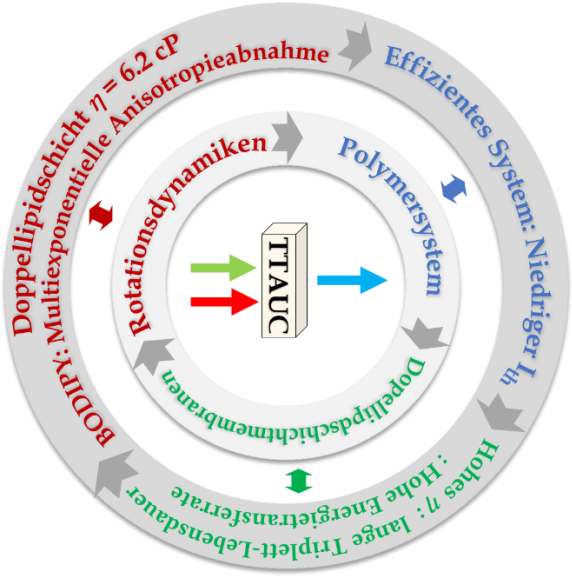

Abbildung 7.4: Schematischer Abschluss der Arbeit.

Bibliography

References

(1) Sheppard, N.; Willis, H. A.; Rigg, J. C. Names, Symbols, Definitions and Units of Quantities in Optical Spectroscopy (Recommendations 1984). *Pure and Applied Chemistry* **1985**, *57* (1), 105–120.

(2) Svelto, O.; Hanna, D. C. *Principles of Lasers*; Springer, 2010; Vol. 1.

(3) Siegman, A. E. *Lasers*; University science books, 1986.

(4) Trupke, T.; Shalav, A.; Richards, B. S.; Würfel, P.; Green, M. A. Efficiency Enhancement of Solar Cells by Luminescent Up-Conversion of Sunlight. *Solar Energy Materials and Solar Cells* **2006**, *90* (18–19), 3327–3338. https://doi.org/10.1016/j.solmat.2005.09.021.

(5) Ekins-Daukes, N. J.; Schmidt, T. W. A Molecular Approach to the Intermediate Band Solar Cell: The Symmetric Case. *Appl Phys Lett* **2008**, *93* (6), 2–5. https://doi.org/10.1063/1.2970157.

(6) Askes, S. H. C.; Bahreman, A.; Bonnet, S. Activation of a Photodissociative Ruthenium Complex by Triplet-Triplet Annihilation Upconversion in Liposomes. *Angewandte Chemie* **2014**, *126* (4), 1047–1051. https://doi.org/10.1002/ange.201309389.

(7) Wandelt, K. *Encyclopedia of Interfacial Chemistry: Surface Science and Electrochemistry*; Elsevier, 2018.

(8) Gray, V.; Moth-Poulsen, K.; Albinsson, B.; Abrahamsson, M. Towards Efficient Solid-State Triplet–Triplet Annihilation Based Photon Upconversion: Supramolecular, Macromolecular and Self-Assembled Systems. *Coord Chem Rev* **2018**, *362*, 54–71. https://doi.org/10.1016/j.ccr.2018.02.011.

(9) Singh-Rachford, T. N.; Castellano, F. N. Photon Upconversion Based on Sensitized Triplet-Triplet Annihilation. *Coord Chem Rev* **2010**, *254* (21–22), 2560–2573. https://doi.org/10.1016/j.ccr.2010.01.003.

(10) Jha, K. K.; Prabhakaran, A.; Burke, C. S.; Schulze, M.; Schubert, U. S.; Keyes, T. E.; Jäger, M.; Ivanšić, B. D. Triplet–Triplet Annihilation Upconversion by Polymeric Sensitizers. *The Journal of Physical Chemistry C* **2022**, *126* (8), 4057–4066. https://doi.org/10.1021/acs.jpcc.1c09897.

(11) Moor, K.; Kim, J. H.; Snow, S.; Kim, J. H. [C70] Fullerene-Sensitized Triplet-Triplet Annihilation Upconversion. *Chemical Communications* **2013**, *49* (92), 10829–10831. https://doi.org/10.1039/c3cc46598e.

(12) Singh-Rachford, T. N.; Haefele, A.; Ziessel, R.; Castellano, F. N. Boron Dipyrromethene Chromophores: Next Generation Triplet Acceptors/Annihilators for Low Power Upconversion Schemes. *J Am Chem Soc* **2008**, *130* (48), 16164–16165. https://doi.org/10.1021/ja807056a.

(13) Hao, R.; Ye, C.; Wang, X.; Zhu, L.; Chen, S.; Yang, J.; Tao, X. PH-Responsive Low-Power Upconversion Based on Sandwichlike Palladiumphthalocyanine and Rhodamine B. *Journal of Physical Chemistry C* **2017**, *121* (25), 13524–13531. https://doi.org/10.1021/acs.jpcc.7b02785.

(14) Ravetz, B. D.; Pun, A. B.; Churchill, E. M.; Congreve, D. N.; Rovis, T.; Campos, L. M. Photoredox Catalysis Using Infrared Light via Triplet Fusion Upconversion. *Nature* **2019**, *565* (7739), 343–346. https://doi.org/10.1038/s41586-018-0835-2.

(15) Parker, C. A.; Hatchard, C. G.; C . A . Parker and C . G . Hatchard. Delayed Fluorescence from Solutions of Anthracene and Phenanthrene. *Proc R Soc Lond A Math Phys Sci* **1962**, *269* (1339), 574–584.

(16) Schmidt, T. W.; Castellano, F. N. Photochemical Upconversion: The Primacy of Kinetics. *Journal of Physical Chemistry Letters* **2014**, *5* (22), 4062–4072. https://doi.org/10.1021/jz501799m.

(17) Haefele, A.; Blumhoff, J.; Khnayzer, R. S.; Castellano, F. N. Getting to the (Square) Root of the Problem: How to Make Noncoherent Pumped Upconversion Linear. *Journal of Physical Chemistry Letters* **2012**, *3* (3), 299–303. https://doi.org/10.1021/jz300012u.

(18) De Wild, J.; Meijerink, A.; Rath, J. K.; Van Sark, W. G. J. H. M.; Schropp, R. E. I. Upconverter Solar Cells: Materials and Applications. *Energy Environ Sci* **2011**, *4* (12), 4835–4848. https://doi.org/10.1039/c1ee01659h.

(19) Gray, V.; Dzebo, D.; Abrahamsson, M.; Albinsson, B.; Moth-Poulsen, K. Triplet-Triplet Annihilation Photon-Upconversion: Towards Solar Energy Applications. *Physical Chemistry Chemical Physics* **2014**, *16* (22), 10345–10352. https://doi.org/10.1039/c4cp00744a.

(20) Shockley, W.; Queisser, H. Detailed Balance Limit of Efficiency of P-n Junction

Solar Cells. *Renewable Energy: Four Volume Set* **2018**, *2–4* (May 1960), 35–54. https://doi.org/10.4324/9781315793245-44.

(21) Cheng, Y. Y.; Fückel, B.; MacQueen, R. W.; Khoury, T.; Clady, R. G. C. R.; Schulze, T. F.; Ekins-Daukes, N. J.; Crossley, M. J.; Stannowski, B.; Lips, K.; Schmidt, T. W. Improving the Light-Harvesting of Amorphous Silicon Solar Cells with Photochemical Upconversion. *Energy Environ Sci* **2012**, *5* (5), 6953–6959. https://doi.org/10.1039/c2ee21136j.

(22) Nattestad, A.; Cheng, Y. Y.; Macqueen, R. W.; Schulze, T. F.; Thompson, F. W.; Mozer, A. J.; Fückel, B.; Khoury, T.; Crossley, M. J.; Lips, K.; Wallace, G. G.; Schmidt, T. W. Dye-Sensitized Solar Cell with Integrated Triplet-Triplet Annihilation Upconversion System. *Journal of Physical Chemistry Letters* **2013**, *4* (12), 2073–2078. https://doi.org/10.1021/jz401050u.

(23) Porter, G.; Wilkinson, F.; A, P. R. S. L. Energy Transfer from the Triplet State. *Proc R Soc Lond A Math Phys Sci* **1961**, *264* (1316), 1–18. https://doi.org/10.1098/rspa.1961.0182.

(24) Çakmak, Y.; Kolemen, S.; Buyuktemiz, M.; Dede, Y.; Erten-Ela, S. Synthesis and Dye Sensitized Solar Cell Applications of Bodipy Derivatives with Bis-Dimethylfluorenyl Amine Donor Groups. *New Journal of Chemistry* **2015**, *39* (5), 4086–4092.

(25) Askes, S. H. C.; Kloz, M.; Bruylants, G.; Kennis, J. T. M.; Bonnet, S. Triplet-Triplet Annihilation Upconversion Followed by FRET for the Red Light Activation of a Photodissociative Ruthenium Complex in Liposomes. *Physical Chemistry Chemical Physics* **2015**, *17* (41), 27380–27390. https://doi.org/10.1039/c5cp04352b.

(26) Durandin, N. A.; Isokuortti, J.; Efimov, A.; Vuorimaa-Laukkanen, E.; Tkachenko, N. V.; Laaksonen, T. Efficient Photon Upconversion at Remarkably Low Annihilator Concentrations in a Liquid Polymer Matrix: When Less Is More. *Chemical Communications* **2018**, *54* (99), 14029–14032. https://doi.org/10.1039/c8cc07592a.

(27) Boutin, P. C.; Ghiggino, K. P.; Kelly, T. L.; Steer, R. P. Photon Upconversion by Triplet-Triplet Annihilation in Ru(Bpy)3- and DPA-Functionalized Polymers. *Journal of Physical Chemistry Letters* **2013**, *4* (23), 4113–4118. https://doi.org/10.1021/jz402311j.

(28) Islangulov, R. R.; Singh, T.; Lott, J.; Weder, C.; Castellano, F. N. Low-Power

Upconversion in Solid Polymer Films. *American Chemical Society, Polymer Preprints, Division of Polymer Chemistry* **2008**, *49* (1), 1028–1029.

(29) Capadona, J. R.; Van Den Berg, O.; Capadona, L. A.; Schroeter, M.; Rowan, S. J.; Tyler, D. J.; Weder, C. A Versatile Approach for the Processing of Polymer Nanocomposites with Self-Assembled Nanofibre Templates. *Nat Nanotechnol* **2007**, *2* (12), 765–769. https://doi.org/10.1038/nnano.2007.379.

(30) Schroers, M.; Kokil, A.; Weder, C. Solid Polymer Electrolytes Based on Nanocomposites of Ethylene Oxide-Epichlorohydrin Copolymers and Cellulose Whiskers. *J Appl Polym Sci* **2004**, *93* (6), 2883–2888. https://doi.org/10.1002/app.20870.

(31) Mongin, C.; Golden, J. H.; Castellano, F. N. Liquid PEG Polymers Containing Antioxidants: A Versatile Platform for Studying Oxygen-Sensitive Photochemical Processes. *ACS Appl Mater Interfaces* **2016**, *8* (36), 24038–24048. https://doi.org/10.1021/acsami.6b05697.

(32) Lee, S. H.; Ayer, M. A.; Vadrucci, R.; Weder, C.; Simon, Y. C. Light Upconversion by Triplet-Triplet Annihilation in Diphenylanthracene-Based Copolymers. *Polym Chem* **2014**, *5* (24), 6898–6904. https://doi.org/10.1039/c4py00920g.

(33) Sittig, M.; Schmidt, B.; Görls, H.; Bocklitz, T.; Wächtler, M.; Zechel, S.; Hager, M. D.; Dietzek, B. Fluorescence Upconversion by Triplet-Triplet Annihilation in All-Organic Poly(Methacrylate)-Terpolymers. *Phys Chem Chem Phys* **2020**, *22* (7), 4072–4079. https://doi.org/10.1039/d0cp00232a.

(34) Edhborg, F.; Bildirir, H.; Bharmoria, P.; Moth-Poulsen, K.; Albinsson, B. Intramolecular Triplet–Triplet Annihilation Photon Upconversion in Diffusionally Restricted Anthracene Polymer. *J Phys Chem B* **2021**, *125* (23), 6255–6263. https://doi.org/10.1021/acs.jpcb.1c02856.

(35) Zhang, G.; Zhang, D. New Photosensitizer Design Concept: Polymerization-Enhanced Photosensitization. *Chem* **2018**, *4* (9), 2013–2015. https://doi.org/10.1016/j.chempr.2018.08.027.

(36) Wu, W.; Mao, D.; Xu, S.; Kenry; Hu, F.; Li, X.; Kong, D.; Liu, B. Polymerization-Enhanced Photosensitization. *Chem* **2018**, *4* (8), 1937–1951. https://doi.org/10.1016/j.chempr.2018.06.003.

(37) Askes, S. H. C.; Brodie, P.; Bruylants, G.; Bonnet, S. Temperature Dependence of Triplet-Triplet Annihilation Upconversion in Phospholipid Membranes.

Journal of Physical Chemistry B **2017**, *121* (4), 780–786. https://doi.org/10.1021/acs.jpcb.6b10039.

(38) Ariola, F. S.; Li, Z.; Cornejo, C.; Bittman, R.; Heikal, A. A. Membrane Fluidity and Lipid Order in Ternary Giant Unilamellar Vesicles Using a New Bodipy-Cholesterol Derivative. *Biophys J* **2009**, *96* (7), 2696–2708. https://doi.org/10.1016/j.bpj.2008.12.3922.

(39) Fujiwara, T.; Nagayama, K. The Wobbling-in-a-Cone Analysis of Internal Motion in Macromolecules. *J Chem Phys* **1985**, *83* (6), 3110–3117. https://doi.org/10.1063/1.449217.

(40) Jameson, D. M.; Ross, J. A. Fluorescence Polarization/Anisotropy in Diagnostics and Imaging. *Chem Rev* **2010**, *110* (5), 2685–2708. https://doi.org/10.1021/cr900267p.

(41) Weinreis, S. A.; Ellis, J. P.; Cavagnero, S.; n, Eunsung Mouradian, M. M. Dynamic Fluorescence Depolarization: A Powerful Tool to Explore Protein Folding on the Ribosome. *Methods* **2010**, *52* (1), 57–73. https://doi.org/10.1016/j.ymeth.2010.06.001.

(42) Solanko, L. M.; Honigmann, A.; Midtiby, H. S.; Lund, F. W.; Brewer, J. R.; Dekaris, V.; Bittman, R.; Eggeling, C.; Wüstner, D. Membrane Orientation and Lateral Diffusion of BODIPY-Cholesterol as a Function of Probe Structure. *Biophys J* **2013**, *105* (9), 2082–2092. https://doi.org/10.1016/j.bpj.2013.09.031.

(43) Dent, M. R.; Ló Pez-Duarte, I.; Dickson, C. J.; Geoghegan, N. D.; Cooper, J. M.; Gould, I. R.; Krams, R.; Bull, J. A.; Brooks, N. J.; Kuimova, M. K.; López-Duarte, I.; Dickson, C. J.; Geoghegan, N. D.; Cooper, J. M.; Gould, I. R.; Krams, R.; Bull, J. A.; Brooks, N. J.; Kuimova, M. K. Imaging Phase Separation in Model Lipid Membranes through the Use of BODIPY Based Molecular Rotors. *Phys. Chem. Chem. Phys* **2015**, *17* (28), 18393. https://doi.org/10.1039/c5cp01937k.

(44) Miao, W.; Yu, C.; Hao, E.; Jiao, L. Functionalized BODIPYs as Fluorescent Molecular Rotors for Viscosity Detection. *Front Chem* **2019**, *7* (November), 1–6. https://doi.org/10.3389/fchem.2019.00825.

(45) Aguilar, L. F.; Pino, J. A.; Soto-Arriaza, M. A.; Cuevas, F. J.; Sánchez, S.; Sotomayor, C. P. Differential Dynamic and Structural Behavior of Lipid-Cholesterol Domains in Model Membranes. *PLoS One* **2012**, *7* (6). https://doi.org/10.1371/journal.pone.0040254.

(46) De Almeida, R. F. M.; Borst, J.; Fedorov, A.; Prieto, M.; Visser, A. J. W. G. Complexity of Lipid Domains and Rafts in Giant Unilamellar Vesicles Revealed by Combining Imaging and Microscopic and Macroscopic Time-Resolved Fluorescence. *Biophys J* **2007**, *93* (2), 539–553. https://doi.org/10.1529/biophysj.106.098822.

(47) ThermoFisher Scientific. Probes for Lipids and Membranes. *Molecular Probes Handbook* **2010**, *76* (11), 547–589.

(48) Koan, M. M.; Blanchard, G. J. Gauging the Effect of Impurities on Lipid Bilayer Phase Transition Temperature. *Journal of Physical Chemistry B* **2006**, *110* (33), 16584–16590. https://doi.org/10.1021/jp061506s.

(49) Kuimova, M. K. Mapping Viscosity in Cells Using Molecular Rotors. *Phys. Chem. Chem. Phys* **2012**, *14*, 12671–12686. https://doi.org/10.1039/c2cp41674c.

(50) Lee, A. G. How Lipids Affect the Activities of Integral Membrane Proteins. *Biochim Biophys Acta Biomembr* **2004**, *1666* (1–2), 62–87. https://doi.org/10.1016/j.bbamem.2004.05.012.

(51) Pillman, H. A.; Blanchard, G. J. Consequences of Transient Heating on the Motional Dynamics of Cholesterol-Containing Phospholipid Vesicles. *Journal of Physical Chemistry B* **2011**, *115* (14), 3819–3827. https://doi.org/10.1021/jp111020j.

(52) Brasselet, S.; Ferrand, P.; Kress, A.; Wang, X.; Ranchon, H.; Gasecka, A. Imaging Molecular Order in Cell Membranes by Polarization-Resolved Fluorescence Microscopy. In *Fluorescent Methods to Study Biological Membranes*; Springer, Berlin, Heidelberg, 2012; pp 311–337. https://doi.org/10.1007/4243_2012_51.

(53) Brasselet, S.; Ferrand, P.; Kress, A.; Wang, X.; Ranchon, H.; Gasecka, A. Imaging Molecular Order in Cell Membranes by Polarization-Resolved Fluorescence Microscopy BT - Fluorescent Methods to Study Biological Membranes; Mély, Y., Duportail, G., Eds.; Springer Berlin Heidelberg: Berlin, Heidelberg, 2013; pp 311–337. https://doi.org/10.1007/4243_2012_51.

(54) Gasecka, A.; Han, T. J.; Favard, C.; Cho, B. R.; Brasselet, S. Quantitative Imaging of Molecular Order in Lipid Membranes Using Two-Photon Fluorescence Polarimetry. *Biophys J* **2009**, *97* (10), 2854–2862. https://doi.org/10.1016/j.bpj.2009.08.052.

(55) Karolin, J.; Johansson, L. B. A.; Strandberg, L.; Ny, T. Fluorescence and

Absorption Spectroscopic Properties of Dipyrrometheneboron Difluoride (BODIPY) Derivatives in Liquids, Lipid Membranes, and Proteins. *J Am Chem Soc* **1994**, *116* (17), 7801–7806. https://doi.org/10.1021/ja00096a042.

(56) Ariola, F. S.; Mudaliar, D. J.; Walvick, R. P.; Heikal, A. A. Dynamics Imaging of Lipid Phases and Lipid-Marker Interactions in Model Biomembranes. *Physical Chemistry Chemical Physics* **2006**, *8* (39), 4517–4529. https://doi.org/10.1039/b608629b.

(57) van der Meer, W.; Pottel, H.; Herreman, W.; Ameloot, M.; Hendrickx, H.; Schröder, H. Effect of Orientational Order on the Decay of the Fluorescence Anisotropy in Membrane Suspensions. A New Approximate Solution of the Rotational Diffusion Equation. *Biophys J* **1984**, *46* (4), 515–523. https://doi.org/10.1016/S0006-3495(84)84049-7.

(58) Smith, T. A.; Ghiggino, K. P. A Review of the Analysis of Complex Time-Resolved Fluorescence Anisotropy Data. *Methods Appl Fluoresc* **2015**, *3* (2). https://doi.org/10.1088/2050-6120/3/2/022001.

(59) Lakowicz, J. R. *Principles of Fluorescence Spectroscopy*, 3rd ed.; Dr. Joseph R. Lakowicz, Ed.; Springer, Boston, MA, 2006. https://doi.org/10.1007/978-0-387-46312-4.

(60) Yuan, Y.; Liu, B. Visualization of Drug Delivery Processes Using AIEgens. *Chem Sci* **2017**, *8* (4), 2537–2546. https://doi.org/10.1039/C6SC05421H.

(61) Parvathy Venu,Trong-Nghia Le; Pawan Kumar, Diptendu Patra, R. K.; Lee, C.-K.; N. Vijayakameswara Rao, R. S. Efficient Design to Monitor the Site-specific Sustained Release of a Non-Emissive Anticancer Drug. *Chem Asian J* **2021**, *16* (17), 2552–2558. https://doi.org/doi.org/10.1002/asia.202100355.

(62) Youyong Yuan, Chong-Jing Zhang, Meng Gao, Ruoyu Zhang, Ben Zhong Tang, and B. L. Specific Light-Up Bioprobe with Aggregation-Induced Emission and Activatable. *Angewandte Chemie - International Edition* **2015**, *54* (6), 1780 –1786. https://doi.org/10.1002/anie.201408476.

(63) O'Connor, D.; Byrne, A.; Keyes, T. E. Linker Length in Fluorophore-Cholesterol Conjugates Directs Phase Selectivity and Cellular Localisation in GUVs and Live Cells. *RSC Adv* **2019**, *9* (40), 22805–22816. https://doi.org/10.1039/c9ra03905h.

(64) Askes, S. H. C.; Leeuwenburgh, V. C.; Pomp, W.; Arjmandi-Tash, H.; Tanase, S.; Schmidt, T.; Bonnet, S. Water-Dispersible Silica-Coated Upconverting

Liposomes: Can a Thin Silica Layer Protect TTA-UC against Oxygen Quenching? *ACS Biomater Sci Eng* **2017**, *3* (3), 322–334. https://doi.org/10.1021/acsbiomaterials.6b00678.

(65) Askes, S. H. C.; Mora, N. L.; Harkes, R.; Koning, R. I.; Koster, B.; Schmidt, T.; Kros, A.; Bonnet, S. Imaging the Lipid Bilayer of Giant Unilamellar Vesicles Using Red-to-Blue Light Upconversion. *Chemical Communications* **2015**, *51* (44), 9137–9140. https://doi.org/10.1039/c5cc02197a.

(66) Manna, M. K.; Shokri, S.; Wiederrecht, G. P.; Gosztola, D. J.; Ayitou, A. J. L. New Perspectives for Triplet-Triplet Annihilation Based Photon Upconversion Using All-Organic Energy Donor & Acceptor Chromophores. *Chemical Communications* **2018**, *54* (46), 5809–5818. https://doi.org/10.1039/c8cc01553h.

(67) Zhao, J.; Wu, W.; Sun, J.; Guo, S. Triplet Photosensitizers: From Molecular Design to Applications. *Chem Soc Rev* **2013**, *42* (12), 5323–5351. https://doi.org/10.1039/c3cs35531d.

(68) Abrahamsson, M.; Jäger, M.; Kumar, R. J.; Österman, T.; Persson, P.; Becker, H. C.; Johansson, O.; Hammarström, L. Bistridentate Ruthenium(II)Polypyridyl-Type Complexes with Microsecond 3MLCT State Lifetimes: Sensitizers for Rod-like Molecular Arrays. *J Am Chem Soc* **2008**, *130* (46), 15533–15542. https://doi.org/10.1021/ja804890k.

(69) Tilley, A. J.; Kim, M. J.; Chen, M.; Ghiggino, K. P. Photo-Induced Energy Transfer in Ruthenium-Centred Polymers Prepared by a RAFT Approach. *Polymer (Guildf)* **2013**, *54* (12), 2865–2872. https://doi.org/10.1016/j.polymer.2013.03.064.

(70) Wu, W.; Ji, S.; Wu, W.; Shao, J.; Guo, H.; James, T. D.; Zhao, J. Ruthenium(II)-Polyimine-Coumarin Light-Harvesting Molecular Arrays: Design Rationale and Application for Triplet-Triplet-Annihilation-Based Upconversion. *Chemistry - A European Journal* **2012**, *18* (16), 4953–4964. https://doi.org/10.1002/chem.201101377.

(71) Tyson, D. S.; Henbest, K. B.; Bialecki, J.; Castellano, F. N. Excited State Processes in Ruthenium(II)/Pyrenyl Complexes Displaying Extended Lifetimes. *Journal of Physical Chemistry A* **2001**, *105* (35), 8154–8161. https://doi.org/10.1021/jp011770f.

(72) Zhou, Y.; Castellano, F. N.; Schmidt, T. W.; Hanson, K. On the Quantum Yield of Photon Upconversion via Triplet-Triplet Annihilation. *ACS Energy Lett* **2020**,

5 (7), 2322–2326. https://doi.org/10.1021/acsenergylett.0c01150.

(73) Dzebo, D.; Moth-Poulsen, K.; Albinsson, B. Robust Triplet-Triplet Annihilation Photon Upconversion by Efficient Oxygen Scavenging. *Photochemical and Photobiological Sciences* **2017**, *16* (8), 1327–1334. https://doi.org/10.1039/c7pp00201g.

(74) Filatov, M. A.; Baluschev, S.; Landfester, K. Protection of Densely Populated Excited Triplet State Ensembles against Deactivation by Molecular Oxygen. *Chem Soc Rev* **2016**, *45* (17), 4668–4689. https://doi.org/10.1039/c6cs00092d.

(75) Zhao, J.; Ji, S.; Guo, H. Triplet-Triplet Annihilation Based Upconversion: From Triplet Sensitizers and Triplet Acceptors to Upconversion Quantum Yields. *RSC Adv* **2011**, *1* (6), 937–950. https://doi.org/10.1039/c1ra00469g.

(76) Saltiel, J.; Atwater, B. W. Spin-Statistical Factors in Diffusion-Controlled Reactions. *Advances in Photochemistry* **2009**, *14*, 1–90.

(77) Charlton, J. L.; Dabestani, R.; Saltiel, J. Role of Triplet-Triplet Annihilation in Anthracene Dimerization. *J Am Chem Soc* **1983**, *105* (11), 3473–3476. https://doi.org/10.1021/ja00349a017.

(78) McLean, A. J.; Truscott, T. G. Faraday Communications. Efficiency of Triplet-Photosensitised Singlet Oxygen Generation in Benzene. *Journal of the Chemical Society, Faraday Transactions* **1990**, *86* (14), 2671–2672. https://doi.org/10.1039/FT9908602671.

(79) Bachilo, S. M.; Weisman, R. B. Determination of Triplet Quantum Yields from Triplet-Triplet Annihilation Fluorescence. *Journal of Physical Chemistry A*. 2000, pp 7713–7714. https://doi.org/10.1021/jp001877n.

(80) Mahboub, M.; Huang, Z.; Tang, M. L. Efficient Infrared-to-Visible Upconversion with Subsolar Irradiance. *Nano Lett* **2016**, *16* (11), 7169–7175. https://doi.org/10.1021/acs.nanolett.6b03503.

(81) Gray, V.; Xia, P.; Huang, Z.; Moses, E.; Fast, A.; Fishman, D. A.; Vullev, V. I.; Abrahamsson, M.; Moth-Poulsen, K.; Lee Tang, M. CdS/ZnS Core–Shell Nanocrystal Photosensitizers for Visible to UV Upconversion. *Chem Sci* **2017**, *8* (8), 5488–5496. https://doi.org/10.1039/C7SC01610G.

(82) Levin, P. P.; Costa, S. M. B.; Nunes, T. G.; Vieira Ferreira, L. F.; Ilharco, L. M.; Botelho do Rego, A. M. Kinetics of Triplet−Triplet Annihilation of Tetraphenylporphyrin in Liquid and Frozen Films of Decanol on the External

Surface of Zeolite. Fast Probe Diffusion in Monolayers and Polycrystals. *J Phys Chem A* **2003**, *107* (3), 328–336. https://doi.org/10.1021/jp021635i.

(83) Cheng, Y. Y.; Fückel, B.; Khoury, T.; Clady, R. G. C. R.; Tayebjee, M. J. Y.; Ekins-Daukes, N. J.; Crossley, M. J.; Schmidt, T. W. Kinetic Analysis of Photochemical Upconversion by Triplet-Triplet Annihilation: Beyond Any Spin Statistical Limit. *Journal of Physical Chemistry Letters*. 2010, pp 1795–1799. https://doi.org/10.1021/jz100566u.

(84) Cheng, Y. Y.; Khoury, T.; Clady, R. G. C. R.; Tayebjee, M. J. Y.; Ekins-Daukes, N. J.; Crossley, M. J.; Schmidt, T. W. On the Efficiency Limit of Triplet-Triplet Annihilation for Photochemical Upconversion. *Physical Chemistry Chemical Physics* **2010**, *12* (1), 66–71. https://doi.org/10.1039/b913243k.

(85) Hoseinkhani, S.; Tubino, R.; Meinardi, F.; Monguzzi, A. Achieving the Photon Up-Conversion Thermodynamic Yield Upper Limit by Sensitized Triplet-Triplet Annihilation. *Physical Chemistry Chemical Physics* **2015**, *17* (6), 4020–4024. https://doi.org/10.1039/c4cp03936j.

(86) Monguzzi, A.; Mézyk, J.; Scotognella, F.; Tubino, R.; Meinardi, F. Upconversion-Induced Fluorescence in Multicomponent Systems: Steady-State Excitation Power Threshold. *Phys Rev B Condens Matter Mater Phys* **2008**, *78* (19), 2–6. https://doi.org/10.1103/PhysRevB.78.195112.

(87) Monguzzi, A.; Duan, P. Highly Efficient Photon Upconversion Based on Triplet – Triplet Annihilation from Bichromophoric Annihilators. *J. Mater. Chem. C* **2021**, *9*, 14201–14208. https://doi.org/10.1039/d1tc01569a.

(88) Monguzzi, A.; Tubino, R.; Hoseinkhani, S.; Campione, M.; Meinardi, F. Low Power, Non-Coherent Sensitized Photon up-Conversion: Modelling and Perspectives. *Physical Chemistry Chemical Physics* **2012**, *14* (13), 4322–4332. https://doi.org/10.1039/c2cp23900k.

(89) Durandin, N. A.; Isokuortti, J.; Efimov, A.; Vuorimaa-Laukkanen, E.; Tkachenko, N. v.; Laaksonen, T. Critical Sensitizer Quality Attributes for Efficient Triplet-Triplet Annihilation Upconversion with Low Power Density Thresholds. *Journal of Physical Chemistry C* **2019**, *123* (37), 22865–22872. https://doi.org/10.1021/acs.jpcc.9b08026.

(90) Vanorman, Z. A.; Nienhaus, L. Bulk Metal Halide Perovskites as Triplet Sensitizers: Taking Charge of Upconversion. *ACS Energy Lett* **2021**, *6* (10), 3686–3694. https://doi.org/10.1021/acsenergylett.1c01794.

(91) Nienhaus, L.; Wu, M.; Bulović, V.; Baldo, M. A.; Bawendi, M. G. Using Lead Chalcogenide Nanocrystals as Spin Mixers: A Perspective on near-Infrared-to-Visible Upconversion. *Dalton Transactions* **2018**, *47* (26), 8509–8516. https://doi.org/10.1039/c8dt00419f.

(92) Wieghold, S.; Bieber, A. S.; VanOrman, Z. A.; Daley, L.; Leger, M.; Correa-Baena, J. P.; Nienhaus, L. Triplet Sensitization by Lead Halide Perovskite Thin Films for Efficient Solid-State Photon Upconversion at Subsolar Fluxes. *Matter* **2019**, *1* (3), 705–719. https://doi.org/10.1016/j.matt.2019.05.026.

(93) Nienhaus, L.; Correa-Baena, J. P.; Wieghold, S.; Einzinger, M.; Lin, T. A.; Shulenberger, K. E.; Klein, N. D.; Wu, M.; Bulović, V.; Buonassisi, T.; Baldo, M. A.; Bawendi, M. G. Triplet-Sensitization by Lead Halide Perovskite Thin Films for near-Infrared-to-Visible Upconversion. *ACS Energy Lett* **2019**, *4* (4), 888–895. https://doi.org/10.1021/acsenergylett.9b00283.

(94) Yang, M.; Sheykhi, S.; Zhang, Y.; Milsmann, C.; Castellano, F. N. Low Power Threshold Photochemical Upconversion Using a Zirconium(Iv) LMCT Photosensitizer. *Chem Sci* **2021**, *12* (26), 9069–9077. https://doi.org/10.1039/d1sc01662h.

(95) Pollnau, M.; Gamelin, D. R.; Lüthi, S. R.; Güdel, H. U.; Hehlen, M. P. Power Dependence of Upconversion Luminescence in Lanthanide and Transition-Metal-Ion Systems. *Phys Rev B* **2000**, *61* (5), 3337–3346. https://doi.org/10.1103/PhysRevB.61.3337.

(96) Dzebo, D.; Börjesson, K.; Gray, V.; Moth-Poulsen, K.; Albinsson, B. Intramolecular Triplet-Triplet Annihilation Upconversion in 9,10-Diphenylanthracene Oligomers and Dendrimers. *Journal of Physical Chemistry C* **2016**, *120* (41), 23397–23406. https://doi.org/10.1021/acs.jpcc.6b07920.

(97) Singh-Rachford, T. N.; Castellano, F. N. Supra-Nanosecond Dynamics of a Red-to-Blue Photon Upconversion System. *Inorg Chem* **2009**, *48* (6), 2541–2548. https://doi.org/10.1021/ic802114d.

(98) Murakami, Y.; Kamada, K. Kinetics of Photon Upconversion by Triplet-Triplet Annihilation: A Comprehensive Tutorial. *Physical Chemistry Chemical Physics* **2021**, *23* (34), 18268–18282. https://doi.org/10.1039/d1cp02654b.

(99) Murakami, Y.; Kikuchi, H.; Kawai, A. Kinetics of Photon Upconversion in Ionic Liquids: Time-Resolved Analysis of Delayed Fluorescence. *Journal of Physical Chemistry B* **2013**, *117* (17), 5180–5187. https://doi.org/10.1021/jp401474n.

(100) Lakowicz, J. R. *Time-Dependent Anisotropy Decays*; 1999. https://doi.org/10.1007/978-1-4757-3061-6_11.

(101) Lessing, H. E. Transient Absorption and Rotational Relaxation in the Liquid State. *Opt Quantum Electron* **1976**, *8*, 309–315. https://doi.org/10.1007/BF00619543.

(102) Fluorescence, R.; Note, T. Fluorescence Anisotropy/ Technical Aspects. *FLIM microscopy in Biology and Medicine*. 2009, pp 245–288.

(103) Schröder, G. F.; Alexiev, U.; Grubmüller, H. Simulation of Fluorescence Anisotropy Experiments: Probing Protein Dynamics. *Biophys J* **2005**, *89* (6), 3757–3770. https://doi.org/10.1529/biophysj.105.069500.

(104) Hairong Zhang, Qian Wu, and M. Y. B. Fluorescence Anisotropy (Polarization): From Drug Screening to Precision Medicine. *Physiol Behav* **2017**, *176* (3), 139–148. https://doi.org/10.1517/17460441.2015.1075001.

(105) Small, E. W.; Isenberg, I. Hydrodynamic Properties of a Rigid Molecule: Rotational and Linear Diffusion and Fluorescence Anisotropy. *Biopolymers* **1977**, *16* (9), 1907–1928. https://doi.org/10.1002/bip.1977.360160907.

(106) Jaffe, H. H.; Miller, A. L. The Fates of Electronic Excitation Energy. 1964–1966.

(107) Levitus, M. Tutorial: Measurement of Fluorescence Spectra and Determination of Relative Fluorescence Quantum Yields of Transparent Samples. *Methods Appl Fluoresc* **2020**, *8* (3). https://doi.org/10.1088/2050-6120/ab7e10.

(108) Ly, J. T.; Presley, K. F.; Cooper, T. M.; Baldwin, L. A.; Dalton, M. J.; Grusenmeyer, T. A. Impact of Iodine Loading and Substitution Position on Intersystem Crossing Efficiency in a Series of Ten Methylated-: Meso -Phenyl-BODIPY Dyes. *Physical Chemistry Chemical Physics* **2021**, *23* (21), 12033–12044. https://doi.org/10.1039/d0cp05904h.

(109) Filatov, M. A. Biomolecular Chemistry Heavy-Atom-Free BODIPY Photosensitizers with Photoinduced Electron Transfer. *Org Biomol Chem* **2020**, *18* (10), 10–27. https://doi.org/10.1039/c9ob02170a.

(110) You, Z. Q.; Hsu, C. P.; Fleming, G. R. Triplet-Triplet Energy-Transfer Coupling: Theory and Calculation. *Journal of Chemical Physics* **2006**, *124* (4). https://doi.org/10.1063/1.2155433.

(111) Dexter, D. L. A Theory of Sensitized Luminescence in Solids. *J Chem Phys* **1953**,

21 (5), 836–850. https://doi.org/10.1063/1.1699044.

(112) Zhang, Y.; Forrest, S. R. Triplet Diffusion Leads to Triplet-Triplet Annihilation in Organic Phosphorescent Emitters. *Chem Phys Lett* **2013**, *590*, 106–110. https://doi.org/10.1016/j.cplett.2013.10.048.

(113) Guo, X.; Liu, Y.; Chen, Q.; Zhao, D.; Ma, Y. New Bichromophoric Triplet Photosensitizer Designs and Their Application in Triplet–Triplet Annihilation Upconversion. *Adv Opt Mater* **2018**, *6* (4), 1–16. https://doi.org/10.1002/adom.201700981.

(114) Gehlen, M. H. The Centenary of the Stern-Volmer Equation of Fluorescence Quenching: From the Single Line Plot to the SV Quenching Map. *Journal of Photochemistry and Photobiology C: Photochemistry Reviews* **2020**, *42*, 100338.

(115) Braslavsky, S. E. Glossary of Terms Used in Photochemistry, (IUPAC Recommendations 2006). *Pure and Applied Chemistry* **2007**, *79* (3), 293–465.

(116) Calloway, D. Beer-Lambert Law. *J Chem Educ* **1997**, *74* (7), 744.

(117) Khitrova, G.; Berman, P. R.; Iii, M. S. Theory of Pump-Probe Spectroscopy. *J. Opt. Soc. Am. B* **1988**, *5* (1), 160–170. https://doi.org/10.1364/JOSAB.5.000160.

(118) Ruckebusch, C.; Sliwa, M.; Pernot, P.; de Juan, A.; Tauler, R. Comprehensive Data Analysis of Femtosecond Transient Absorption Spectra: A Review. *Journal of Photochemistry and Photobiology C: Photochemistry Reviews* **2012**, *13* (1), 1–27. https://doi.org/10.1016/j.jphotochemrev.2011.10.002.

(119) Montalti, M.; Credi, A.; Prodi, L.; Gandolfi, M. T. *Handbook of Photochemistry*, 3rd Editio.; CRC Press, 2006. https://doi.org/10.1201/9781420015195.

(120) Cavaleri, J. J.; Prater, K.; Bowman, R. M. An Investigation of the Solvent Dependence on the Ultrafast Intersystem Crossing Kinetics of Xanthone. *Chem Phys Lett* **1996**, *259* (5–6), 495–502.

(121) Walker, L. A.; Jarrett, J. T.; Anderson, N. A.; Pullen, S. H.; Matthews, R. G.; Sension, R. J. Time-Resolved Spectroscopic Studies of B12 Coenzymes: The Identification of a Metastable Cob (III) Alamin Photoproduct in the Photolysis of Methylcobalamin. *J Am Chem Soc* **1998**, *120* (15), 3597–3603.

(122) Wolfseder, B.; Seidner, L.; Stock, G.; Domcke, W. Femtosecond Pump-Probe Spectroscopy of Electron-Transfer Systems: A Nonperturbative Approach. *Chem Phys* **1997**, *217* (2-3 SPEC. ISS.), 275–287. https://doi.org/10.1016/s0301-

0104(97)00046-3.

(123) Stark, C. W.; Schreier, W. J.; Lucon, J.; Edwards, E.; Douglas, T.; Kohler, B. Interligand Electron Transfer in Heteroleptic Ruthenium(II) Complexes Occurs on Multiple Time Scales. *Journal of Physical Chemistry A* **2015**, *119* (20), 4813–4824. https://doi.org/10.1021/acs.jpca.5b01770.

(124) Kim, S. Y.; Cho, Y. J.; Son, H. J.; Cho, D. W.; Kang, S. O. Photoinduced Electron Transfer in a BODIPY- Ortho -Carborane Dyad Investigated by Time-Resolved Transient Absorption Spectroscopy. *Journal of Physical Chemistry A* **2018**, *122* (13), 3391–3397. https://doi.org/10.1021/acs.jpca.8b01539.

(125) Min, C. K.; Joo, T.; Yoon, M. C.; Kim, C. M.; Hwang, Y. N.; Kim, D.; Aratani, N.; Yoshida, N.; Osuka, A. Transient Absorption Anisotropy Study of Ultrafast Energy Transfer in Porphyrin Monomer, Its Direct Meso-Meso Coupled Dimer and Trimer. *Journal of Chemical Physics* **2001**, *114* (15), 6750–6758. https://doi.org/10.1063/1.1357438.

(126) Sánchez-Rodríguez, J. A.; Mohamadzade, A.; Mai, S.; Ashwood, B.; Pollum, M.; Marquetand, P.; González, L.; Crespo-Hernández, C. E.; Ullrich, S. 2-Thiouracil Intersystem Crossing Photodynamics Studied by Wavelength-Dependent Photoelectron and Transient Absorption Spectroscopies. *Physical Chemistry Chemical Physics* **2017**, *19* (30), 19756–19766.

(127) Montanaro, S.; Lhiaubet-Vallet, V.; Iesce, M.; Previtera, L.; Miranda, M. A. A Mechanistic Study on the Phototoxicity of Atorvastatin: Singlet Oxygen Generation by a Phenanthrene-like Photoproduct. *Chem Res Toxicol* **2009**, *22* (1), 173–178.

(128) Berera, R.; van Grondelle, R.; Kennis, J. T. M. Ultrafast Transient Absorption Spectroscopy: Principles and Application to Photosynthetic Systems. *Photosynth Res* **2009**, *101* (2–3), 105–118. https://doi.org/10.1007/s11120-009-9454-y.

(129) Ohkita, H.; Tamai, Y.; Benten, H.; Ito, S. Transient Absorption Spectroscopy for Polymer Solar Cells. *IEEE Journal of Selected Topics in Quantum Electronics* **2015**, *22* (1), 100–111.

(130) Ohkita, H.; Ito, S. Transient Absorption Spectroscopy of Polymer-Based Thin-Film Solar Cells. *Polymer (Guildf)* **2011**, *52* (20), 4397–4417.

(131) Knowles, K. E.; Koch, M. D.; Shelton, J. L. Three Applications of Ultrafast Transient Absorption Spectroscopy of Semiconductor Thin Films:

Spectroelectrochemistry, Microscopy, and Identification of Thermal Contributions. *J Mater Chem C Mater* **2018**, *6* (44), 11853–11867.

(132) Cui, Q.; He, J.; Bellus, M. Z.; Mirzokarimov, M.; Hofmann, T.; Chiu, H. Y.; Antonik, M.; He, D.; Wang, Y.; Zhao, H. Transient Absorption Measurements on Anisotropic Monolayer ReS2. *Small* **2015**, *11* (41), 5565–5571. https://doi.org/10.1002/smll.201501668.

(133) Davydova, D.; de la Cadena, A.; Akimov, D.; Dietzek, B. Transient Absorption Microscopy: Advances in Chemical Imaging of Photoinduced Dynamics. *Laser Photon Rev* **2016**, *10* (1), 62–81.

(134) Kim, S.-Y.; Cho, Y.-J.; Son, H.-J.; Dae, †; Cho, W.; Kang, S. O. Photoinduced Electron Transfer in a BODIPY-Ortho-Carborane Dyad Investigated by Time-Resolved Transient Absorption Spectroscopy. *J. Phys. Chem. A* **2018**, *122* (13), 3391–3397. https://doi.org/10.1021/acs.jpca.8b01539.

(135) Farr, E. P.; Quintana, J. C.; Reynoso, V.; Ruberry, J. D.; Shin, W. R.; Swartz, K. R. Introduction to Time-Resolved Spectroscopy: Nanosecond Transient Absorption and Time-Resolved Fluorescence of Eosin B. *J Chem Educ* **2018**, *95* (5), 864–871. https://doi.org/10.1021/acs.jchemed.7b00941.

(136) Haselsberger, R. Femto-to Nanosecond Time-Resolved Pump-Probe Spectroscopy on Electron Transfer in Ferrocenophanone/Oxazine-1, Merocyanine-3/TiO2 and Acridine-Modified. *Spectroscopy* **2003**.

(137) Salin, F. How to Manipulate and Change the Characteristics of Laser Pulses. *Femtosecond laser pulses: Principles and experiments* **2005**, 175–194.

(138) Huber, R.; Satzger, H.; Zinth, W.; Wachtveitl, J. Noncollinear Optical Parametric Amplifiers with Output Parameters Improved by the Application of a White Light Continuum Generated in CaF2. *Opt Commun* **2001**, *194* (4–6), 443–448.

(139) Ziolek, M.; Naskrecki, R.; Karolczak, J. Some Temporal and Spectral Properties of Femtosecond Supercontinuum Important in Pump–Probe Spectroscopy. *Opt Commun* **2004**, *241* (1–3), 221–229.

(140) Rulliere, C.; Amand, T.; Marie, X. Spectroscopic Methods for Analysis of Sample Dynamics. *Femtosecond Laser Pulses: Principles and Experiments* **2005**, 223–281.

(141) Maroncelli, M.; Fleming, G. R. Picosecond Solvation Dynamics of Coumarin 153: The Importance of Molecular Aspects of Solvation. *J Chem Phys* **1987**, *86* (11), 6221–6239.

(142) Dietzek, B.; Pascher, T.; Sundström, V.; Yartsev, A. Appearance of Coherent Artifact Signals in Femtosecond Transient Absorption Spectroscopy in Dependence on Detector Design. *Laser Phys Lett* **2007**, *4* (1), 38–43. https://doi.org/10.1002/lapl.200610070.

(143) Son, M.; Hart, S. M.; Schlau-Cohen, G. S. Investigating Carotenoid Photophysics in Photosynthesis with 2D Electronic Spectroscopy. *Trends Chem* **2021**, *3* (9), 733–746. https://doi.org/10.1016/J.TRECHM.2021.05.008.

(144) Renk, K. F. *Basics of Laser Physics*; Springer, 2012.

(145) Dura, L.; Wächtler, M.; Kupfer, S.; Kübel, J.; Ahrens, J.; Höfler, S.; Bröring, M.; Dietzek, B.; Beweries, T. Photophysics of BODIPY Dyes as Readily-Designable Photosensitisers in Light-Driven Proton Reduction. *Inorganics*. 2017. https://doi.org/10.3390/inorganics5020021.

(146) Wallin, S.; Davidsson, J.; Modin, J.; Hammarström, L. Femtosecond Transient Absorption Anisotropy Study on [Ru(Bpy) 3]2+ and [Ru(Bpy)(Py)4]2+· Ultrafast Interligand Randomization of the MLCT State. *Journal of Physical Chemistry A* **2005**, *109* (21), 4697–4704. https://doi.org/10.1021/jp0509212.

(147) Jonas, D. M.; Lang, M. J.; Nagasawa, Y.; Joo, T.; Fleming, G. R. Pump-Probe Polarization Anisotropy Study of Femtosecond Energy Transfer within the Photosynthetic Reaction Center of Rhodobacter Sphaeroides R26. *Journal of Physical Chemistry* **1996**, *100* (30), 12660–12673. https://doi.org/10.1021/jp960708t.

(148) Burda, C.; Link, S.; Mohamed, M.; El-Sayed, M. The Relaxation Pathways of CdSe Nanoparticles Monitored with Femtosecond Time-Resolution from the Visible to the IR: Assignment of the Transient Features by Carrier Quenching. *J Phys Chem B* **2001**, *105* (49), 12286–12292.

(149) Rosspeintner, A.; Angulo, G.; Vauthey, E. Bimolecular Photoinduced Electron Transfer beyond the Diffusion Limit: The Rehm–Weller Experiment Revisited with Femtosecond Time Resolution. *J Am Chem Soc* **2014**, *136* (5), 2026–2032.

(150) Frisch, M. J. ea; Trucks, G. W.; Schlegel, H. B.; Scuseria, G. E.; Robb, M. A.; Cheeseman, J. R.; Scalmani, G.; Barone, V.; Petersson, G. A.; Nakatsuji, H. Gaussian 16. Gaussian, Inc. Wallingford, CT 2016.

(151) Neese, F.; Wennmohs, F.; Becker, U.; Riplinger, C. The ORCA Quantum Chemistry Program Package. *J Chem Phys* **2020**, *152* (22), 224108.

(152) Haoyu, S. Y.; He, X.; Li, S. L.; Truhlar, D. G. MN15: A Kohn–Sham Global-Hybrid Exchange–Correlation Density Functional with Broad Accuracy for Multi-Reference and Single-Reference Systems and Noncovalent Interactions. *Chem Sci* **2016**, *7* (8), 5032–5051.

(153) Weigend, F. Accurate Coulomb-Fitting Basis Sets for H to Rn. *Physical chemistry chemical physics* **2006**, *8* (9), 1057–1065.

(154) Weigend, F.; Ahlrichs, R. Balanced Basis Sets of Split Valence, Triple Zeta Valence and Quadruple Zeta Valence Quality for H to Rn: Design and Assessment of Accuracy. *Physical Chemistry Chemical Physics* **2005**, *7* (18), 3297–3305.

(155) Grimme, S.; Ehrlich, S.; Goerigk, L. Effect of the Damping Function in Dispersion Corrected Density Functional Theory. *J Comput Chem* **2011**, *32* (7), 1456–1465.

(156) Goerigk, L.; Hansen, A.; Bauer, C.; Ehrlich, S.; Najibi, A.; Grimme, S. A Look at the Density Functional Theory Zoo with the Advanced GMTKN55 Database for General Main Group Thermochemistry, Kinetics and Noncovalent Interactions. *Physical Chemistry Chemical Physics* **2017**, *19* (48), 32184–32215.

(157) Tomasi, J.; Mennucci, B.; Cammi, R. Quantum Mechanical Continuum Solvation Models. *Chem Rev* **2005**, *105* (8), 2999–3094.

(158) Marenich, A. V; Cramer, C. J.; Truhlar, D. G. Universal Solvation Model Based on Solute Electron Density and on a Continuum Model of the Solvent Defined by the Bulk Dielectric Constant and Atomic Surface Tensions. *J Phys Chem B* **2009**, *113* (18), 6378–6396.

(159) Ball, K. Ellipsoids of Maximal Volume in Convex Bodies. *Geom Dedic* **1992**, *41* (2), 241–250.

(160) Yuan, J.; Zhao, L.; Leng, G. Inequalities for Lp Centroid Body. *Taiwanese Journal of Mathematics* **2007**, *11* (5), 1315–1325.

(161) John, F. Extremum Problems with Inequalities as Subsidiary Conditions, in (KO Friedrichs, OE Neugebauer, and JJ Stoker, Eds.) Studies and Essays, Courant Anniversary Volume. Wiley-Interscience, New York 1948.

(162) Van Aelst, S.; Rousseeuw, P. Minimum Volume Ellipsoid. *Wiley Interdiscip Rev Comput Stat* **2009**, *1* (1), 71–82.

(163) Schrader, R. The Ellipsoid Method and Its Implications. *Operations-Research-Spektrum* **1983**, *5* (1), 1–13.

(164) Cohen, M. B.; Cousins, B.; Lee, Y. T.; Yang, X. A Near-Optimal Algorithm for Approximating the John Ellipsoid. In *Conference on Learning Theory*; PMLR, 2019; pp 849–873.

(165) Arellano-Reyes, R. A.; Prabhakaran, A.; Sia, R. C. E.; Guthmuller, J.; Jha, K. K.; Yang, T.; Dietzek-Ivanšić, B.; McKee, V.; Keyes, T. E. BODIPY-Perylene Charge Transfer Compounds; Sensitizers for Triplet-Triplet Annihilation Up-Conversion. *Chemistry – A European Journal* **2023**, *n/a* (n/a), e202300239. https://doi.org/10.1002/chem.202300239.

(166) Bergamini, G.; Ceroni, P.; Fabbrizi, P.; Cicchi, S. A Multichromophoric Dendrimer: From Synthesis to Energy up-Conversion in a Rigid Matrix. *Chemical Communications* **2011**, *47* (48), 12780–12782. https://doi.org/10.1039/c1cc16000a.

(167) Ji, S.; Guo, H.; Wu, W.; Wu, W.; Zhao, J. Ruthenium(II) Polyimine-Coumarin Dyad with Non-Emissive 3IL Excited State as Sensitizer for Triplet-Triplet Annihilation Based Upconversion. *Angewandte Chemie - International Edition*. 2011, pp 8283–8286. https://doi.org/10.1002/anie.201008134.

(168) Schlotthauer, T.; Suchland, B.; Görls, H.; Parada, G. A.; Hammarström, L.; Schubert, U. S.; Jäger, M. Aryl-Decorated RuII Polypyridyl-Type Photosensitizer Approaching NIR Emission with Microsecond Excited State Lifetimes. *Inorg Chem* **2016**, *55* (11), 5405–5416. https://doi.org/10.1021/acs.inorgchem.6b00420.

(169) Jäger, M.; Kumar, R. J.; Görls, H.; Bergquist, J.; Johansson, O. Facile Synthesis of Bistridentate Ru II Complexes Based on 2,6-Di(Quinolin-8-Yl)Pyridyl Ligands: Sensitizers with Microsecond 3MLCT Excited State Lifetimes. *Inorg Chem* **2009**, *48* (7), 3228–3238. https://doi.org/10.1021/ic802342t.

(170) Ragazzon, G.; Verwilst, P.; Denisov, S. A.; Credi, A.; Jonusauskas, G.; McClenaghan, N. D. Ruthenium(II) Complexes Based on Tridentate Polypyridine Ligands That Feature Long-Lived Room-Temperature Luminescence. *Chemical Communications* **2013**, *49* (80), 9110–9112. https://doi.org/10.1039/c3cc45387a.

(171) Denisevich, P.; Abruña, H. D.; Leidner, C. R.; Meyer, T. J.; Murray, R. W. Electropolymerization of Vinylpyridine and Vinylbipyridine Complexes of Iron

and Ruthenium: Homopolymers, Copolymers, Reactive Polymers. *Inorg Chem* **1982**, *21* (6), 2153–2161. https://doi.org/10.1021/ic00136a006.

(172) Abrahamsson, M.; Becker, H. C.; Hammarström, L. Microsecond 3MLCT Excited State Lifetimes in Bis-Tridentate Ru(II)-Complexes: Significant Reductions of Non-Radiative Rate Constants. *Dalton Transactions* **2017**, *46* (39), 13314–13321. https://doi.org/10.1039/c7dt02437a.

(173) Kübel, J.; Schroot, R.; Wächtler, M.; Schubert, U. S.; Dietzek, B.; Jäger, M. Photoredox-Active Dyads Based on a Ru(II) Photosensitizer Equipped with Electron Donor or Acceptor Polymer Chains: A Spectroscopic Study of Light-Induced Processes toward Efficient Charge Separation. *Journal of Physical Chemistry C* **2015**, *119* (9), 4742–4751. https://doi.org/10.1021/acs.jpcc.5b00866.

(174) Chettri, A.; Kruse, J. H.; Kumar Jha, K.; Dröge, L.; Romanenko, I.; Neumann, C.; Kupfer, S.; Turchanin, A.; Rau, S.; Schacher, F. H.; Dietzek, B. A Molecular Photosensitizer in a Porous Block Copolymer Matrix-Implications for the Design of Photocatalytically Active Membranes. *Chemistry - A European Journal* **2021**, *27*, 1–11. https://doi.org/10.1002/chem.202102377.

(175) Takaya, T.; Hamaguchi, H. O.; Iwata, K. Femtosecond Time-Resolved Absorption Anisotropy Spectroscopy on 9, 9′ -Bianthryl: Detection of Partial Intramolecular Charge Transfer in Polar and Nonpolar Solvents. *Journal of Chemical Physics* **2009**, *130* (1). https://doi.org/10.1063/1.3043368.

(176) Rauch, M. P.; Knowles, R. R. Applications and Prospects for Triplet-Triplet Annihilation Photon Upconversion. *Chimia (Aarau)*. https://doi.org/10.2533/chimia.2018.501.

(177) Bachilo, S. M.; Weisman, R. B. Determination of Triplet Quantum Yields from Triplet-Triplet Annihilation Fluorescence. *Journal of Physical Chemistry A*. 2000, pp 7713–7714. https://doi.org/10.1021/jp001877n.

(178) Olesund, A.; Gray, V.; Mårtensson, J.; Albinsson, B. Diphenylanthracene Dimers for Triplet-Triplet Annihilation Photon Upconversion: Mechanistic Insights for Intramolecular Pathways and the Importance of Molecular Geometry. *J Am Chem Soc* **2021**, *143* (15), 5745–5754. https://doi.org/10.1021/jacs.1c00331.

(179) Ye, C.; Gray, V.; Kushwaha, K.; Kumar Singh, S.; Erhart, P.; Börjesson, K. Optimizing Photon Upconversion by Decoupling Excimer Formation and Triplet Triplet Annihilation. *Physical Chemistry Chemical Physics* **2020**, *22* (3), 1715–1720. https://doi.org/10.1039/c9cp06561j.

(180) Ye, C.; Gray, V.; Mårtensson, J.; Börjesson, K. Annihilation Versus Excimer Formation by the Triplet Pair in Triplet-Triplet Annihilation Photon Upconversion. *J Am Chem Soc* **2019**, *141* (24), 9578–9584. https://doi.org/10.1021/jacs.9b02302.

(181) Bohne, C.; Abuin, E. B.; Scaiano, J. C. Characterization of the Triplet-Triplet Annihilation Process of Pyrene and Several Derivatives under Laser Excitation. *J Am Chem Soc* **1990**, *112* (11), 4226–4231. https://doi.org/10.1021/ja00167a018.

(182) Dzebo, D.; Börjesson, K.; Gray, V.; Moth-Poulsen, K.; Albinsson, B. Intramolecular Triplet-Triplet Annihilation Upconversion in 9,10-Diphenylanthracene Oligomers and Dendrimers. *Journal of Physical Chemistry C* **2016**, *120* (41), 23397–23406. https://doi.org/10.1021/acs.jpcc.6b07920.

(183) Olesund, A.; Gray, V.; Mårtensson, J.; Albinsson, B. Diphenylanthracene Dimers for Triplet-Triplet Annihilation Photon Upconversion: Mechanistic Insights for Intramolecular Pathways and the Importance of Molecular Geometry. *J Am Chem Soc* **2021**, *143* (15), 5745–5754. https://doi.org/10.1021/jacs.1c00331.

(184) Raišys, S.; Kazlauskas, K.; Juršenas, S.; Simon, Y. C. The Role of Triplet Exciton Diffusion in Light-Upconverting Polymer Glasses. *ACS Appl Mater Interfaces* **2016**, *8* (24), 15732–15740. https://doi.org/10.1021/acsami.6b03888.

(185) Gao, C.; Prasad, S. K. K.; Zhang, B.; Dvořák, M.; Tayebjee, M. J. Y.; McCamey, D. R.; Schmidt, T. W.; Smith, T. A.; Wong, W. W. H. Intramolecular Versus Intermolecular Triplet Fusion in Multichromophoric Photochemical Upconversion. *Journal of Physical Chemistry C* **2019**, *123* (33), 20181–20187. https://doi.org/10.1021/acs.jpcc.9b07098.

(186) O'shea, R.; Kendrick, W. J.; Gao, C.; Owyong, T. C.; White, J. M.; Ghiggino, K. P.; Wong, W. W. H. Revealing the Influence of Steric Bulk on the Triplet–Triplet Annihilation Upconversion Performance of Conjugated Polymers. *Sci Rep* **2021**, *11* (1), 1–10. https://doi.org/10.1038/s41598-021-99179-y.

(187) Gray, V.; Börjesson, K.; Dzebo, D.; Abrahamsson, M.; Albinsson, B.; Moth-Poulsen, K. Porphyrin-Anthracene Complexes: Potential in Triplet-Triplet Annihilation Upconversion. *Journal of Physical Chemistry C* **2016**, *120* (34), 19018–19026. https://doi.org/10.1021/acs.jpcc.6b06298.

(188) Gray, V.; Küçüköz, B.; Edhborg, F.; Abrahamsson, M.; Moth-Poulsen, K.; Albinsson, B. Singlet and Triplet Energy Transfer Dynamics in Self-Assembled Axial Porphyrin-Anthracene Complexes: Towards Supra-Molecular Structures

for Photon Upconversion. *Physical Chemistry Chemical Physics* **2018**, *20* (11), 7549–7558. https://doi.org/10.1039/c8cp00884a.

(189) Abrahamsson, M.; Jäger, M.; Österman, T.; Eriksson, L.; Persson, P.; Becker, H. C.; Johansson, O.; Hammarström, L. A 3.0 Ms Room Temperature Excited State Lifetime of a Bistridentate RuII-Polypyridine Complex for Rod-like Molecular Arrays. *J Am Chem Soc* **2006**, *128* (39), 12616–12617. https://doi.org/10.1021/ja064262y.

(190) Heinrich, G.; Schoof, S.; Gusten, H. 9,10-Diphenylanthracene As a Fluorescence Quantum Yield Standard. *Journal of Photochemistry* **1974**, *3* (2), 315–320. https://doi.org/10.1016/0047-2670(74)80040-7.

(191) Mark S. Workentin, Linda J. Johnston, Danial D. M. Wayner, and V. D. P. Reactivity of Aromatic Radical Cations. Rate Constants for Reactions of 9-Phenyl- and 9,10-Diphenylanthracene Radical Cations with Acyclic Amines. *J. Am. Chem. Soc.* **1994**, *116* (18), 8279–8287.

(192) Singh-Rachford, T. N.; Castellano, F. N. Photon Upconversion Based on Sensitized Triplet-Triplet Annihilation. *Coord Chem Rev* **2010**, *254* (21–22), 2560–2573. https://doi.org/10.1016/j.ccr.2010.01.003.

(193) Chen, Q.; Liu, Y.; Guo, X.; Peng, J.; Garakyaraghi, S.; Papa, C. M.; Castellano, F. N.; Zhao, D.; Ma, Y. Energy Transfer Dynamics in Triplet-Triplet Annihilation Upconversion Using a Bichromophoric Heavy-Atom-Free Sensitizer. *Journal of Physical Chemistry A* **2018**, *122* (33), 6673–6682. https://doi.org/10.1021/acs.jpca.8b05901.

(194) Bonneau, R.; Carmichael, I.; Hug, G. L. Molar Absorption Coefficients of Transient Species in Solution. *Pure and Applied Chemistry* **1991**, *63* (2), 289–300. https://doi.org/10.1351/pac199163020289.

(195) Jortner, J.; Choi, S. Il; Katz, J. L.; Rice, S. A. Triplet Energy Transfer and Triplet-Triplet Interaction in Aromatic Crystals. *Phys Rev Lett* **1963**, *11* (7), 323–326. https://doi.org/10.1103/PhysRevLett.11.323.

(196) Ulrich, G.; Ziessel, R.; Harriman, A. The Chemistry of Fluorescent Bodipy Dyes: Versatility Unsurpassed. *Angewandte Chemie - International Edition* **2008**, *47* (7), 1184–1201. https://doi.org/10.1002/anie.200702070.

(197) Loudet, A.; Burgess, K. BODIPY Dyes and Their Derivatives: Syntheses and Spectroscopic Properties. *Chem Rev* **2007**, *107* (11), 4891–4932.

https://doi.org/10.1021/cr078381n.

(198) Maleckaitė, K.; Narkevičius, D.; Žilėnaitė, R.; Dodonova-Vaitkūnienė, J.; Toliautas, S.; Tumkevičius, S.; Vyšniauskas, A. Give or Take: Effects of Electron-Accepting/-Withdrawing Groups in Red-Fluorescent BODIPY Molecular Rotors. *Molecules* **2022**, *27* (1). https://doi.org/10.3390/molecules27010023.

(199) Filatov, M. A. Heavy-Atom-Free BODIPY Photosensitizers with Intersystem Crossing Mediated by Intramolecular Photoinduced Electron Transfer. *Org Biomol Chem* **2019**, *18* (1), 10–27. https://doi.org/10.1039/c9ob02170a.

(200) Lee, S. C.; Heo, J.; Woo, H. C.; Lee, J. A.; Seo, Y. H.; Lee, C. L.; Kim, S.; Kwon, O. P. Fluorescent Molecular Rotors for Viscosity Sensors. *Chemistry - A European Journal* **2018**, *24* (52), 13706–13718. https://doi.org/10.1002/chem.201801389.

(201) Haidekker, M. A.; Nipper, M.; Mustafic, A.; Lichlyter, D.; Dakanali, M.; Theodorakis, E. A. *Dyes with Segmental Mobility: Molecular Rotors*; Springer Berlin Heidelberg: Berlin, Heidelberg, 2010. https://doi.org/10.1007/978-3-642-04702-2_8.

(202) Kuimova, M. K.; Yahioglu, G.; Levitt, J. A.; Suhling, K. Molecular Rotor Measures Viscosity of Live Cells via Fluorescence Lifetime Imaging. *J Am Chem Soc* **2008**, *130* (21), 6672–6673. https://doi.org/10.1021/ja800570d.

(203) Reinholdt, P.; Wind, S.; Wüstner, D.; Kongsted, J. Computational Characterization of a Cholesterol-Based Molecular Rotor in Lipid Membranes. *Journal of Physical Chemistry B* **2019**, *123* (34), 7313–7326. https://doi.org/10.1021/acs.jpcb.9b04967.

(204) Vyšniauskas, A.; López-Duarte, I.; Duchemin, N.; Vu, T. T.; Wu, Y.; Budynina, E. M.; Volkova, Y. A.; Peña Cabrera, E.; Ramírez-Ornelas, D. E.; Kuimova, M. K. Exploring Viscosity, Polarity and Temperature Sensitivity of BODIPY-Based Molecular Rotors. *Physical Chemistry Chemical Physics* **2017**, *19* (37), 25252–25259. https://doi.org/10.1039/c7cp03571c.

(205) Li, F.; Yang, S. I.; Ciringh, Y.; Seth, J.; Martin, C. H.; Singh, D. L.; Kim, D.; Birge, R. R.; Bocian, D. F.; Holten, D.; Lindsey, J. S. Design, Synthesis, and Photodynamics of Light-Harvesting Arrays Comprised of a Porphyrin and One, Two, or Eight Boron-Dipyrrin Accessory Pigments. *J Am Chem Soc* **1998**, *120* (39), 10001–10017. https://doi.org/10.1021/ja9812047.

(206) Walde, P.; Cosentino, K.; Engel, H.; Stano, P. Giant Vesicles: Preparations and

Applications. *ChemBioChem* **2010**, *11* (7), 848–865. https://doi.org/10.1002/cbic.201000010.

(207) Peters, R.; Cherrytt, R. J. Lateral and Rotational Diffusion of Bacteriorhodopsin in Lipid Bilayers : Experimental Test of the Saffman-Delbruck Equations. *Proc Natl Acad Sci U S A* **1982**, *79* (14), 4317–4321. https://doi.org/10.2307/12584.

(208) Jain, P.; Motosuke, M. Fluorescence Anisotropy Studies on Bodipy (Pyrromethene 546) Dye as a Novel Thermal Probe. *J Fluoresc* **2022**, No. Pyrromethene 546. https://doi.org/10.1007/s10895-021-02868-0.

(209) Chung, P. H.; Tregidgo, C.; Suhling, K. Determining a Fluorophore's Transition Dipole Moment from Fluorescence Lifetime Measurements in Solvents of Varying Refractive Index. *Methods Appl Fluoresc* **2016**, *4* (4). https://doi.org/10.1088/2050-6120/4/4/045001.

(210) Bergström, F.; Mikhalyov, I.; Hägglöf, P.; Wortmann, R.; Ny, T.; Johansson, L. B. Å. Dimers of Dipyrrometheneboron Difluoride (BODIPY) with Light Spectroscopic Applications in Chemistry and Biology. *J Am Chem Soc* **2002**, *124* (2), 196–204. https://doi.org/10.1021/ja010983f.

(211) Grudzinski, W.; Sagan, J.; Welc, R.; Luchowski, R.; Gruszecki, W. I. Molecular Organization, Localization and Orientation of Antifungal Antibiotic Amphotericin B in a Single Lipid Bilayer. *Sci Rep* **2016**, *6* (August), 1–11. https://doi.org/10.1038/srep32780.

(212) Grudzinski, W.; Sagan, J.; Welc, R.; Luchowski, R.; Gruszecki, W. I. Molecular Organization, Localization and Orientation of Antifungal Antibiotic Amphotericin B in a Single Lipid Bilayer: Supplimetry Information. *Sci Rep* **2016**, *6*. https://doi.org/10.1038/srep32780.

(213) Zhou, Z.; Yan, X.; Lai, Y. H.; Zare, R. N. Fluorescence Polarization Anisotropy in Microdroplets. *Journal of Physical Chemistry Letters* **2018**, *9* (11), 2928–2932. https://doi.org/10.1021/acs.jpclett.8b01129.

(214) Goto, A.; Otomo, K.; Nemoto, T. Real-Time Polarization-Resolved Imaging of Living Tissues Based on Two-Photon Excitation Spinning-Disk Confocal Microscopy. *Front Phys* **2019**, *7* (MAR), 1–9. https://doi.org/10.3389/fphy.2019.00056.

(215) Zhixin Zhou Ying Li, Anran Liu, Songqin Liu, and Yuanjian Zhang, Y. S. Physicochemical and Computational Insight of 19F NMR and Emission

Properties of Meso-(o-Aryl)-BODIPYs: Supporting Information. *Aldenderfer, Mark S., Craig, Nathan M., Speakman, Robert Jeff, and Popelka-Filcoff, Rachel S.* **2015**, *2* (1), 1–5.

(216) Carlotti, B.; Poddar, M.; Elisei, F.; Spalletti, A.; Misra, R. Energy-Transfer and Charge-Transfer Dynamics in Highly Fluorescent Naphthalimide-BODIPY Dyads: Effect of BODIPY Orientation. *Journal of Physical Chemistry C* **2019**, *123* (40), 24362–24374. https://doi.org/10.1021/acs.jpcc.9b05851.

(217) Sui, B.; Bondar, M. V.; Anderson, D.; Rivera-Jacquez, H. J.; Masunov, A. E.; Belfield, K. D. New Two-Photon Absorbing BODIPY-Based Fluorescent Probe: Linear Photophysics, Stimulated Emission, and Ultrafast Spectroscopy. *Journal of Physical Chemistry C* **2016**, *120* (26), 14317–14329. https://doi.org/10.1021/acs.jpcc.6b04426.

(218) Uzhinov, B. M.; Ivanov, V. L.; Melnikov, M. Y. Molecular Rotors as Luminescence Sensors of Local Viscosity and Viscous Flow in Solutions and Organized Systems. *Russian Chemical Reviews* **2011**, *80* (12), 1179–1190. https://doi.org/10.1070/rc2011v080n12abeh004246.

(219) Ohligschläger, A., Menzel, K., Ten Kate, A., Martinez, J.R., Frömbgen, C., Arts, J., McCulloch, A., Rossberg, M., Lendle, W., Pfleiderer, G., Tögel, A., Torkelson, T.R. and Beutel, K. K. Dichloromethane. *Chloromethanes. In Ullmann's Encyclopedia of Industrial Chemistry* **2022**, *12*, 148–150. https://doi.org/10.1002/14356007.a06_233.pub4.

(220) Pochorovski, I.; Knehans, T.; Nettels, D.; Müller, A. M.; Schweizer, W. B.; Caflisch, A.; Schuler, B.; Diederich, F. Experimental and Computational Study of BODIPY Dye-Labeled Cavitand Dynamics. *J Am Chem Soc* **2014**, *136* (6), 2441–2449. https://doi.org/10.1021/ja4104292.

(221) Van Veldhoven, E.; Zhang, H.; Glasbeek, M. Femtosecond Fluorescence Anisotropy Studies of Solvation-Induced Intraligand Charge Transfer in Photoexcited Aluminum(III) Tris(8-Hydroxyquinoline). *Journal of Physical Chemistry A* **2001**, *105* (10), 1687–1692. https://doi.org/10.1021/jp003540r.

(222) Dong, Y.; Taddei, M.; Doria, S.; Bussotti, L.; Zhao, J.; Mazzone, G.; Di Donato, M. Torsion-Induced Nonradiative Relaxation of the Singlet Excited State of Meso-Thienyl Bodipy and Charge Separation, Charge Recombination-Induced Intersystem Crossing in Its Compact Electron Donor/Acceptor Dyads. *Journal of Physical Chemistry B* **2021**, *125* (18), 4779–4793.

https://doi.org/10.1021/acs.jpcb.1c00053.

(223) Kinosita, K.; Ikegami, A.; Kawato, S. On the Wobbling-in-Cone Analysis of Fluorescence Anisotropy Decay. *Biophys J* **1982**, *37* (2), 461–464. https://doi.org/10.1016/S0006-3495(82)84692-4.

(224) Schröder, G. F.; Alexiev, U.; Grubmüller, H. Simulation of Fluorescence Anisotropy Experiments: Probing Protein Dynamics. *Biophys J* **2005**, *89* (6), 3757–3770. https://doi.org/10.1529/biophysj.105.069500.

(225) Vogel, S. S.; Thaler, C.; Blank, P. S.; Koushik, S. v. Time-Resolved Fluorescence Anisotropy. *Flim Microscopy in Biology and Medicine* **2009**, 245–288. https://doi.org/10.1201/9781420078916-17.

(226) Schneider, K. R. A.; Chettri, A.; Cole, H. D.; Reglinski, K.; Brückmann, J.; Roque, J. A.; Stumper, A.; Nauroozi, D.; Schmid, S.; Lagerholm, C. B.; Rau, S.; Bäuerle, P.; Eggeling, C.; Cameron, C. G.; McFarland, S. A.; Dietzek, B. Intracellular Photophysics of an Osmium Complex Bearing an Oligothiophene Extended Ligand. *Chemistry - A European Journal* **2020**, *26* (65), 14844–14851. https://doi.org/10.1002/chem.202002667.

(227) Marian, C. M. Understanding and Controlling Intersystem Crossing in Molecules. *Annu Rev Phys Chem* **2020**, *72*, 617–640. https://doi.org/10.1146/annurev-physchem-061020-053433.

(228) Marian, C. M. Spin-Orbit Coupling and Intersystem Crossing in Molecules. *Wiley Interdiscip Rev Comput Mol Sci* **2012**, *2* (2), 187–203. https://doi.org/10.1002/wcms.83.

(229) Dongyi Liu, Ahmed M. El-Zohry, Maria Taddei, Clemens Matt, Laura Bussotti, Zhijia Wang, Jianzhang Zhao, Omar F. Mohammed, Mariangela Di Donato, and S. W. Long-Lived Charge-Transfer State Induced by Spin-Orbit Charge Transfer Intersystem Crossing (SOCT-ISC) in a Compact Spiro Electron Donor/Acceptor Dyad. *Angewandte Chemie - International Edition* **2020**, *59* (28), 11591–11599. https://doi.org/10.1002/anie.202003560.

(230) Liu, Y.; Zhao, J.; Iagatti, A.; Bussotti, L.; Foggi, P.; Castellucci, E.; Di Donato, M.; Han, K.-L. A Revisit to the Orthogonal Bodipy Dimers: Experimental Evidence for the Symmetry Breaking Charge Transfer-Induced Intersystem Crossing. *The Journal of Physical Chemistry C* **2018**, *122* (5), 2502–2511. https://doi.org/10.1021/acs.jpcc.7b10213.

(231) Imran, M.; A. Sukhanov, A.; Wang, Z.; Karatay, A.; Zhao, J.; Mahmood, Z.; Elmali, A.; K. Voronkova, V.; Hayvali, M.; Heng Xing, Y.; Weber, S. Electronic Coupling and Spin–Orbit Charge-Transfer Intersystem Crossing in Phenothiazine–Perylene Compact Electron Donor/Acceptor Dyads. *The Journal of Physical Chemistry C* **2019**, *123* (12), 7010–7024. https://doi.org/10.1021/acs.jpcc.8b12040.

(232) Brown, A. M.; McCusker, C. E.; McCusker, J. K. Spectroelectrochemical Identification of Charge-Transfer Excited States in Transition Metal-Based Polypyridyl Complexes. *Dalton Transactions* **2014**, *43* (47), 17635–17646. https://doi.org/10.1039/c4dt02849j.

(233) Zhijia Wang, Mikhail Ivanov, Yuting Gao, Laura Bussotti, Paolo Foggi, Huimin Zhang, Nino Russo, Bernhard Dick, Jianzhang Zhao, Mariangela Di Donato, Gloria Mazzone, Liang Luo, M. F. Spin–Orbit Charge-Transfer Intersystem Crossing (ISC) in Compact Electron Donor–AcceptorDyads:ISC Mechanism and Application as Novel and Potent Photodynamic Therapy Reagents. *Chemistry – A European Journal* **2020**, *26* (5), 1091–1102. https://doi.org/10.1002/chem.201904306.

(234) BODIPY-perylene Charge Transfer Compounds Sensitizers for Triplet-triplet.

(235) Zhao, Y.; Duan, R.; Zhao, J.; Li, C. Spin–Orbit Charge Transfer Intersystem Crossing in Perylenemonoimide–Phenothiazine Compact Electron Donor–Acceptor Dyads. *Chemical Communications* **2018**, *54* (87), 12329–12332. https://doi.org/10.1039/C8CC07012A.

(236) Wang, X.; Song, Y.; Pan, G.; Han, W.; Wang, B.; Cui, L.; Ma, H.; An, Z.; Xie, Z.; Xu, B.; Tian, W. Exploiting Radical-Pair Intersystem Crossing for Maximizing Singlet Oxygen Quantum Yields in Pure Organic Fluorescent Photosensitizers. *Chem Sci* **2020**, *11* (40), 10921–10927. https://doi.org/10.1039/d0sc03128c.

(237) Nguyen, V. N.; Ha, J.; Koh, C. W.; Ryu, B.; Kim, G.; Park, J. H.; Kim, C. Y.; Park, S.; Yoon, J. Access to the Triplet Excited States of Heavy-Atom-Free Boron-Dipyrromethene Photosensitizers via Radical Pair Intersystem Crossing for Image-Guided Tumor-Targeted Photodynamic Therapy. *Chemistry of Materials* **2021**, *33* (19), 7889–7896. https://doi.org/10.1021/acs.chemmater.1c02776.

(238) Benniston, A. C.; Copley, G. Lighting the Way Ahead with Boron Dipyrromethene (Bodipy) Dyes. *Physical Chemistry Chemical Physics* **2009**, *11* (21), 4124–4131. https://doi.org/10.1039/b901383k.

(239) Chen, K.; Dong, Y.; Zhao, X.; Imran, M.; Tang, G.; Zhao, J.; Liu, Q. Bodipy Derivatives as Triplet Photosensitizers and the Related Intersystem Crossing Mechanisms. *Front Chem* **2019**, *7* (December), 1–14. https://doi.org/10.3389/fchem.2019.00821.

(240) Kamkaew, A.; Lim, S. H.; Lee, H. B.; Kiew, L. V.; Chung, L. Y.; Burgess, K. BODIPY Dyes in Photodynamic Therapy. *Chem. Soc. Rev.* **2013**, *42* (1), 77–88. https://doi.org/10.1039/C2CS35216H.

(241) Zhao, J.; Wu, W.; Sun, J.; Guo, S. Triplet Photosensitizers: From Molecular Design to Applications. *Chem Soc Rev* **2013**, *42* (12), 5323. https://doi.org/10.1039/c3cs35531d.

(242) Chen, K.; Dong, Y.; Zhao, X.; Imran, M.; Tang, G.; Zhao, J.; Liu, Q. Bodipy Derivatives as Triplet Photosensitizers and the Related Intersystem Crossing Mechanisms. *Front Chem* **2019**, *7* (December), 1–14. https://doi.org/10.3389/fchem.2019.00821.

(243) Sittig, M.; Schmidt, B.; Görls, H.; Bocklitz, T.; Wächtler, M.; Zechel, S.; Hager, M. D.; Dietzek, B. Fluorescence Upconversion by Triplet–Triplet Annihilation in All-Organic Poly(Methacrylate)-Terpolymers. *Physical Chemistry Chemical Physics* **2020**, *22* (7), 4072–4079. https://doi.org/10.1039/D0CP00232A.

(244) Fujimoto, K.; Kawai, K.; Masuda, S.; Mori, T.; Aizawa, T.; Inuzuka, T.; Karatsu, T.; Sakamoto, M.; Yagai, S.; Sengoku, T.; Takahashi, M.; Yoda, H. Triplet–Triplet Annihilation-Based Upconversion Sensitized by a Reverse Micellar Assembly of Amphiphilic Ruthenium Complexes. *Langmuir* **2019**, *35* (30), 9740–9746. https://doi.org/10.1021/acs.langmuir.9b01433.

(245) Cui, X.; M. El-Zohry, A.; Wang, Z.; Zhao, J.; F. Mohammed, O. Homo- or Hetero-Triplet–Triplet Annihilation? A Case Study with Perylene-BODIPY Dyads/Triads. *The Journal of Physical Chemistry C* **2017**, *121* (30), 16182–16192. https://doi.org/10.1021/acs.jpcc.7b05620.

(246) Wu, W.; Guo, H.; Wu, W.; Ji, S.; Zhao, J. Organic Triplet Sensitizer Library Derived from a Single Chromophore (BODIPY) with Long-Lived Triplet Excited State for Triplet–Triplet Annihilation Based Upconversion. *J Org Chem* **2011**, *76* (17), 7056–7064. https://doi.org/10.1021/jo200990y.

(247) Wang, Z.; Sukhanov, A. A.; Toffoletti, A.; Sadiq, F.; Zhao, J.; Barbon, A.; Voronkova, V. K.; Dick, B. Insights into the Efficient Intersystem Crossing of Bodipy-Anthracene Compact Dyads with Steady-State and Time-Resolved

Optical/Magnetic Spectroscopies and Observation of the Delayed Fluorescence. *Journal of Physical Chemistry C* **2019**, *123* (1), 265–274. https://doi.org/10.1021/acs.jpcc.8b10835.

(248) Chen, K.; Yang, W.; Wang, Z.; Iagatti, A.; Bussotti, L.; Foggi, P.; Ji, W.; Zhao, J.; Di Donato, M. Triplet Excited State of BODIPY Accessed by Charge Recombination and Its Application in Triplet–Triplet Annihilation Upconversion. *J Phys Chem A* **2017**, *121* (40), 7550–7564. https://doi.org/10.1021/acs.jpca.7b07623.

(249) Wang, Z.; Zhao, J. Bodipy-Anthracene Dyads as Triplet Photosensitizers: Effect of Chromophore Orientation on Triplet-State Formation Efficiency and Application in Triplet-Triplet Annihilation Upconversion. *Org Lett* **2017**, *19* (17), 4492–4495. https://doi.org/10.1021/acs.orglett.7b02047.

(250) Chen, K.; Yang, W.; Wang, Z.; Iagatti, A.; Bussotti, L.; Foggi, P.; Ji, W.; Zhao, J.; Di Donato, M. Triplet Excited State of BODIPY Accessed by Charge Recombination and Its Application in Triplet-Triplet Annihilation Upconversion. *Journal of Physical Chemistry A* **2017**, *121* (40), 7550–7564. https://doi.org/10.1021/acs.jpca.7b07623.

(251) Mikhail A. Filatov, Safakath Karuthedath, Pavel M. Polestshuk, Susan Callaghan, Keith J. Flanagan, Thomas Wiesner, Frédéric Laquai, M. O. S. BODIPY-Pyrene and Perylene Dyads as Heavy-Atom-Free Singlet Oxygen Sensitizers. *ChemPhotoChem* **2018**, *2* (7), 606–615. https://doi.org/10.1002/cptc.201800020.

(252) Gibbons, D. J.; Farawar, A.; Mazzella, P.; Leroy-Lhez, S.; Williams, R. M. Making Triplets from Photo-Generated Charges: Observations, Mechanisms and Theory. *Photochemical and Photobiological Sciences* **2020**, *19* (2), 136–158. https://doi.org/10.1039/c9pp00399a.

(253) Suzuki, S.; Kozaki, M.; Nozaki, K.; Okada, K. Recent Progress in Controlling Photophysical Processes of Donor-Acceptor Arrays Involving Perylene Diimides and Boron-Dipyrromethenes. *Journal of Photochemistry and Photobiology C: Photochemistry Reviews* **2011**, *12* (4), 269–292. https://doi.org/10.1016/j.jphotochemrev.2011.10.001.

(254) Buck, J. T.; Boudreau, A. M.; DeCarmine, A.; Wilson, R. W.; Hampsey, J.; Mani, T. Spin-Allowed Transitions Control the Formation of Triplet Excited States in Orthogonal Donor-Acceptor Dyads. *Chem* **2019**, *5* (1), 138–155.

https://doi.org/10.1016/j.chempr.2018.10.001.

(255) Dr. Mikhail A. Filatov,Dr. Safakath Karuthedath,Dr. Pavel M. Polestshuk,Susan Callaghan,Keith J. Flanagan,Thomas Wiesner,Prof. Dr. Frédéric Laquai, Prof. Dr. M. O. S. BODIPY-Pyrene and Perylene Dyads as Heavy-Atom-Free Singlet Oxygen Sensitizers. *ChemPhotoChem* **2018**, *2* (7), 606–615. https://doi.org/10.1002/cptc.201800020.

(256) Ly, J. T.; Presley, K. F.; Cooper, T. M.; Baldwin, L. A.; Dalton, M. J.; Grusenmeyer, T. A. Impact of Iodine Loading and Substitution Position on Intersystem Crossing Efficiency in a Series of Ten Methylated-: Meso -Phenyl-BODIPY Dyes. *Physical Chemistry Chemical Physics* **2021**, *23* (21), 12033–12044. https://doi.org/10.1039/d0cp05904h.

(257) Filatov, M. A.; Karuthedath, S.; Polestshuk, P. M.; Callaghan, S.; Flanagan, K. J.; Wiesner, T.; Laquai, F.; Senge, M. O. BODIPY-Pyrene and Perylene Dyads as Heavy-Atom-Free Singlet Oxygen Sensitizers. *ChemPhotoChem* **2018**, *2* (7), 606–615. https://doi.org/10.1002/cptc.201800020.

(258) Müller, C.; Pascher, T.; Eriksson, A.; Chabera, P.; Uhlig, J. KiMoPack: A Python Package for Kinetic Modeling of the Chemical Mechanism. *J Phys Chem A* **2022**, *126* (25), 4087–4099. https://doi.org/10.1021/acs.jpca.2c00907.

(259) Wei, Z.; M. Philip, A.; F. Jager, W.; C. Grozema, F. Fast Charge Separation in Distant Donor–Acceptor Dyads Driven by Relaxation of a Hot Excited State. *The Journal of Physical Chemistry C* **2022**, *126* (45), 19250–19261. https://doi.org/10.1021/acs.jpcc.2c05754.

(260) Lei, Y.; Chen, K.; Tang, G.; Zhao, J.; Gurzadyan, G. G. Bodipy-Phenylethynyl Anthracene Dyad: Spin-Orbit Charge Transfer Intersystem Crossing and Triplet Excited-State Equilibrium. *J Photochem Photobiol A Chem* **2020**, *398* (April), 112573. https://doi.org/10.1016/j.jphotochem.2020.112573.

(261) Hou, Y.; Zhang, X.; Chen, K.; Liu, D.; Wang, Z.; Liu, Q.; Zhao, J.; Barbon, A. Charge Separation, Charge Recombination, Long-Lived Charge Transfer State Formation and Intersystem Crossing in Organic Electron Donor/Acceptor Dyads. *J Mater Chem C Mater* **2019**, *7* (39), 12048–12074. https://doi.org/10.1039/c9tc04285g.

(262) Buck, J. T.; Andrew, M.; Wilson, R. W.; Buck, J. T.; Boudreau, A. M.; Wilson, R. W.; Hampsey, J. Spin-Allowed Transitions Control the Formation of Triplet Excited States in Orthogonal Donor-Acceptor Dyads Spin-Allowed Transitions

Control the Formation of Triplet Excited States in Orthogonal Donor-Acceptor Dyads. *Chem* **2018**, *5* (1), 138–155. https://doi.org/10.1016/j.chempr.2018.10.001.

(263) Hou, Y.; Liu, J.; Zhang, N.; Zhao, J. Long-Lived Local Triplet Excited State and Charge Transfer State of 4 , 4 ' -Dimethoxy Triphenylamine-BODIPY Compact Electron Donor / Acceptor Dyads. *Journal of Physical Chemistry A* **2020**, *124* (45), 9360–9375. https://doi.org/10.1021/acs.jpca.0c07907.

(264) Benniston, A. C.; Harriman, A.; Llarena, I.; Sams, C. A. Intramolecular Delayed Fluorescence as a Tool for Imaging Science: Synthesis and Photophysical Properties of a First-Generation Emitter. *Chemistry of Materials* **2007**, *19* (8), 1931–1938. https://doi.org/10.1021/cm062525h.

(265) Gajardo-Parra, N. F.; Campos-Franzani, M. I.; Hernández, A.; Escalona, N.; Canales, R. I. Density and Viscosity of Binary Mixtures Composed of Anisole with Dodecane, Hexadecane, Decalin, or 1,4-Dioxane: Experiments and Modeling. *J Chem Eng Data* **2020**, *65* (4), 2032–2043. https://doi.org/10.1021/acs.jced.9b01159.

List of Figures

List of Tables

Acknowledgements

I would like to thank my Ph.D. supervisor Prof. Dr. Benjamin Dietzek Ivanšić for his kind support and enthusiasm. His words always motivated me to learn spectroscopy and chemistry.

I would like to thank my master thesis supervisor Prof. Dr. Varun Raghunathan for teaching me basics of optics and microscopy; without his training I would not have been able to pursue optics-based experiments.

I would like to thank my co-supervisor Prof. Dr. Tia Keyes for supporting me throughout the Ph.D. program and being my examiner.

I would like to thank my guru Sri Sri Ravisharkar and Sri S N Goenka for teaching me meditation and happiness, which keeps me motivated always.

I would like to thank Dr. Julien Guthmuller for providing the computational results and discussions.

I would like to thank the European Union for LOGICLAB Marie Skłodowska-Curie Innovative Training Network (ITN) funding (grant agreement Number 813920). This generous funding supported me in living and pursuing my doctoral studies in Europe. The funding also supported secondment training at Dublin City University, Ireland.

I would like to thank Dr. Wolfgang Paa and Dr. Shankar Jha for proofreading this thesis. Dr. Paa also supported me in development of vibrational sum frequency generation setup at Leibniz-IPHT, Jena.

I would like to thank Ms. Ramona Scheibinger for translating and proof reading the summary in German language.

I would like to thank Mr. Avinash Chettri, Dr. Mathias Micheel and Dr. Kilian Schneider for supporting me in the initial phase of the experiments and discussion throughout the Ph.D. program.

I would like to thank Dr. Felix Herrmann-Westendorf and Dr. Denis Akimov for providing technical support on lasers and optical setups.

I would like to thank Prof. Dr. Michael Börsch, Lukas Spantzel and Iván Pérez for access to his microscopy laboratory and assistance with measurements.

I would like to thank Dr. Anja Schulz for her non-academic support and helping me during initial days in Jena.

I would like to thank my friends from LOGICLAB ITN: Ms. Amrutha Prabhakaran for providing liposomes, Ms. Tingxiang Yang for teaching me streak camera, Mr. Ruben Arellano-Reyes for providing Ruthenium and BODIPY molecules, Mr. Rengel Cane Sia for providing computational results, Mr. Hani Elbehairy for supporting me on fume-hoods and all other members for their support.

I would like to thank Prof. Dr. Maria Wächtler, PD Dr. Martin Presselt and Dr. Martin Schulz for their kind support and discussions.

I would like to thank Mr. Raktim Baruah for teaching me the operation of glovebox.

I would like to thank PD. Dr. Christoph Krafft and colleagues from Raman Spectroscopy group at Leibniz-IPHT for their kind support in laboratory.

I would like to thank Ms. Abha Valavalkar for proofreading this thesis and entire team of AG Dietzek-Ivanšić for their support during my PhD program.

I would like to thank Shri Dev Krishna Jha (Devta Jha Sir) for teaching me basics of mathematics and motivations.

I would like to thank Shri Shravan Kumar Jha, my secondary school teacher for motivation and enthusiasm.

I would like to thank my primary and secondary school teachers for giving me education and motivation.

I would like to thank my loving family members: my mother Ms. Savita Jha and father Mr. Shravan Jha for giving me education from nursery to Ph.D.; my wife Dr. Pratishtha Sharma for her support in organizing my day to day life in the last year of Ph.D. program and proof reading this thesis, my brother and sister for their loving support. I also thank my father-in-law Dr. Durga Prasad Sharma for his kind blessings. I would like to thank my cousin Mr. Sant Kumar Choudhary for supporting my higher secondary education. I thank my cousins and in-law family members for their love and kind support, which keeps motivated in difficult times.

Selbstständigkeitserklärung

Ich erkläre, dass ich die vorliegende Arbeit selbstständig und unter Verwendung der angegebenen Hilfsmittel, persönlichen Mitteilungen und Quellen angefertigt habe.

Keshav Kumar Jha 25.04.2023 Jena……